Floquet Defect Mode Resonance and its Applications in Nonlinear, Quantum and Active Topological Silicon Photonics

by

Tyler James Zimmerling

A thesis submitted in partial fulfillment of the requirements for the degree of

Doctor of Philosophy

in

Photonics and Plasmas

Department of Electrical and Computer Engineering
University of Alberta

Abstract

Topological photonic insulators are photonic quantum metamaterials whose transmission bands and bandgaps are characterized by certain topological invariants, which remain unchanged in the presence of lattice disorders. This resistance to defects has been exploited to realize integrated photonic devices that are tolerant to random variations, such as fabrication-induced imperfections or fluctuations in device operating conditions. While topological photonic insulators have been demonstrated for some applications such as optical delay lines, lasers, and single-photon emitters, the lack of efficient methods for trapping and steering light in a topological photonic lattice has limited their potential applications. Floquet defect mode resonance (FDMR), induced through a perturbation to the periodic Hamiltonian, can form compact, tunable, and high quality factor resonances in a Floquet insulator composed of a 2D lattice of coupled microring resonators. This research focuses on the design and implementation of high quality factor FDMRs on a silicon topological photonic platform and explores their potential applications in nonlinear, quantum, and active silicon photonics. In particular, broadband resonance-enhanced frequency generation was successfully demonstrated using stimulated four-wave mixing and extended to entangled photon-pair generation through spontaneous four-wave mixing. These efforts move topological silicon photonics towards the development of efficient and robust on-chip quantum light sources. Additionally, pn-junctions integrated into the silicon microring lattice allowed for the investigation of modulated FDMR by the plasma effect. Finally, the coupling of many FDMR together was explored to route light across the TPI lattice. These nonlinear and active devices broaden the scope of applications of topological photonic insulators for

realizing robust photonic integrated circuits and quantum photonic circuits that are tolerant to device parameter variations.

Preface

Various parts of this thesis have previously been published in a book chapter, peer-reviewed journals, and conference proceedings.

Chapter 3 of this thesis contains content which has been published as S. Afzal, D. Perron, T. Zimmerling, Y. Ren, and V. Van, “Observation of anomalous Floquet insulator edge states in periodically-driven silicon photonic topological microresonator lattices,” in Frontiers in Optics + Laser Science APS/DLS, OSA Technical Digest (Optica Publishing Group, 2019), paper FM4E.4 and further published as Shirin Afzal, Tyler J. Zimmerling, Yang Ren, David Perron, and Vien Van, “Realization of Anomalous Floquet Insulators in Strongly Coupled Nanophotonic Lattices,” Phys. Rev. Lett. 124, 253601 (24 June 2020). I assisted with device simulation and design, as well as editing the manuscript and supplemental material. S. Afzal was responsible for the design, simulation, and measurement of devices, as well as the collection and analysis of experimental data. D. Perron assisted with device design. Y. Ren assisted with the experimental measurements. V. Van was the supervisory author and contributed to the ideation of the experiment and editing the manuscript.

Chapter 4 of this thesis contains content which has been published as T. J. Zimmerling, S. Afzal, and V. Van, “FWM Frequency Generation in Topological Floquet Defect Mode Resonance,” in Frontiers in Optics + Laser Science 2021, C. Mazzali, T. (T.-C.) Poon, R. Averitt, and R. Kaindl, eds., Technical Digest Series (Optica Publishing Group, 2021), paper FM2E.2 and further published as T. J. Zimmerling, S. Afzal, and V. Van , “Broadband resonance-enhanced frequency generation by four-wave mixing in a silicon Floquet topological photonic insulator”, APL Photonics 7, 056104 (2022). I was responsible for describing the FWM theory, performing the experiments, analyzing gathered data, developing simulated results and composing the manuscript. S. Afzal designed the devices tested, provided the FDMR theory, assisted with performing the experiments and assisted in developing simulated results. V. Van was the supervisory author and contributed to the ideation of the experiment and editing the manuscript.

Chapter 5 of this thesis contains content which has been published as S. Afzal, T. J. Zimmerling, V. Van, and S. Barzanjeh, "Resonance-Enhanced Entangled Photon Pair Generation Using Topological Floquet Defect Mode Resonance", CLEO 2023 (2023). I was responsible for experiment ideation, describing the FWM theory, assisting with experiments, developing simulated results and composing the manuscript. S. Afzal setup and ran the experiments, analyzed the gathered data, and assisted in composing the manuscript. V. Van was one of the supervisory authors and contributed to the ideation of the experiment and editing the manuscript. S. Barzanjeh was one of the supervisory authors and also contributed to the ideation of the experiment and editing the manuscript. This content has also been published in a pre-print as S. Afzal, T. J. Zimmerling, M. Rizvandi, M. Taghavi, T. Hrushevskyi, M. Kaur, V. Van and S. Barzanjeh, "Bright quantum photon sources from a topological Floquet resonance", arXiv:2308.11451 [quant-ph] (2023).

Chapter 7 of this thesis contains content which has been published as Tyler J. Zimmerling and Vien Van, "Generation of Hofstadter's butterfly spectrum using circular arrays of microring resonators," Opt. Lett. 45, 714-717 (2020). I was responsible for describing the theory, designing the devices, simulating the device performance, analyzing the results and preparing the manuscript. V. Van was the supervisory author and contributed to the ideation of the experiment and editing the manuscript.

"Do not go where the path may lead. Go instead where there is no path, and leave a trail for others to follow."

-Anonymous

Acknowledgements

I would like to thank my supervisor, Professor Vien Van, for his invaluable guidance and mentorship throughout my studies, exemplified through his assistance in experimental design and data analysis, his encouragement to think critically and troubleshoot problems, and his support in providing opportunities to present my research internationally and participate in collaborations that have led to the success of my research. I would like to thank my supervisory committee members, Professors Ying Tsui and Sandipan Pramanik, for their time and effort in reviewing my thesis, ensuring my research is of a high standard. I would like to thank my candidacy examiners, Professors John Davis and Robert Fedosejevs, for their time and effort in reviewing my candidacy report, providing important feedback and new insights on my research. I would like to thank my colleagues and co-authors, Dr. Shirin Afzal, Dr. Yang Ren, Dr. Huynh Ngo, David Perron, Dr. Shabir Barzanjeh, Dr. Masum Hossain, and Negin Memar. More specifically, I would like to thank Dr. Afzal and Dr. Ren for providing me countless lessons on theory and experimental procedure, demonstrating their understanding, patience, and belief in my research abilities. I would like to thank my labmates, Hanfa Song, Bo Leng, YouQian Li, Timothy Lee, and Boden Eakins. Specifically I would like to thank Hanfa for his ongoing support and encouragement in the lab. I would like to thank the Natural Sciences and Engineering Research Council of Canada (NSERC), the University of Alberta Faculty of Graduate Studies and Research (FGSR), Alberta Innovates, and SPIE for supporting my graduate studies through their various scholarships. Additionally, I would like to thank Optica for supporting my professional development through the 2019 Student Leadership Conference.

Table of Contents

List of Tables

List of Figures

List of Symbols

Constants

ε_o	Vacuum Permittivity	$8.854E-12\,F/m$
η_o	Vacuum Impedance	$377\,\Omega$
c	Speed of light in a vacuum	$299,792,458\,m/s$
e	Fundamental Charge	$1.626E-19\,C$
h	Planck's Constant	$6.62607015E-34\,Js$
m_e	Electron Mass	$9.11E-31\,kg$

Latin

A_{eff}	Effective Mode Area
C	Chern Number
E	Electric Field
F	Finesse
f	Frequency
k	Field Coupling Strength per Unit Length
L	Length
n	Index of Refraction
n_2	Kerr Coefficient
n_g	Group Index of Refraction
P	Optical Power
Q	Quality Factor
T	Period
w	Winding Number
Z_2	Integers Modulo 2 [0,1]

Greek

α	Propagation Loss Coefficient
β	Propagation Constant of the Waveguide
β_2	Group Velocity Dispersion (GVD)
χ^3	Third-Order Nonlinearity
$\Delta\phi$	Phase Detune
γ	Waveguide Nonlinearity Parameter
κ	Field Coupling Coefficient
Λ	Lattice Constant
λ	Wavelength
μ	Energy Coupling Coefficient
ω	Angular Frequency
τ	Field Transmission Coefficient
θ	Coupling Angle
ε	Quasienergy

Abbreviations

AFI Anomalous Floquet Insulator.

ASE Amplified Spontaneous Emission.

BPF Bandpass Filter.

CAR Coincidence-to-Accidental Ratio.

CE Conversion Efficiency.

CMOS Complimentary Metal-Oxide-Semiconductor.

CROW Coupled-Resonator Optical Waveguide.

CS Cauchy-Schwarz.

CW Continuous-Wave.

EDFA Erbium-Doped Fibre-Amplifier.

EOM Electro-Optic Modulator.

FCA Free-Carrier Absorption.

FCD Free-Carrier Dispersion.

FDMR Floquet Defect Mode Resonance.

FDTD Finite-Difference Time-Domain.

FSR Free Spectral Range.

FWM Four-Wave Mixing.

GVD Group-Velocity Dispersion.

LOQC Linear Optical Quantum Computing.

MRR Microring Resonator.

NIR Near-Infrared.

PGR Pair Generation Rate.

Q-factor Quality Factor.

RF Radio-Frequency.

ROR Ring-of-Rings.

SEM Scanning Electron Microscope.

SFWM Spontaneous Four-Wave Mixing.

Si Silicon.

SiO_2 Silicon Dioxide (Silica Glass).

SOI Silicon-on-Insulator.

SPD Single-Photon Detector.

SSH Su-Schrieffer-Heeger.

TE Transverse-Electric.

Ti/W Titanium-Tungsten.

TiN Titanium Nitride.

TM Transverse-Magnetic.

TPA Two-Photon Absorption.

TPI Topological Photonic Insulator.

WDM Wavelength Demultiplexer.

Glossary of Terms

Chern Number An integer static band invariant, calculated by integrating the Berry curvature of the n^{th} Bloch mode over the Brillouin zone of the momentum space of the lattice.

Entanglement A process whereby energetically degenerate states cannot be separated. Two entangled photons are inextricably linked regardless of temporal or spatial separation and measurement of one will determine characteristics of the other.

Floquet A mathematical theory analyzing time-varying systems as periodic systems, such as light propagating around a resonator.

Hamiltonian A mathematical description of the total energy state of a system.

Topological Exhibits properties that are preserved under continuous, adiabatic changes, such as a bandgap in an energy spectrum.

Winding Number An integer dynamical gap invariant which depends on the complete evolution history of the system over each driving period.

Chapter 1

Introduction

In this thesis, I will address the motivation for my research on Floquet defect mode resonance (FDMR), a new resonance phenomenon in anomalous Floquet topological photonic insulators (TPIs). Additionally, I will explore the applications of FDMR in nonlinear, quantum, and active topological silicon photonics. I will outline the objectives that directed this work and present my results to date, including design, fabrication, simulation, and experimental demonstrations. To conclude, I will propose future research directions for the development and application of anomalous Floquet insulators (AFIs) and FDMR in topological silicon photonics.

1.1 Motivation

In a world where fiber optics has revolutionized communication via the internet, integrated silicon photonics is leading a paradigm shift in optical communication and information processing. Augmenting and expanding microprocessor functionalities with optical signal processing circuits allows for computations to be carried out at the speed of light. Developing complex lightwave circuits for new applications, such as neuromorphic computing [1] and quantum information [2], is a major pursuit of integrated silicon photonics. However, as silicon photonic circuits grow in scale and complexity, their performance becomes more susceptible to device imperfections, such as those caused by fabrication variations and fluctuations in the operating environment. In order to overcome these challenges, recent research efforts have begun to focus on developing robust photonic devices that are tolerant to random variations and fabrication defects. Thanks to their resistance to defects, TPIs have emerged as a potential material platform for realizing robust photonic devices [3–13]. Though they remain sensitive to waveguide-level scattering, comparable to that of a conventional silicon waveguide, these devices maintain performance on the lattice-constant level. Despite this, few device applications of topological photonic insulators have been demonstrated thus far. This is partly due to the lack of some key elements of integrated photonics, such as high quality (Q)-factor resonances, which have yet to be realized in a topological photonic lattice. The research presented in this thesis aims to explore the generation and utilization of FDMR on a silicon TPI, contributing to the development of robust silicon photonic integrated circuits that are tolerant to device parameter variations.

1.2 Background and Literature Review

TPIs are artificial materials whose energy band structures exhibit nontrivial topological properties, similar to those of electronic wave functions in solid-state topological insulators [12, 14]. These bandgap insulators are characterized by certain nontrivial topological invariants [15, 16] which identify global attributes of the device which do not change as some physical parameters are varied. Topological insulators have attracted a great deal of interest recently as the existence of topologically-protected edge modes at sample boundaries provide a unique solution to disorder, which poses a challenge in many applications of large-scale integrated photonic circuits [17–19]. These high-transmission states cross energy bandgaps, are localized to the edge of the insulator, and are immune to lattice disorder. This exotic property of TPIs could be used to realize robust optical devices and other novel applications [20–22].

The development of topological insulators stems from the discovery [23] and further study [24, 25] of the quantum Hall effect, leading to the classification of materials based on their topological order [26]. For more complex systems, a Z_2 topological invariant was developed by considering the quantum spin Hall effect in graphene [27, 28]. Haldane and Raghu [29, 30] were the first to propose analogues of quantum Hall systems in the photonic domain, describing a one-way photonic waveguide equivalent to the chiral edge states under the quantum Hall effect. Topological insulator behaviours in bosonic systems were first observed at microwave frequencies by applying an external magnetic field to a gyromagnetic photonic crystal to break the time reversal symmetry [3]. This was soon followed by a theoretical and experimental demonstration of an adiabatically modulated photonic quasicrystal exhibiting topological edge states [4].

The effect of the magnetic field is weak at optical frequencies, thus, the first TPI was realized by emulating an effective magnetic field for photons using a synthetic gauge field [5, 6]. Topological photonic insulators on the microring lattice platform were first proposed [7] and demonstrated [8] through a combination of site resonators and off-resonance link resonators. Soon after, strongly coupled microring lattices were also explored [9]. Since then, the study of TPIs in integrated photonic lattices has been a very active area of research [10–13]. There have also been realizations of TPIs in zero net magnetic field by introducing a local gauge field using next-nearest neighbor hoppings or by breaking the spatial symmetry through a deformation of the unit cell [31–36]. All of these realizations of TPIs are based on static systems with time-independent Hamiltonians.

These static systems form a complete class of topological insulators called Chern insulators (CIs) and have been explored experimentally [37, 38]. However, there exist systems beyond this class of static TPIs which offer the advantage of being more versatile. In particular, Floquet TPIs [39, 40], which are based on periodically-driven quantum systems, can exhibit much richer topological behaviors than static systems. Floquet systems can support not only conventional CI behaviour [6, 41], but also AFI edge modes in the bandgaps between energy bands with trivial Chern number [42–50]. This AFI phase is not observed in time-independent topological insulators. In addition, Floquet systems are more versatile than static systems, since their topological behaviours can be tailored through suitable design of the driving Hamiltonian. AFIs have been demonstrated at acoustic and microwave frequencies using strongly-coupled ring resonators [44, 45] and at optical frequencies using 2D arrays of periodically-coupled waveguides [46, 51, 52]. For the photonic AFIs based on waveguide arrays, since many periods are required to observed Floquet topological behaviours, the waveguides must have long lengths, typically in the range of centimeters, making them unsuitable for implementation on an integrated photonics platform.

1.2.1 Implementations and Applications of Topological Photonic Insulators

TPIs can potentially have practical applications in realizing photonic devices that are robust to lattice-level imperfections by exploiting the topological protection property of the edge modes [53–55]. In the optics domain, TPIs have been demonstrated using coupled waveguide arrays [41, 46, 51, 52, 56, 57] and 2D microring lattices [7, 8, 55, 58–61].

The first experimental observation of a Floquet TPI in any physical system was realized optically using topologically-protected unidirectional edge states in 2013, without magnetic fields, using a honeycomb photonic lattice of helical waveguides [41]. The structure was made in fused silica using femtosecond-direct-laser writing and had a propagation length of 10 cm. Figure 1.1 shows a micrograph of the input of the lattice, a schematic diagram of the helical waveguides, the band structure of the lattice when the waveguides are straight versus helical, and the group velocity versus the helix radius. The structure follows a tight-binding model and constitutes the first observation of a field-free TPI. This structure functions by applying a time-periodic potential to the system, requiring no spin-orbit coupling in order to achieve topological protection, a novel "Floquet" TPI.

In 2017, a coupled waveguide array was implemented such that the Chern numbers of all bands were zero, however chiral edge modes still existed [51]. By employing periodically-driven photonic waveguide lattices, topologically-protected and scatter-free edge transport was demonstrated in an "anomalous" Floquet TPI. This structure of single-mode waveguides was written inside a high-purity, 15 cm-long fused silica wafer using a femtosecond

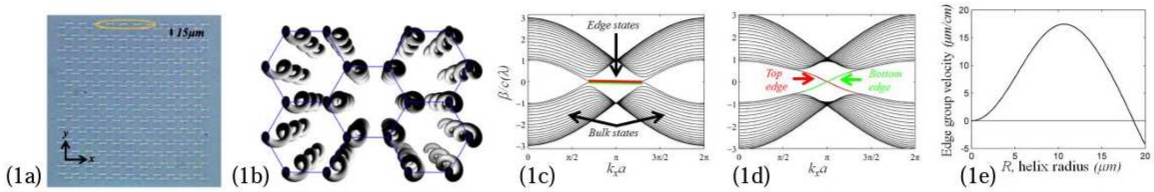

Figure 1.1: From [41], a micrograph of the input of the lattice, a schematic diagram of the helical waveguides, the band structure of the lattice when the waveguides are straight versus helical, and the group velocity versus the helix radius.

laser. Figure 1.2 shows the coupling steps that take place as light travels through the lattice, the formation of localized bulk modes and chiral edge modes along the lattice boundaries, a schematic of the sample, and the edge and bulk band structures. This work demonstrated the significance of calculating the winding number in determining the topological characteristics of periodically driven systems.

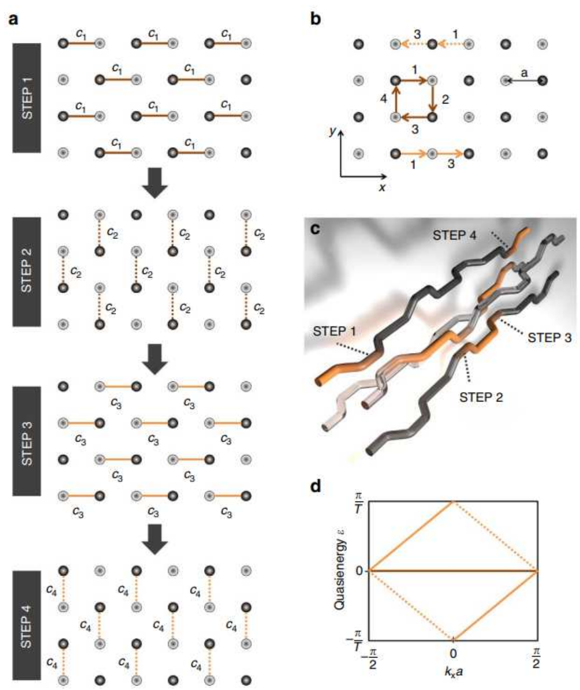

Figure 1.2: From [51], the coupling steps that take place as light travels through the lattice, the formation of localized bulk modes and chiral edge modes along the lattice boundaries, a schematic of the sample, and the edge and bulk band structures.

Closely related to these results, also in 2017, another coupled waveguide array demonstrated anomalous topological edge modes [46]. This photonic lattice, with two distinct driving periods, was fabricated inside a 7 cm-long glass substrate using ultrafast laser inscription. This devices differs from the last as the asymmetric coupling in x and y introduces a rich, yet simple model to explore many different topological regimes. Figure 1.3 presents a sketch illustrating the different regimes of driving frequency, the four coupling steps and their cyclic driving protocol, the chiral edge modes and localized bulk mode, a sketch of the device, and a white-light transmission micrograph of the lattice facet. This work introduces the generalized model which allows the coupling strength in one axis to differ from that in another.

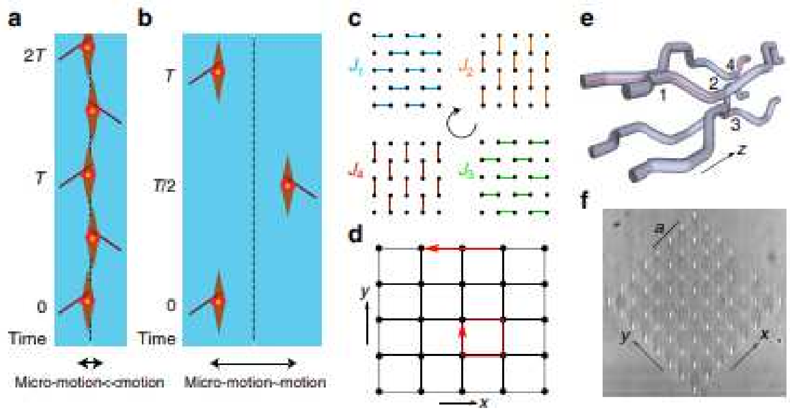

Figure 1.3: From [46] a sketch illustrating the different regimes of driving frequency, the four coupling steps and their cyclic driving protocol, the chiral edge modes and localized bulk mode, a sketch of the device, and a white-light transmission micrograph of the lattice facet.

This same group in 2018 implemented a coupled waveguide array inside of a cavity, allowing the optical state to evolve through the lattice multiple times [52]. Figure 1.4 shows a sketch illustrating linear and ring state-recycling techniques, a one-dimensional driven lattice whose coupling strengths vary in time, a schematic of said lattice implemented on a photonics platform in a linear cavity, the band diagram of such a device, and the excitation of a linearly dispersive band sampled at various effective propagation distances. This device provided one solution to the limitation of propagation distance in these coupled waveguide arrays and allowed for the exploration of long timescale/propagation distance effects. This setup also had the benefit of being able to sample effective dynamics in a quasi-real-time or stroboscopic manner, taking snapshots of the system at periodic intervals.

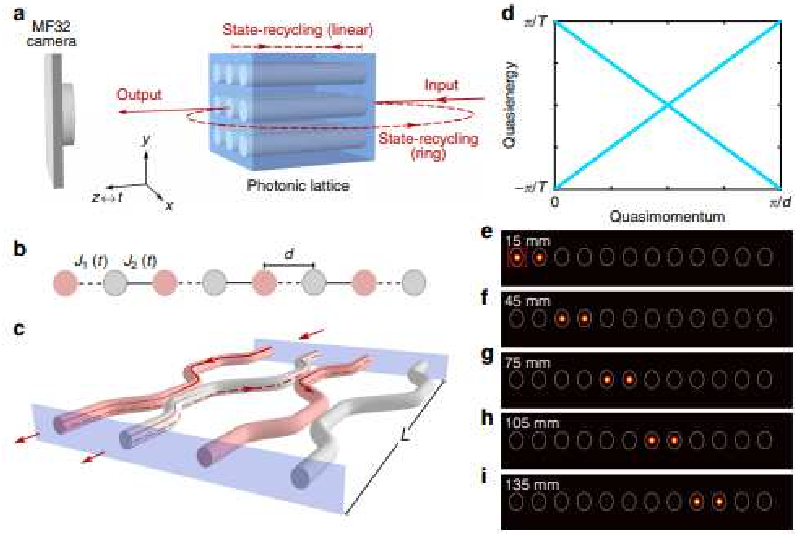

Figure 1.4: From [52], a sketch illustrating linear and ring state-recycling techniques, a one-dimensional driven lattice whose coupling strengths vary in time, a schematic of said lattice implemented on a photonics platform in a linear cavity, the band diagram of such a device, and the excitation of a linearly dispersive band sampled at various effective propagation distances.

With the well-established defect-resistant nature of topological modes, the distinction between static and time-varying defects was explored in coupled waveguide arrays as well [56]. These arrays were fabricated via direct laser writing in a negative tone photoresist, later infiltrated with SU8-2 which is baked to form the solid waveguides about 500 μm long. Figure 1.5 shows scanning electron micrographs of the top and side of the structure, as well as a timelapse of SU8-2 infiltrating the unfilled waveguides. It was found that a Floquet system of periodically-coupled helical waveguides continued to support a chiral edge state under a single dynamic defect, even when the temporal modulation was strong. This research also suggests that scattering of edge modes into bulk modes should be possible, if the introduced defect has a quasienergy matching that of the bulk band. This could be achieved by tuning the effective refractive index of that defect waveguide.

More recently, nonlinearity has also been explored in Floquet TPIs, with solitons being observed in a waveguide array with periodic variations along the waveguide axis [57].

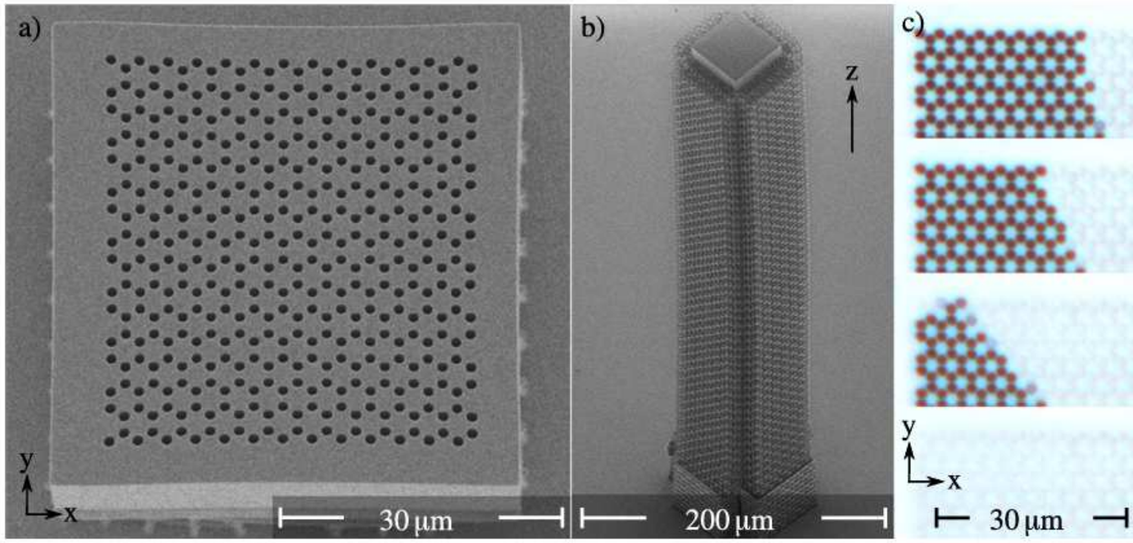

Figure 1.5: From [56], scanning electron micrographs of the top and side of the structure, as well as a timelapse of SU8-2 infiltrating the unfilled waveguides.

These periodic variations gave rise to a nonzero winding number, enabling topologically nontrivial behaviour, while the nonlinearity arose from the optical Kerr effect. The solitons executed cyclotron-like orbits associated with the underlying topology. This device was fabricated using femtosecond laser writing inside a borosilicate glass. Figure 1.6 shows the periodically driven square lattice with four equal couplings, a schematic of the three-dimensional waveguide array, a quasi-energy spectrum of the linear regime of the lattice, and a micrograph of the facet of the photonic square lattice.

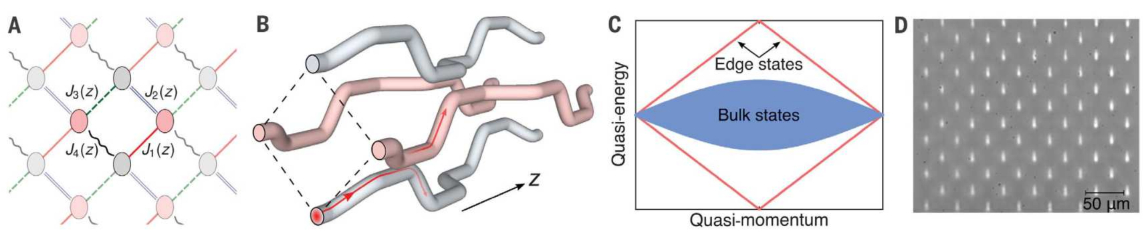

Figure 1.6: From [57], the periodically driven square lattice with four equal couplings, a schematic of the three-dimensional waveguide array, a quasi-energy spectrum of the linear regime of the lattice, and a micrograph of the facet of the photonic square lattice.

2D microring lattices were first proposed for implementing TPI's in 2011 using a system of site rings and off-resonance link-ring-couplers [7]. It was demonstrated that key characteristics such as the Hofstadter butterfly and robust edge state transport could be obtained on a device consisting of a network of coupled resonator optical waveguides (CROW). Figure 1.7 shows simulations of light intensity for counter-clockwise and clockwise one-way edgemodes propagating along the boundary of a 2D lattice, as well as avoiding a defect along the bottom edge. Specifically, this work looked to improve the performance of optical delay lines and overcome limitations on photonic device performance introduced by disorder in photonic technologies.

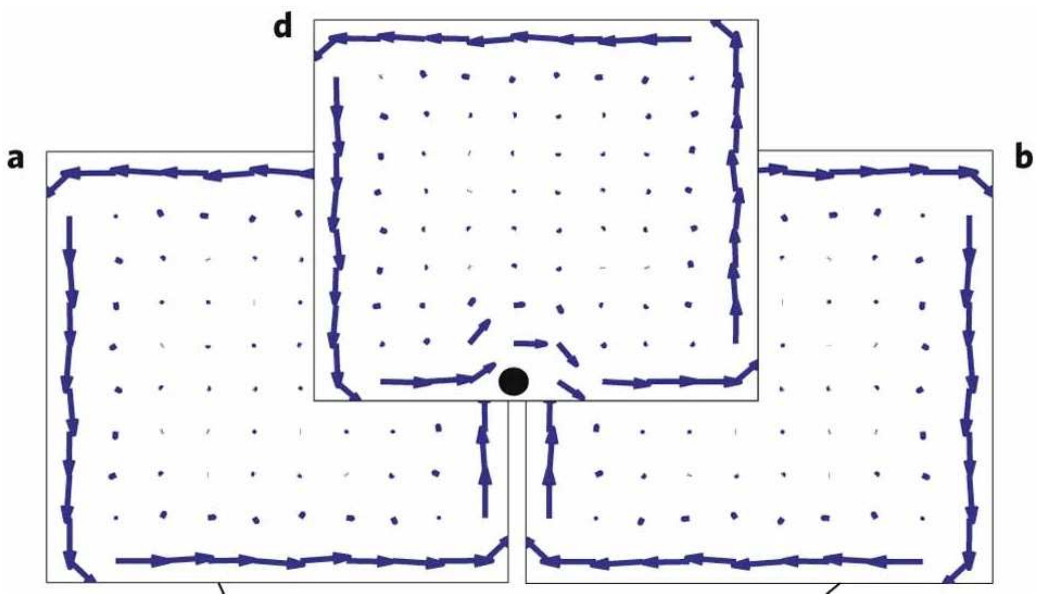

Figure 1.7: From [7], simulations of light intensity for counter-clockwise and clockwise one-way edgemodes propagating along the boundary of a 2D lattice, as well as avoiding a defect along the bottom edge.

This structure was then implemented experimentally by the same group in 2013, fabricating a 2D array of coupled microring resonators on an SOI substrate [8]. This structure realized an effective magnetic field for photons at room temperature, allowing for the first observation of topological edge states of light in a 2D system. Figure 1.8 shows an SEM image of the lattice, with a site-ring resonator intentionally removed, forming a significant introduced defect. This device was demonstrated to be robust against both intrinsic and introduced disorder in lattice coupling strength and phase. This device also demonstrated that the SOI platform was promising for exploring topological effects as it allowed for the measurement of both transmission spectra and spatial mode distribution.

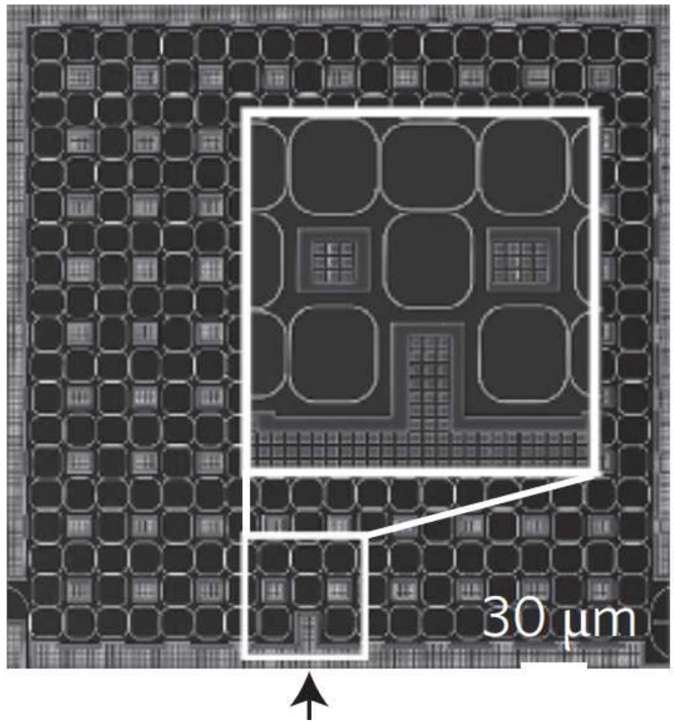

Figure 1.8: From [8], an SEM image of the lattice, with a site-ring resonator intentionally removed, forming a significant introduced defect.

Further exploration of this device allowed for the determination of the distribution of photon transport properties in the lattice [58]. This investigation confirmed that localization occurred dominantly in the bulk of the lattice and was suppressed in edge states along the lattice boundary. Figure 1.9 shows an SEM image of the 2D lattice connected to the measurement setup schematic, as well as an SEM image of a 1D device and simulated mode distributions of edge modes and bulk modes across 8x8 and 15x15 microring lattices.

This kind of 2D lattice of microring resonators has also been demonstrated to realize topological edge states and use them to generate correlated photon pairs by spontaneous four-wave mixing [59]. The spectral robustness of this device outperformed similar, yet topologically-trivial, 1D arrays of microrings. Figure 1.10 shows an SEM image of an 8x8 lattice of site-ring and link-ring resonators, with the unit cell highlighting the site rings in cyan and the link rings in yellow. The clockwise mode follows the longer red outline along

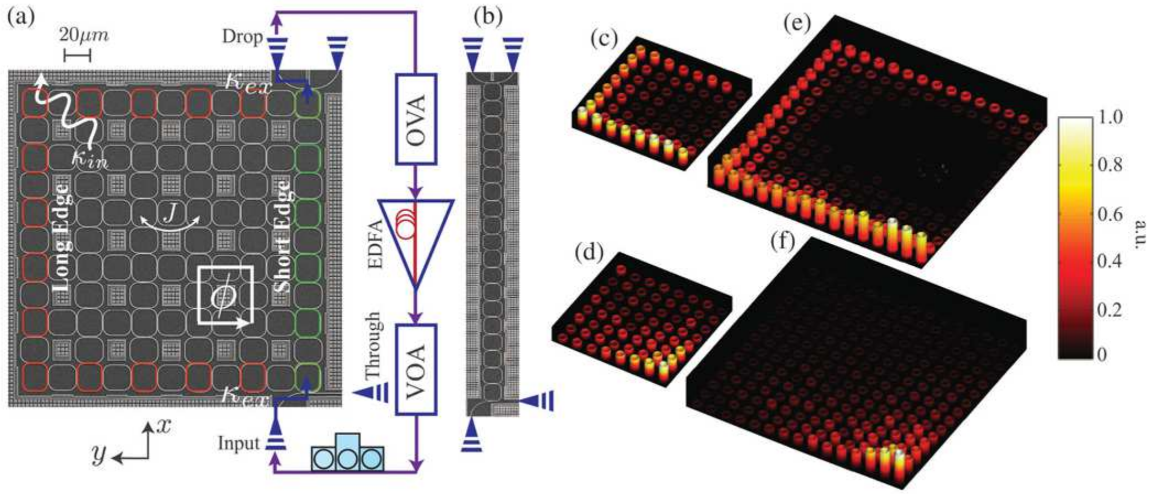

Figure 1.9: From [58], an SEM image of the 2D lattice connected to the measurement setup schematic, as well as an SEM image of a 1D device and simulated mode distributions of edge modes and bulk modes across 8x8 and 15x15 microring lattices.

the upper edge of the lattice while the counter-clockwise mode follows the shorter green outline along the lower edge. This work demonstrated a topological source of correlated photon pairs, with a spectral distribution robust against the disorder of lattice-coefficients introduced through fabrication.

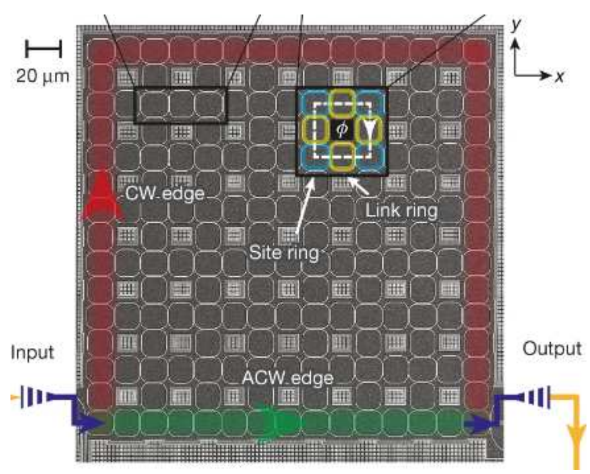

Figure 1.10: From [59], an SEM image of an 8x8 lattice of site-ring and link-ring resonators, with the unit cell highlighting the site rings in cyan and the link rings in yellow.

This work was expanded upon to demonstrate energy-time entangled photons with tunable spectral bandwidths [61]. The two input pump wavelengths were tuned across respective flat, high-transmission edge modes. The bandwidth of the spectrum of generated photon pairs was controlled by the spectral location of the input pump waves relative to the edge mode. Figure 1.11 shows a schematic of the 2D lattice with site-rings and link-rings, with the supporting experimental setup, simulated transmission and delay spectra with the edge mode in green and the bulk modes in blue, and the pumping scheme used to generate indistinguishable photon pairs using stimulated four-wave mixing. This work set the stage for the on-chip generation of quantum states where topology allows for the robust manipulation of photons.

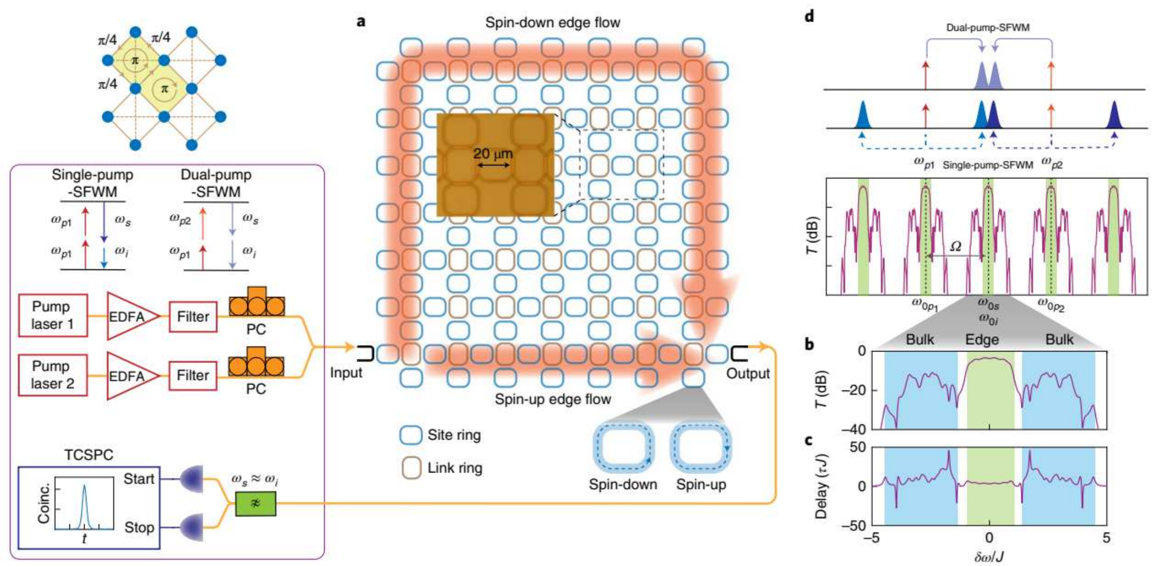

Figure 1.11: From [61], a schematic of the 2D lattice with site-rings and link-rings, with the supporting experimental setup, simulated transmission and delay spectra with the edge mode in green and the bulk modes in blue, and the pumping scheme used to generate indistinguishable photon pairs using stimulated four-wave mixing.

Most recently, the robustness to implemented defects was tested using entangled photon pairs on a photonic anomalous Floquet TPI using non-trivial edge modes [55]. This device demonstrated that entanglement could be topologically protected against artificial structure defects. Figure 1.12 shows a diagram and optical microscope image of the 2D lattice with experimental setups to measure the degenerate and non-degenerate cases of FWM, as well as SEM of a waveguide, optical microscope images of the microrings, and the grating coupler. The strongly-coupled anomalous Floquet TPI lattice supports clockwise and counter-clockwise edge modes highlighted in yellow and green, respectively. This device furthers the work on topological photon-pair sources in insulator lattices.

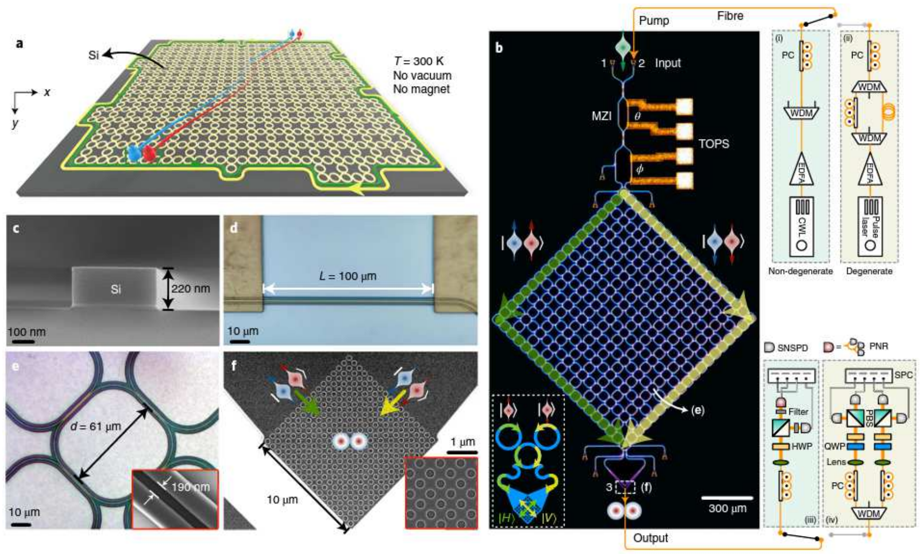

Figure 1.12: From [55], a diagram and optical micrscope image of the 2D lattice with experimental setups to measure the degenerate and non-degenerate cases of FWM, as well as SEM of a waveguide, optical microscope images of the microrings, and the grating coupler.

Demonstrations of TPI applications include the realization of robust optical delay lines [7], all-optical signal processing [62], optical isolators [63], and lasing [64, 65]. There has also been growing interest in achieving parametric processes on a TPI platform, exploiting the topological protection of edge modes to realize robust wavelength sources and frequency converters [53, 55, 59, 66–69]. For example, one-dimensional arrays of silicon nanodisks emulating the generalized Su–Schrieffer–Heeger (SSH) model have been used to obtain enhanced third-harmonic generation at telecom frequencies through Mie resonances and the topological localization of edge states [68]. Plasmonic metasurfaces, consisting of 2D hexagonal arrays of nanoholes in graphene sheets under a static magnetic field, have been shown to form Chern insulator edge states and were used to achieve FWM in the 13 THz frequency range [69]. Spontaneous FWM using edge modes in a Chern insulator based on a 2D lattice of silicon ring resonators has been demonstrated for correlated photon-pair generation [59]. Entangled-photon emitters have also been achieved by FWM in a silicon AFI microring lattice [55]. None of these previous works employed resonance effects to enhance nonlinear processes on a topological platform.

1.2.2 Resonance in Topological Photonic Insulators

As optical resonators are an important device in many photonic applications, there has been a great deal of interest in realizing high-Q resonators in a topological photonic platform that are robust to lattice-level defects. Topological resonators have been explored through propagation of topologically protected edge modes in a loop to form a ring cavity [20, 21]. These resonances are characterized by very long path lengths, leading to small FSRs and low Q-factors.

Topologically protected edge modes can be formed in arbitrary geometries by fabricating photonic crystals with trivial and nontrivial bandgaps adjacent to either, resulting in a boundary across which a topological invariant changes. At telecommunication wavelengths, integrated nonreciprocal topological cavities have been demonstrated to couple stimulated emission from one-way photonic edge states to a selected waveguide output [20]. In this work, the structure was made of InGaAsP multiple quantum wells bonded on an yttrium iron garnet substrate, which was used to break time-reversal symmetry in a system when exposed to a static external magnetic field. Figure 1.13a shows a top-view SEM of the fabricated arbitrarily-shaped topological cavity, Fig. 1.13b shows an image of the device with the external optical pumping and magnetic field turned on, with the boundary clearly occupied by the light, Fig. 1.13c demonstrates the difference in emission power isolation when the direction of applied magnetic field is flipped, and Fig. 1.13d shows the lack of an edgemode when the magnetic field is absent, effectively closing the nontrivial bandgap of the photonic crystal lattice. This work demonstrated the flexibility of topological photonic cavities.

The first observation of topologically-protected edgemode lasing in nonmagnetic, 2D topological cavity arrays was presented in 2018 [21]. Such a magnet-free implementa-

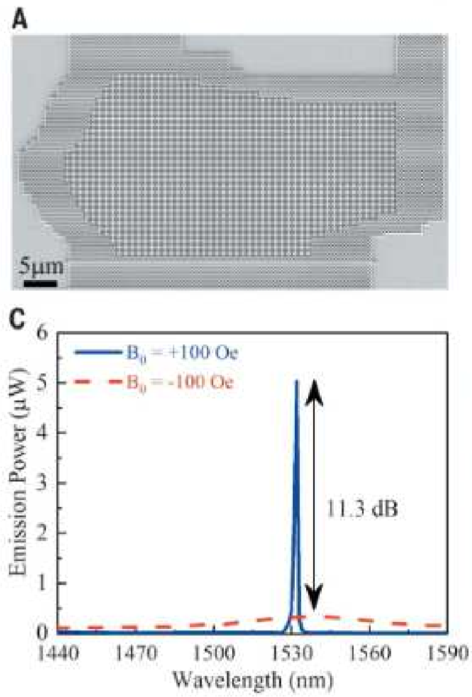

Figure 1.13: From [20], a top-view SEM of the fabricated arbitrarily-shaped topological cavity, an image of the device with the external optical pumping and magnetic field turned on, with the boundary clearly occupied by the light, the difference in emission power isolation when the direction of applied magnetic field is flipped, and the lack of an edgemode when the magnetic field is absent.

tion was more compatible with fabrication processes and photonic integration with lossless components, as well as provided an expanded topological bandgap. This device was implemented using InGaAsP quantum wells on an active platform. The lattice was formed through site rings and link rings, where a phase shift was introduced through the link rings to provide a synthetic magnetic field and establish topologically nontrivial bandgaps. Figure 1.14a shows a microscope image of the topological 10 by 10 unit cell microresonator array, Fig. 1.14b shows an SEM image of the outcoupling grating used to sample the spectral output of the lattice, Fig. 1.14c shows an SEM image of a single site ring surrounded by four link rings, and Fig. 1.14d shows a schematic of the topological array when pumped along the perimeter of the lattice to promote lasing of the topological edge mode. This work experimentally demonstrated that topological protection can lead to higher efficiency than trivial counterparts and the bypassing of defects, providing a route for the development of arrays of semiconductor lasers.

Contrary to these resonances, defect mode resonances are spatially localized to a few unit cells in the lattice and have achieved Q-factors up to 10^6 in silicon membrane photonic crystal nanocavities [70]. Defect modes have been demonstrated in static lattices with point and line defects [71–74]. These defects are time-independent, with no periodicity in time in either the defect, the lattice, or both, with few explorations of dynamic defects in a static lattice [56].

1.3 Thesis Objectives

The broad objective of my research is to investigate TPIs and identify their potential applications. We consider a periodic defect in a periodically-driven lattice, giving rise to FDMR. The novel FDMR [75, 76] is a resonance mode whose spatial distribution is governed by the hopping sequence of the lattice, not by the presence of an interface. This FDMR represents a periodic defect in the TPI lattice, which differs from a static defect studied in other devices [71–74].

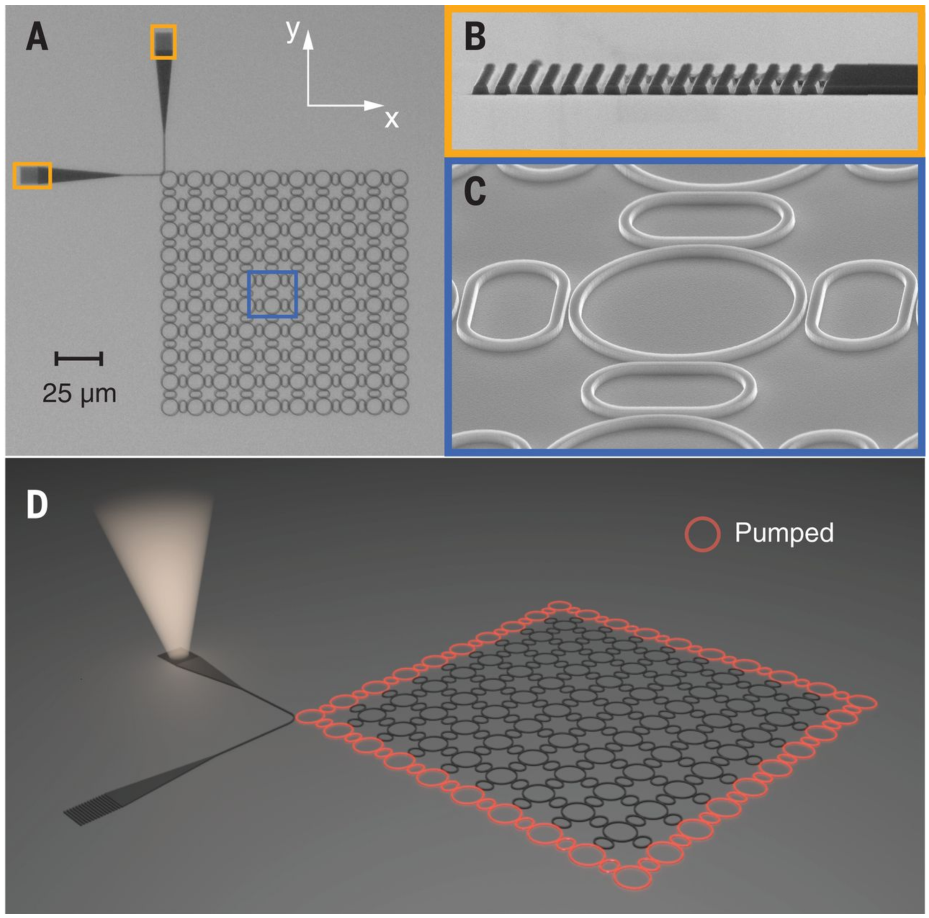

Figure 1.14: From [21], a microscope image of the topological 10 by 10 unit cell microresonator array, an SEM image of the outcoupling grating used to sample the spectral output of the lattice, an SEM image of a single site ring surrounded by four link rings, and a schematic of the topological array when pumped along the perimeter of the lattice to promote lasing of the topological edge mode.

Specifically, my focus is to explore how AFIs and FDMR can enable the realization of defect-resistant integrated silicon photonic devices in order to contribute to advancements in both classical and quantum communication applications. Furthermore, I aim to investigate how the dependence on added phase detune allows the resonant frequency and quality factor of the resonance to be tuned as desired. This research strives to evaluate the spectral characteristics and phase-dependence of FDMR and identify how FDMR can provide the foundation for robust integrated silicon photonic devices through topologically-protected modes. The tunability, high-Q and compact nature of FDMR could enable new applications of Floquet TPIs in integrated photonics. Namely, this research investigates the advantages and challenges associated with potential applications of FDMR in frequency generation, entangled photon pair generation, optical switching, and modulation.

1.4 Thesis Outline

This report outlines my efforts in realizing AFI topological photonic lattices and my experimental investigation of a novel resonance phenomenon induced in this lattice, FDMR, all on the silicon-on-insulator (SOI) platform. This chapter provides a brief introduction to this thesis and Chapter 2 will cover the necessary background information and theory on Floquet TPIs.

The first component of my research, Chapter 3, investigates the design, fabrication, and experimental demonstration of silicon photonic AFI microring lattices. These lattices formed the devices which later provided the initial demonstration of FDMR, using octagon resonators to achieve a Q-factor of 20,000, while our most recent rounded-square lattice achieved Q-factors up to 100,000. As many important applications in integrated silicon photonics, such as filtering and nonlinear frequency conversion, require high-Q resonators, optimization of the microring lattice design was key to reducing losses and maximizing the applications of the FDMR.

Chapters 4 and 5 explore nonlinear and quantum applications of FDMR by demonstrating frequency generation and entangled photon-pair generation through FWM in a silicon topological photonic lattice. High-Q FDMRs can enable efficient nonlinear applications based on third-order optical nonlinearities in silicon. In particular, Chapter 4 describes resonance-enhanced frequency generation through stimulated FWM. The results of this experiment enabled the exploration of entangled photon-pair generation on a topological photonics platform for quantum photonics applications. To this end, Chapter 5 describes resonance-enhanced entangled photon pair generation using the topological FDMR and spontaneous FWM.

Chapter 6 explores active photonic applications of FDMR with embedded pn-junctions and metallic heaters. The design, implementation, and demonstration of these active applications, such as optical signal modulation, have not yet been demonstrated on a topological photonic platform. By embedding pn-junctions selectively into our silicon microring lattice, the resonant frequency of the generated FDMR could be varied at high speed using the plasma effect (through free carrier injection). This could be used to realize fast optical switches and modulators, which have applications in both classical and quantum communication systems. Furthermore, generating multiple FDMR using heaters placed across the bulk of the lattice provides the opportunity to form a pseudo-CROW structure. This implementation allows for the exploration of another useful integrated silicon photonics device on a topological platform which could be used to form complex routing across a TPI lattice.

Investigating the theoretical extremes of a psuedo-infinite lattice, Chapter 7 explores the generation of Hofstadter's butterfly spectrum. This spectrum describes the energy bands of electrons in a two-dimensional periodic lattice with a perpendicular magnetic field, a topological system that eventually led to the discovery of the quantum Hall effect. In the optical domain, we implement a circular array of microring resonators, forming a 2D topological microring system with a synthetic dimension formed by the periodic variation of the microring resonance frequency.

TPIs offer an exotic platform for exploring new device applications in integrated silicon photonics. FDMR provides a novel method for realizing compact, high-Q and tunable resonators that benefit from the robustness of the topological platform. Our research focuses on nonlinear, quantum, and active photonic applications of FDMR, which have been little explored and could open new directions toward realizing silicon photonic integrated circuits for classical and quantum applications that are robust to lattice-level variation. We will look at the current research progress towards Floquet TPI lattices using the SOI fabrication platform and identify where we have furthered the field. I will summarize the key findings of my research on FDMR and its applications in nonlinear, quantum, and active topological silicon photonics. Finally, Chapter 8 will propose future research directions in the development and application of TPIs and FDMR in silicon photonics.

Chapter 2

Floquet Topological Photonic Insulator Theory

Here, we will review the theory of topological photonic insulators (TPIs) with a focus on those realized by microring lattices. We will derive the equations of motion describing a periodically-driven Floquet microring TPI in 2D and discuss its band structure and the topological invariants associated with the bands and bandgaps. We will then discuss the generation of Floquet defect mode resonance (FDMR) through a periodic perturbation to the Hamiltonian of the Floquet lattice.

2.1 Anomalous Floquet Topological Photonic Insulators

We consider a 2D square lattice of microring resonators with identical resonant frequencies. Each microring is assumed to support only one propagating mode in either the clockwise or counter-clockwise direction, which may be regarded as a "pseudo-spin" state. Each microring is coupled to its neighbours through evanescent field coupling between the waveguide modes. The strength of coupling between two resonators is defined by coupling angle θ such that the fraction of power coupled from one waveguide to the other is given by $\kappa^2 = \sin^2(\theta)$. Each coupling junction acts as a directional coupler, where the direction of propagation in one microring dictates the direction of propagation in the next, with the pseudo-spin of each site alternating like a set of spinning gears. In our work, the lattice is based on a general unit cell consisting of four microrings, A, B, C, and D as shown in

Fig. 2.1a. The lattice is thus translationally invariant, with a periodicity of Λ, the width of the unit cell, in both the x and y directions. Within each unit cell, the coupling between microring A and its neighbours, θ_a, generally differs from the coupling between microring D and its neighbours, θ_b. By tuning θ_a and θ_b, we can realize different topological phases in the lattice, including normal insulator (NI), Chern insulator (CI), and anomalous Floquet insulator (AFI) [50].

The topological behaviour of a 2D static system is fully characterized by the Chern number. The Chern number of quasienergy band n is an integer topological invariant which is calculated by integrating the Berry curvature of the n^{th} Bloch mode, $|\Psi_n(\mathbf{k})\rangle$, over the Brillouin zone of the momentum space of the lattice, k_x and k_y. Wrapping momentum-space into a torus (so that the points at $k_x = 0$ join the points at $k_x = 2\pi/\Lambda$ and $k_y = 0$ join the points at $k_y = 2\pi/\Lambda$), we integrate

$$C_n = \frac{1}{2\pi}\int_{BZ}(\nabla_{\mathbf{k}} \times \mathbf{A} \cdot \hat{\mathbf{k}}_z)dk_x dk_y = \frac{1}{2\pi}\int\int(\partial_{k_x}A_y - \partial_{k_y}A_x)dk_x dk_y \tag{2.1}$$

where ∂_k is the partial derivative with respect to k, $\nabla_{\mathbf{k}} \times \mathbf{A}$ is the Berry curvature ($\nabla_{\mathbf{k}}$ is the gradient with respect to $\mathbf{k}$) and $\mathbf{A}$ is the Berry phase connection defined as

$$\mathbf{A} = -i\langle\psi_n(\mathbf{k})|\nabla_{\mathbf{k}}|\psi_n(\mathbf{k})\rangle \tag{2.2}$$

To completely characterize the topological behaviors of a 2D Floquet system, we need to determine the integer dynamical gap invariant, or winding number, which depends on the complete evolution history of the system over each driving period. For a 2D lattice, the winding number associated with a bandgap at quasienergy ξ is given by [42]

$$w[U_\xi] = \frac{1}{8\pi^2}\int_0^L dz \int_{BZ} dk_x dk_y \mathrm{Tr}\left\{U_\xi^{-1}\partial_z U_\xi [U_\xi^{-1}\partial_{k_x}U_\xi, U_\xi^{-1}\partial_{k_y}U_\xi]\right\} \tag{2.3}$$

where U_ξ is the periodized evolution operator with an open bandgap around ξ. We can periodize the evolution operator $U(\mathbf{k},z)$, such that $U(\mathbf{k},L) = I$, by multiplying it with an operator V_ξ [42]

$$U_\xi(\mathbf{k},z) = U(\mathbf{k},z)V_\xi(\mathbf{k},z) \tag{2.4}$$

where

$$V_\xi(\mathbf{k}) = e^{iH_{eff,\xi}(\mathbf{k})z} \tag{2.5}$$

with the eigenvalues of the effective Hamiltonian $H_{eff,\xi}$ chosen to be between ξ and $\xi + 2\pi/L$. The winding number is equal to the number of edge modes that can exist in the bandgap. In addition, the Chern number of the n^{th} Floquet band is related to the winding number of the upper (ξ') and lower (ξ) bandgaps via the equation $C_n = w[U_\xi] - w[U_{\xi'}]$.

A TPI lattice exhibits AFI behaviour when the winding numbers are nontrivial even though the Chern numbers indicate the bands would be trivial in a static system. In particular, to achieve AFI bandgaps, we need to satisfy $\theta_a^2 + \theta_b^2 \gtrsim \pi^2/8$. In early work, the different coupling strengths were achieved by using asymmetrical coupling between different waveguide widths in an octagon resonator. We can take the extreme design choice of setting $\theta_b \equiv 0$ to simplify our fabrication. Not only does this allow for the removal of ring D, but we can simplify the resonators to rounded squares with identical coupling at every junction. This results in lower coupling loss between resonators and less propagation loss in the resonators themselves. In this design iteration, the unit cell of our device consists of three microrings, A, B, and C, as pictured in Fig. 2.1a with microring D in orange removed. This three-ring unit cell allows all three bandgaps to exhibit AFI behaviour for $\theta_a \gtrsim \pi/\sqrt{8}$, as shown in the band diagram in Fig. 2.1b. The winding numbers of all bandgaps are nontrivial (equal to 1) for $\theta_a > \pi/\sqrt{8}$ while the Chern numbers of all bands are trivial (equal to 0). This is the defining characteristic of the AFI phase, where the static model, based on the Chern numbers of the bands above and below the bandgap of interest, indicates the bandgap should be a normal insulator, while the periodic model, based on the winding number of the bandgap, indicates the bandgap should exhibit topological behaviour. The spatial distribution of the edge mode excited in one of these nontrivial bandgaps is represented by the light-blue shaded region in Fig. 2.1c.

To show that the microring lattice emulates a periodically-driven quantum system, we derive its Floquet-Bloch Hamiltonian by first transforming the lattice into an equivalent 2D

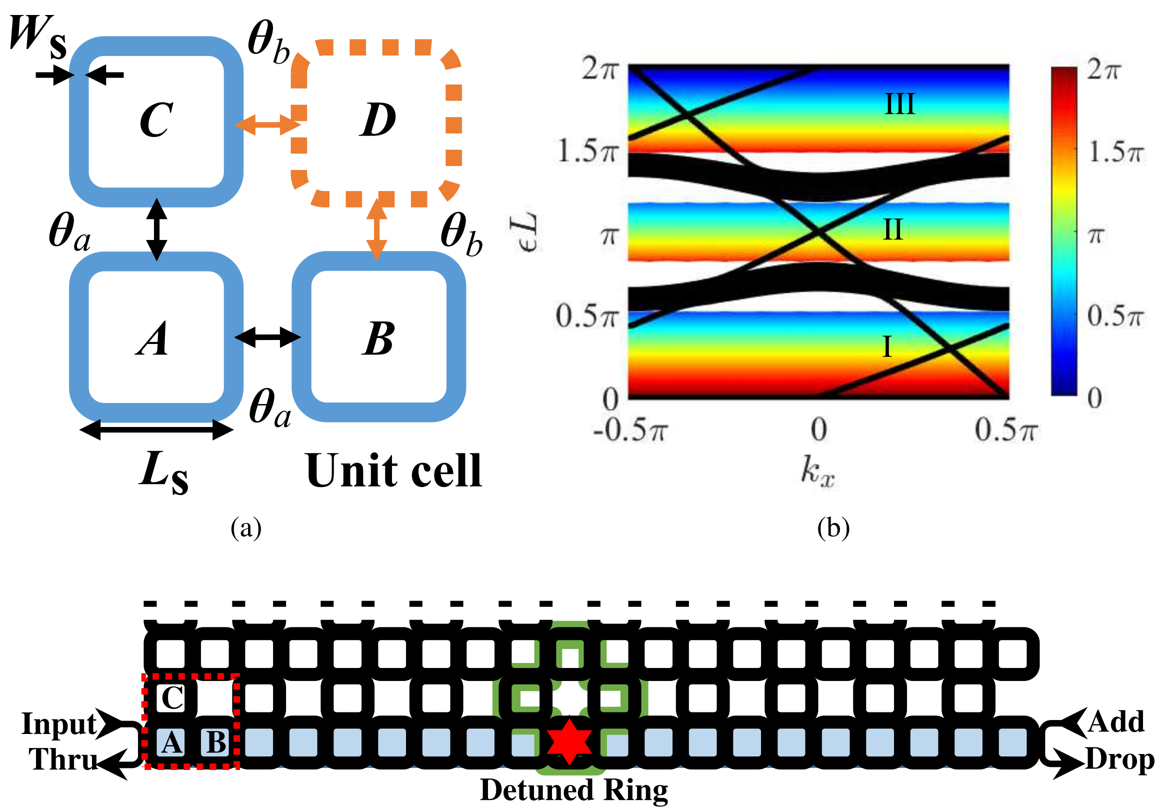

(a) (b)

(c)

Figure 2.1: (a) Schematic of 2D Floquet microring lattice with each unit cell consisting of 3 identical microrings A, B, C with neighbor coupling angle θ_a. The 4th microring D is omitted, setting $\theta_b \equiv 0$. (b) Projected quasienergy band diagram of a Floquet lattice with $\theta_a = 0.441\pi$ showing all 3 bandgaps hosting AFI edge modes. The colored gradients depict FDMR quasienergy bands which move across the bandgaps with increasing phase detune $\Delta\phi$ applied to the defect ring. (c) Unit cell shown in red, the edge mode in blue, and the FDMR loop in green, which is excited by applying a phase detune to the defect microring (red star). Adapted from [77].

coupled waveguide array [50]. This is achieved by "cutting" each microring in a unit cell at the points indicated by the small open circles in Fig. 2.2a and unrolling it into a straight waveguide with length L equal to the circumference of the microring, as shown in Fig. 2.2b. Thus, each round-trip of light circulation in a microring is equivalent to light propagation along the coupled waveguide array of length L, which can be divided into a sequence of 4 coupling steps of equal length $L/4$. Denoting the fields in microrings A, B, and C in unit cell (m,n) in the lattice as $\psi^A_{m,n}$, $\psi^B_{m,n}$ and $\psi^C_{m,n}$ respectively, we can write the equations for the evolution of light in the waveguide array along the direction of propagation (z-axis) over each period in terms of the coupled mode equations [18]

$$-i\frac{\partial \psi^A_{m,n}}{\partial z} = \beta \psi^A_{m,n} + k_a(1)\psi^B_{m,n} + k_a(2)\psi^C_{m,n} + k_a(3)\psi^B_{m-1,n} + k_a(4)\psi^C_{m,n-1} \tag{2.6}$$

$$-i\frac{\partial \psi^B_{m,n}}{\partial z} = \beta \psi^B_{m,n} + k_a(1)\psi^A_{m,n} + k_a(3)\psi^A_{m+1,n} \tag{2.7}$$

$$-i\frac{\partial \psi^C_{m,n}}{\partial z} = \beta \psi^C_{m,n} + k_a(2)\psi^A_{m,n} + k_a(4)\psi^A_{m,n+1} \tag{2.8}$$

where β is the propagation constant of the microring waveguide mode and $k_a(j)$ specifies the coupling between adjacent waveguides in step j of each evolution period, with $k_a(j) = 4\theta_a/L$ in step j and 0 otherwise. By making use of Bloch's boundary conditions $\psi_{m+1,n} = \psi_{m,n}e^{ik_x\Lambda}$, $\psi_{m,n+1} = \psi_{m,n}e^{ik_y\Lambda}$, where Λ is the lattice constant, for each field in the microrings, we can express the coupled mode equations in the form of a Schrodinger equation with z taking the role of t

$$-i\frac{\partial}{\partial z}|\psi(\mathbf{k},z)\rangle = [\beta I + H_{FB}(\mathbf{k},z)]|\psi(\mathbf{k},z)\rangle \tag{2.9}$$

where $|\psi\rangle = [\psi^A_{m,n}, \psi^B_{m,n}, \psi^C_{m,n}]^T$, $\mathbf{k} = (k_x, k_y)$ is the crystal momentum vector, and I is the 3×3 identity matrix. The Floquet-Bloch Hamiltonian H_{FB} consists of a sequence of 4 Hamiltonians $H(j)$ corresponding to coupling steps $j = \{1,2,3,4\}$, which have the explicit forms for $j = 1,3$

$$H(j) = \begin{pmatrix} 0 & k_a e^{-i\delta_{3j}k_x\Lambda} & 0 \\ k_a e^{i\delta_{3j}k_x\Lambda} & 0 & 0 \\ 0 & 0 & 0 \end{pmatrix} \tag{2.10}$$

and for $j = 2,4$

$$H(j) = \begin{pmatrix} 0 & 0 & k_a e^{-i\delta_{4j}k_y\Lambda} \\ 0 & 0 & 0 \\ k_a e^{i\delta_{4j}k_y\Lambda} & 0 & 0 \end{pmatrix} \tag{2.11}$$

to give

$$H_{FB}(\mathbf{k},z) = \sum_{j=1}^{4} H(j) \tag{2.12}$$

In the above expressions, $\delta_{ij} = 1$ if $i = j$ and 0 otherwise. The Floquet-Bloch Hamiltonian is periodic in z with a periodicity equal to the microring circumference L, $H_{FB}(\mathbf{k}, z) = H_{FB}(\mathbf{k}, z+L)$.

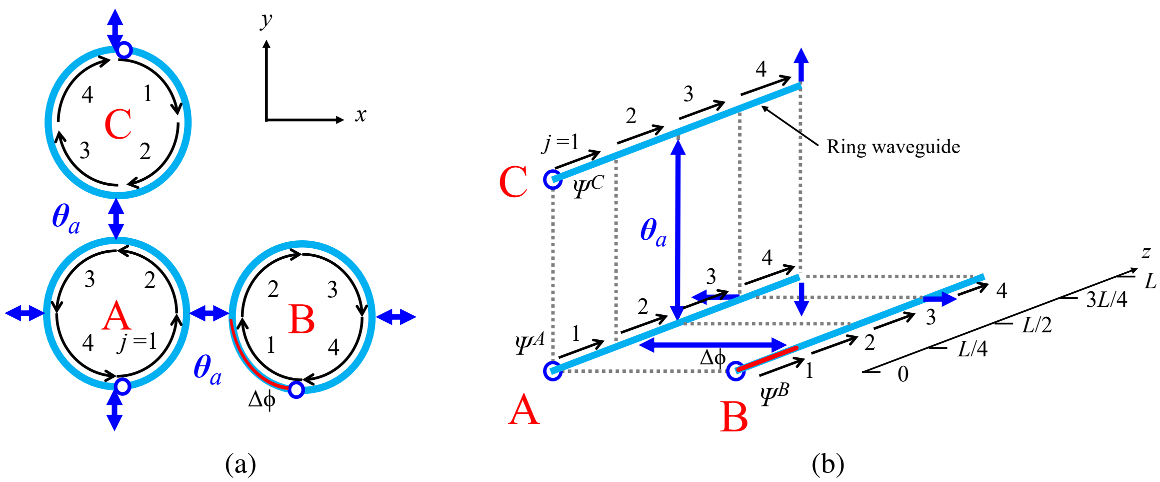

Figure 2.2: (a) Schematic of a unit cell of the 2D Floquet microring lattice with three microrings and neighbor coupling angle θ_a. Each round-trip of light propagation in a microring is broken into 4 steps, $j = 1$ to 4. Also shown is a periodic perturbation in the form of a phase detune $\Delta\phi$ (red) applied to step "$j = 1$" of microring B. (b) Equivalent coupled waveguide array of each unit cell in the microring lattice. The field propagation is along the microring waveguides ("z"-axis) with each period equal to the microring circumference L. Waveguide B experiences a periodic phase detune of $\Delta\phi$ (red) in step "$j = 1$". Adapted from the Supplementary Material of [77].

The solution of the Schrodinger equation in Equation 2.9 can be expressed as

$$|\psi(\mathbf{k}, z)\rangle = U(\mathbf{k}, z)e^{i\beta z}|\psi(\mathbf{k}, 0)\rangle \tag{2.13}$$

where $U(\mathbf{k}, z)$, the evolution operator, is given by

$$U(\mathbf{k}, z) = \mathcal{T}e^{i\int_0^z H_{FB}(k,z')dz'} \tag{2.14}$$

with the $\mathcal{T}$ being the time-order operator defined as,

$$\mathcal{T}e^{i\int H(z')dz'} = \lim_{\delta z \to 0} e^{iH(z)\delta z}e^{iH(z-\delta z)\delta z}e^{iH(z-2\delta z)\delta z}\ldots e^{iH(0)\delta z} \tag{2.15}$$

The Hamiltonian $H(j)$ in Equation 2.12 is independent of z in each step, allowing us to express the evolution operator (after dropping the $e^{i\beta z}$ term) as

$$U(\mathbf{k},z) = \left\{ \begin{array}{rl} e^{iH_1(\mathbf{k})z}, & 0 \leq z < L/4 \\ e^{iH_2(\mathbf{k})(z-L/4)}e^{iH_1(\mathbf{k})L/4}, & L/4 \leq z < L/2 \\ e^{iH_3(\mathbf{k})(z-L/2)}e^{iH_2(\mathbf{k})L/4}e^{iH_1(\mathbf{k})L/4}, & L/2 \leq z < 3L/4 \\ e^{iH_4(\mathbf{k})(z-3L/4)}e^{iH_3(\mathbf{k})L/4}e^{iH_2(\mathbf{k})L/4}e^{iH_1(\mathbf{k})L/4}, & 3L/4 \leq z \leq L \end{array} \right. \quad (2.16)$$

We can define an operator which samples the periodic evolution of the system at regular intervals, capturing the motion of the system every period, called the Floquet operator. This Floquet operator is then

$$U_F(\mathbf{k}) = U(\mathbf{k},L) = e^{iH_4(\mathbf{k})(L/4)}e^{iH_3(\mathbf{k})L/4}e^{iH_2(\mathbf{k})L/4}e^{iH_1(\mathbf{k})L/4} = e^{iH_{eff}(\mathbf{k})L} \quad (2.17)$$

where H_{eff} is the effective Hamiltonian. The Floquet operator is a unitary matrix with complex eigenvalues of unit magnitude. Its eigenstates $|\Phi_n(\mathbf{k})\rangle$ obtained from

$$U_F(\mathbf{k})|\Phi_n(\mathbf{k})\rangle = e^{i\varepsilon_n(\mathbf{k})L}|\Phi_n(\mathbf{k})\rangle \quad (2.18)$$

are called the Floquet modes with eigenvalues $e^{i\varepsilon_n(\mathbf{k})L}$. The quasienergy bands of the Floquet modes are given by $\varepsilon_n(\mathbf{k})$, which are periodic with a periodicity of $2\pi/L$. For each quasienergy band n, we can compute the Chern number from the Floquet state Φ_n as

$$C_n = C[P_n] = \frac{1}{2\pi i}\int_{BZ} Tr\{P_n[\partial_{k_x}P_n, \partial_{k_y}P_n]\}dk_x dk_y \quad (2.19)$$

where $[.,.]$ is the commutator and $P_n(\mathbf{k}) = |\Phi_n(\mathbf{k})\rangle\langle\Phi_n(\mathbf{k})|$ is the projector onto eigenstate $|\Phi_n(\mathbf{k})\rangle$ of the Floquet operator. Again, the winding number $w[U_\xi]$ can be calculated using Equation 2.3 and the definition for $U(\mathbf{k},z)$ given by Equation 2.14, choosing the appropriate eigenvalues $e^{i\varepsilon_n(\mathbf{k})L}$. For our microring lattice, the quasienergy spectrum consists of three bands with three bandgaps in each Floquet-Brillouin zone period ($0 \leq \varepsilon L \leq 2\pi$), with a flat band state at quasienergies $2m\pi$, $(m \in \mathbb{Z})$. We label the bandgaps I, II and III, as shown in Fig. 2.1b, where bandgaps I and III are symmetric with respect to $\varepsilon L = \pi$. The existence of edge states across all three of these bandgaps confirms the nontrivial, topological nature of the AFI lattice.

2.2 Floquet Defect Mode Resonance

The FDMR is created by introducing a periodic perturbation to the Hamiltonian in the form of a phase detune of a microring during a step j in each evolution period. Thus, if a phase detune of $\Delta\phi$ is applied to microring B in unit cell (m,n) during step j, as shown in Fig. 2.2, its equation of motion is modified as

$$-i\frac{\partial \psi^B_{m,n}}{\partial z} = (\beta + \Delta\beta(j))\psi^B_{m,n} + k_a(1)\psi^A_{m,n} + k_a(3)\psi^A_{m+1,n} \tag{2.20}$$

where $\Delta\beta(j) = 4\Delta\phi/L$ in step j and zero otherwise. The phase detune $\Delta\phi$ serves to break degeneracy and move one Floquet mode into the bandgap, forming an isolated band which is periodic in frequency. Figure 2.1b presents these isolated flat bands as colourful horizontal lines whose quasienergy is a function of phase detune applied. The spatial field localization pattern of the defect mode depends on which segments of the microring are detuned and where in the lattice the defect ring is located [76]. Figure 2.3a shows the hopping pattern for a phase detune applied to a microring B located along the bottom lattice boundary and Fig. 2.3b depicts when the detune is applied to a microring B in the bulk.

The spatial localization pattern of the FDMR can be understood as follows. In the limit of perfect coupling, $\theta_a \equiv \pi/2$, the hopping sequence guarantees that light starting in microring A in the bulk will return to the same microring after 3 periods, following a loop pattern. The bulk passbands consist of the $3L$ resonance bulk loops, as this forms the dominant hopping sequence. Figure 2.3 displays the spatial localization of one of these bulk modes. If we excite in the bandgap, the loop modes will be excited, but will not support constructive interference and will therefore die off as the round-trip phase is not a multiple of 2π. If we excite in the bulk passband, every unit cell participates in a 3L resonance loop at that passband frequency, supporting sporadic transmission through the bulk. By adding the phase detune to one bulk mode resonance and shifting its quasienergy into the bandgap, that one loop will support constructive interference and the neighbouring bulk loops will not, so the mode will stay localized. Allowing this loop to share a ring with the

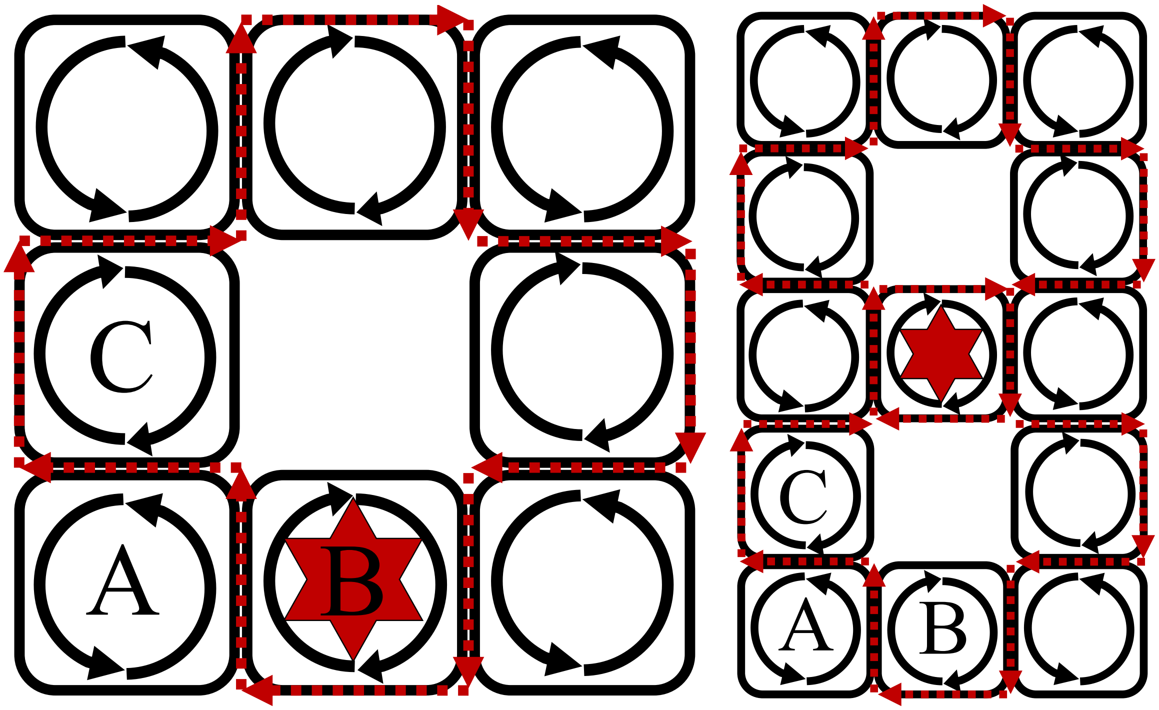

(a) (b)

Figure 2.3: $3L$ hopping loop spatial localization where (a) shows the FDMR when the defect ring (red star) is located along the edge of the lattice and (b) shows the dual-loop FDMR when the defect ring (red star) is located in the bulk.

edge mode allows for coupling between the edge mode and this detuned bulk mode. The FDMR is fundamentally distinct from the conventional defect-mode resonance in a static system as it is applied to the Floquet mode periodically in step j and no other time. The fact that different, distinct hopping modes can be excited through detune in different steps j demonstrates this difference. Additionally, unlike a conventional point-defect, the FDMR is localized to many unit cells, instead of only the unit cell containing the defect. Another defining feature of the FDMR is that it is cavity-less, requiring no physical boundaries to contain the resonance. This allows the resonance to be excited anywhere in the bulk of the lattice, provided appropriate phase detune is applied.

In practice, the phase detune is implemented through a refractive index change in some section of the resonator. This can be accomplished through thermo-optic tuning with current running through a metallic heater structure above the waveguide, or through free-carrier dispersion with bias voltage applied to a pn-junction integrated into the resonator waveguide. In the thermo-optic case, temperature changes on an SOI device can exceed 100°C. The change in temperature increases the effective index of the waveguide mode, effectively increasing the roundtrip phase around a single microring resonator. The loop bulk-mode forms a resonance that allows the Floquet mode to constructively interfere with itself, leading to strong field localization as pictured in Fig. 2.3. This resonance field enhancement can be leveraged similar to any resonance effect for various applications, with the added advantage that it allows us to exploit the topological protection properties of the Floquet insulator to realize devices whose performance is robust to lattice-level defects.

Chapter 3

Realization of Anomalous Floquet Insulators in Strongly Coupled Nanophotonic Lattices

Our group experimentally demonstrated the first anomalous Floquet insulator (AFI) on a nanophotonic platform using a square lattice of coupled octagon resonators [60, 78]. My contribution to this work was in the design and simulation of the unit cell, which consisted of 4 identical octagons with identical resonant frequencies but with alternating coupling coefficients to adjacent resonators. Unlike previously reported topological insulator systems based on microring lattices with static (time independent) Hamiltonians, the nontrivial topological behaviours of our system arose directly from the periodic evolution of light around each octagon, emulating a periodically-driven system. By exploiting asynchronism in the evanescent coupling between adjacent octagonal resonators, we could achieve strong and asymmetric couplings in each unit cell, which are necessary for observing AFI behaviour. Direct imaging of scattered light from fabricated samples confirmed the existence of chiral edge states as predicted by the topological phase map of the lattice. In addition, by exploiting the frequency dispersion of the coupling coefficients, we could observe topological phase changes of the lattice from normal insulator (NI) to Chern insulator (CI) and AFI. Our lattice thus provided a versatile nanophotonic system for investigating 2D Floquet topological photonic insulators (TPIs) and formed the basis for realizing AFI and FDMR in our research.

3.1 Introduction

In this Chapter, we report the first experimental realization of AFI on a nanophotonics platform using a lattice of strongly-coupled octagonal resonators in the silicon-on-insulator (SOI) material system. Our system exploits the periodic evolution of light around each microring to emulate a periodically-varying Hamiltonian [50]. We note that our Floquet TPI lattice is fundamentally different from the microring lattice recently reported in [31, 32]. In these works, static Chern insulators were realized by emulating a local gauge flux through a combination of direction-dependent nearest and next-nearest neighour hopping via link rings between site resonators. Since next-nearest neighbour couplings are usually weak, it is difficult to realize AFI behaviours in these lattices, which require strong coupling to observe. In our lattice, we exploit asynchronism in the evanescent coupling between neighbour octagons to achieve strong and asymmetric direct couplings in each unit cell, which allows us to observe AFI topological effects. Direct imaging of the scattered light pattern shows clear evidence of the formation of chiral AFI edge modes in the bulk bandgaps, which confirms the nontrivial topological behaviours of these lattices. In addition, by varying the coupling coefficients between the resonators, we could observe topological phase changes in the lattice and verify the existence of both Floquet and Chern insulators in different regions of the topological phase map. Our work thus introduces a new, versatile integrated optics platform for investigating Floquet topological behaviours in strongly-coupled 2D systems.

3.2 Theoretical Background

The majority of the theory supporting this lattice is covered in Chapter 2 as this lattice forms the basis for our AFI and FDMR development. We highlight that our lattice differs from the microring lattice in [32] as they require off-resonant link rings for coupling between adjacent resonators to emulate a single-spin system, whereas our lattice is much more compact and allows for the natural spin flipping which occurs between direct-coupled microrings. A depiction of our square lattice and 4-ring unit cell is provided in Fig. 3.1a. Figure 3.1b shows the topological phase map of square microring lattices, where the behaviours of bandgaps I (III) and II can be described as functions of the coupling angles θ_a and θ_b. In particular, AFI behaviour can be observed when $\theta_a = 0.473\pi$ and $\theta_b = 0.026\pi$ (marked by a red triangle labelled 'Z'). The band diagram of a microring lattice with these coupling coefficients, 10 unit cells in the y direction, and infinite unit cells in the x direction is shown in Fig. 3.1c. Here, bandgaps I, II, and III are identified as AFI bandgaps, 2 edge-modes cross each topologically non-trivial bandgap, and bandgaps I and III are symmetric about $\varepsilon L = \pi$.

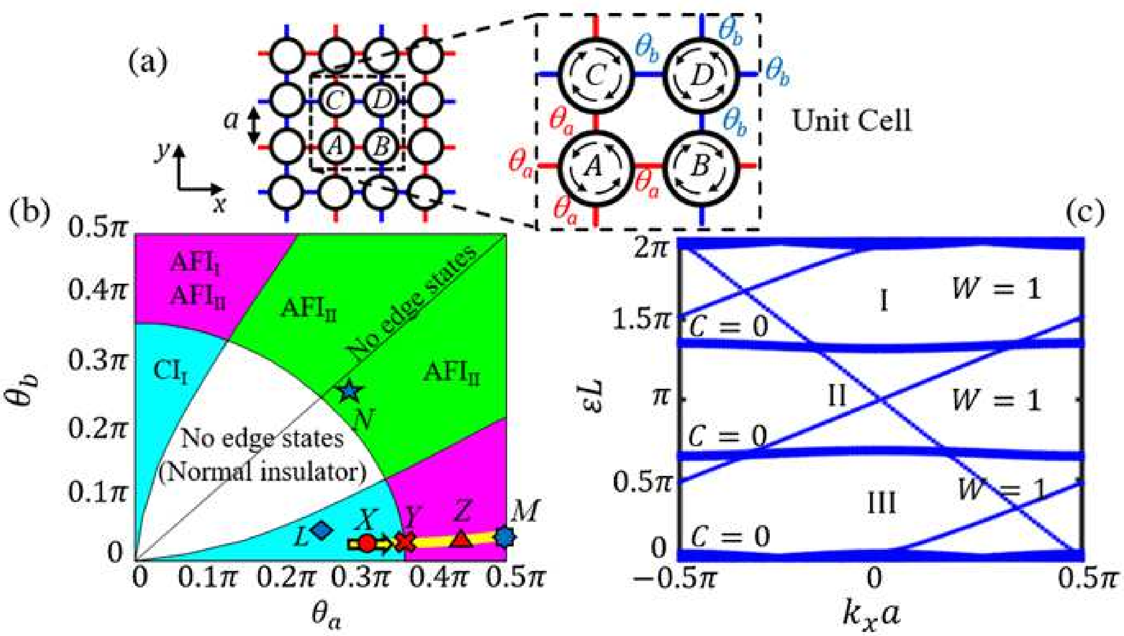

Figure 3.1: (a) Schematic of a Floquet TPI microring lattice and (b) its topological phase map [50]. The lattice behaves as a normal insulator except in regions marked by CI_N or AFI_N, which denote CI or AFI behavior in band gap $N = \{I, II\}$. Markers X, Y, and Z correspond to the topological phases of the fabricated lattice at three wavelengths in Fig. 3.5; L, M, N indicate additional fabricated lattices with different coupling coefficients. (c) AFI edge states in the projected quasienergy band diagram of a semi-infinite lattice with boundaries along the x direction and coupling angles $\theta_a = 0.473\pi$, $\theta_b = 0.026\pi$. The Chern number (C) of each energy band and winding number (W) of each bulk band gap are also indicated. Adapted from [60].

3.3 Experimental Realization

We realized Floquet TPI microring lattices on an SOI substrate with a 220 nm - thick silicon waveguide layer and a 2 μm - thick SiO_2 buried oxide layer. The silicon waveguides were cladded with a 2.2 μm - thick SiO_2 layer. For a square lattice of identical resonators, the microrings must be identical and evanescently coupled to their neighbours via identical coupling gaps. To enable unequal evanescent coupling strengths for resonators A and D in each unit cell, while preserving the square lattice geometry, we used octagonal resonators with sides of identical lengths but alternating widths, W_1 and W_2. Different coupling strengths between adjacent octagons can be achieved by exploiting the difference between synchronous coupling between two waveguides with identical width, and asynchronous coupling between waveguides with different widths. In the lattice, resonators A, B, and C are oriented in the same way, such that the coupling between A and its neighbours, B and C, occurs synchronously between waveguides of the same width, W_1. By rotating resonator D by 45°with respect to the other three resonators, we could obtain different coupling strengths between microring D and its neighbours, B and C, due to asynchronous coupling between waveguides of differing widths. A schematic of this 4-octagon unit cell is shown in Fig. 3.2a. In our design, the octagons have sides of length $L_s = 16.06$ μ m, with the corners rounded using 5 μm radius arcs to reduce scattering loss. The octagon waveguide has alternating widths of $W_1 = 400$ nm and $W_2 = 600$ nm, which support the fundamental TE mode around the 1600 nm telecommunication wavelength. The coupling gap between adjacent octagons is fixed at $g = 225$ nm. SEM images of the resonator waveguides and coupling gaps are presented in Fig. 3.2c, demonstrating the synchronous and asynchronous coupling junctions. At 1620 nm, this yields $\theta_a = 0.473\pi$ for synchronous coupling and $\theta_b = 0.026\pi$ for asynchronous coupling, as obtained from numerical simulations (Finite-Difference Time-Domain solver Lumerical [79]). The fabricated lattice consisted of 5x10 unit cells, with an input waveguide coupled to resonator A of a unit cell on the left boundary of the lattice for edge mode excitation, and an output waveguide coupled to resonator B of a unit cell on the right boundary for transmission measurements. An optical micrograph of the lattice is shown in Fig. 3.2b. The coupling angles between the input/output waveguides and the octagon resonators on the lattice boundary were also set to θ_a.

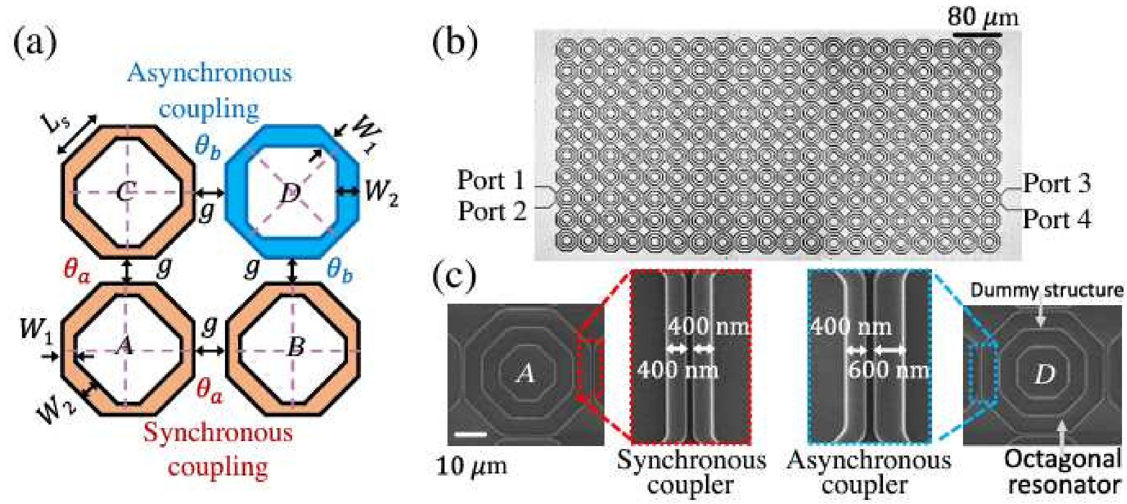

Figure 3.2: (a) Schematic of a unit cell of a Floquet lattice of identical, evanescently coupled octagon resonators, with octagon D rotated by 45° with respect to the other three resonators. (b) Optical microscope image of a 5×10 fabricated lattice with input and output waveguides coupled to the left and right boundaries. (c) SEM images of octagon resonators A and D with zoomed-in images of the synchronous and asynchronous coupling sections. Adapted from [60].

We characterized the transmission bands of the microring lattice by coupling TE-polarized light to the input waveguide and measuring the transmitted power in the output waveguide. A tunable semiconductor laser (Santec TSL 510), whose specifications are laid out in Table 3.1, was used to generated a continuous wave signal to probe the transmission spectrum of the lattice. A fiber polarization controller, Thorlabs FPC562, was used to manually ensure the input light was TE-polarized. The light was butt-coupled onto the SOI chip using an OZ Optics lensed fiber (TSMJ-3A-1550-9/125-0.25-7-2.5-14-2-AR). Transmitted light was then butt-coupled off the chip using an identical lensed fiber, where the optical power was then measured by a Newport power meter (Model 2936-C), whose specifications are laid out in Table 3.2.

The measured transmission spectrum of the lattice is shown in Fig. 3.3a. Over one FSR

Characteristic	Value	Unit
Wavelength Tuning Range	1510-1630	nm
Wavelength Resolution	5	pm
Absolute Wavelength Accuracy	±100	pm
Wavelength Repeatability	±10	pm
Wavelength Stability	≤±5	pm
Peak Output Power	≥+13	dBm
Power Repeatability	±0.01	dB
Power Stability	±0.01	dB
Power Flatness vs. Wavelength	±0.2	dB
Linewidth	500	kHz
Optical Output Connector	FC/APC	
Optical Fiber	SMF	
Communication	GP-IB	
Operating Temperature	15-35	°C

Table 3.1: Santec tunable semiconductor laser TSL-510 Type A performance characteristics. [80]

of the microring resonators (∼5 nm), we identified three bulk bandgaps (I, II, and III) separating the passbands. The high power transmission in all three bulk bandgaps indicates that edge modes were excited in these frequency ranges. We conclude that these modes must correspond to the AFI edge states which exist in all three bandgaps of the microring lattice, as predicted by the projected band diagram computed for the lattice. On the other hand, the transmission spectrum in the bulk passbands exhibits multiple dips, which are caused by multiple interference and localized resonances of light propagating through the bulk of the lattice. For comparison, the simulated transmission spectrum of the lattice was computed using the field coupling method in [18]. The coupling angles were set at $\theta_a = 0.473\pi$ and $\theta_b = 0.026\pi$. A propagation loss of 3 dB/cm was assumed in each octagon resonator. The effects of ±5% uniformly-distributed random variations in the coupling strengths and

Characteristic	Value	Unit
Wavelength Tuning Range	1510-1630	nm
Wavelength Resolution	5	pm
Absolute Wavelength Accuracy	±100	pm
Wavelength Repeatability	±10	pm
Wavelength Stability	$\leq$±5	pm
Peak Output Power	$\geq$+13	dBm
Power Repeatability	±0.01	dB
Power Stability	±0.01	dB
Power Flatness vs. Wavelength	±0.2	dB
Linewidth	500	kHz
Optical Output Connector	FC/APC	
Optical Fiber	SMF	
Communication	GP-IB	
Operating Temperature	15-35	°C

Table 3.2: Newport power meter (Model 2936-C) performance characteristics. [81]

round-trip phases in the lattice was also investigated and compared to our experimental results. The simulated transmission spectrum, including consideration of variation in coupling strength and round-trip phase, is presented in Fig. 3.3b. The characteristic flat band and high transmission in the bulk bandgaps due to edge modes were clearly visible, in good agreement with the measured spectrum. The bulk passbands also exhibit transmission dips similar to those observed in the measured spectrum.

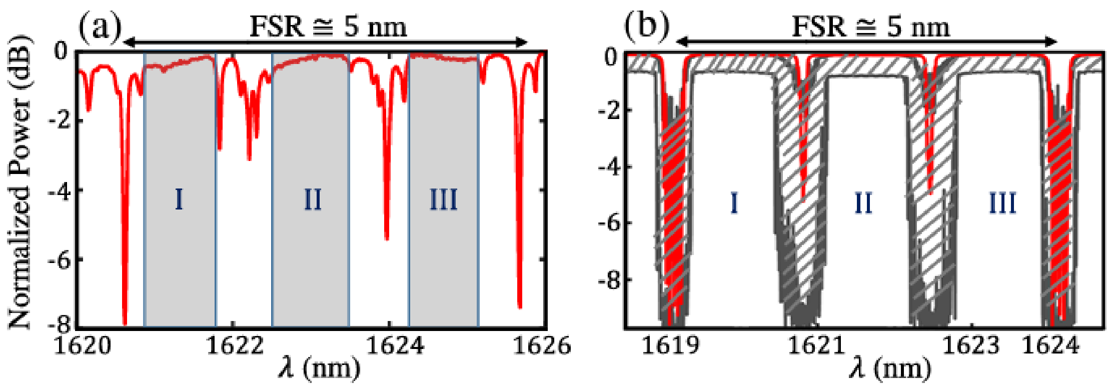

Figure 3.3: (a) Measured and (b) simulated transmission spectra of the TPI microring lattice. The red line in (b) is the spectrum obtained for an ideal lattice of identical microrings with coupling angles $\theta_a = 0.473\pi$, $\theta_b = 0.026\pi$. The hatched area indicates the range of transmission values obtained in the presence of 5% random variations in the coupling strengths and microring round-trip phases. Adapted from [60].

To obtain direct proof of AFI edge modes in the bulk bandgaps, we excited the lattice by injecting light at 1623 nm wavelength, which lies in bandgap II, into the input waveguide. Input light was coupled onto the chip similarly to the transmission spectrum measurements. A microscope was setup vertically above the lattice and an NIR camera (Sensors Unlimited 320M-1.7RT), whose specifications are laid out in Table 3.3, was used to record the light scattered from the lattice. The imaged scattered light intensity distribution could be seen over the lattice when light was injected into Port 1 of the input waveguide, as shown in Fig. 3.4a. Clear evidence of light propagating along the bottom edge of the lattice could be seen, indicating that an AFI edge mode was formed. The simulated light intensity distribution in the microrings also showed good agreement with the scattered light intensity map obtained from the camera. When light was injected into Port 2 of the input waveguide, a counter-propagating edge mode was excited, which propagated along the top edge of the lattice, as seen in Fig. 3.4b. The two chiral modes represent two orthogonal pseudospin states of the lattice which are time-reversal (TR) counterparts of each other, since they have identical quasienergy but propagate in opposite directions in each microring. However, since the driving sequence of our lattice does not satisfy the condition for TR invariance [48, 82], the two chiral edge modes are not TR symmetric, as evidenced by the asymmetry in their dispersion behaviours about $k_x = 0$. The difference in the field distributions provides further evidence of the asymmetry of these modes, reflecting the fact that the boundaries seen by the 2 chiral modes are not the same. The chiral nature of the edge modes implies that time reversal symmetry is broken between the two pseudo-spin states, which exist separately in each microring of the lattice. We also observed similar AFI edge mode patterns for excitation wavelengths in bandgaps I and III. By contrast, when we tuned the laser wavelength to 1624 nm, which lies in a bulk passband, only bulk modes were excited and no edge mode was observed. This can be seen from the NIR camera image in Fig. 3.4c, which showed that the input light spread out over the lattice, instead of remaining localized along the edge. The simulated light intensity distribution in the lattice at the corresponding wavelength also confirmed this behaviour.

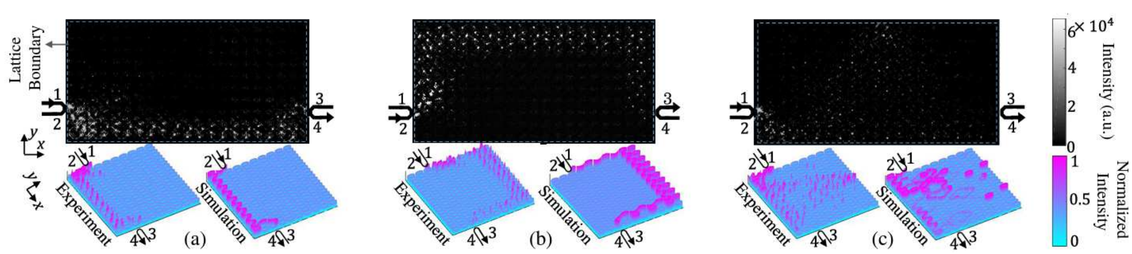

Figure 3.4: (a),(b) NIR camera images showing chiral AFI edge modes along the bottom edge and top edge, respectively, of the octagon lattice when light in a bulk band gap ($\lambda = 1623$ nm) was injected into port 1 or port 2 of the input waveguide. The lower left plot in each figure shows the map of scattered light intensity constructed from raw camera data; the lower right plot is the simulated light intensity distribution in the lattice. (c) When input light was tuned to a wavelength in a transmission band ($\lambda = 1624$ nm), only bulk modes were excited and no edge mode is observed. Adapted from [60].

Since the topological behaviours of the microring lattice depend on the coupling an-

Characteristic	Value	Unit
Spectral Range	900 - 1700	nm
Quantum Efficiency	>70	%
Mean Detectivity, D	>2x10^{12}	cm$\sqrt{Hz}\sqrt{W}$
Noise Equivalent Irradiance	<5x10^{9}	photons/cm$^2\cdot$s
Noise (RMS)	<1000	electrons
Exposure Times	0.127 - 16.27	ms
Frame Rate	60	Hz

Table 3.3: Sensors Unlimited Inc. SU320M-1.7RT InGaAs NIR MiniCamera performance characteristics. [83]

gles θ_a and θ_b, we can observe topological phase changes in the lattice by exploiting the frequency dispersion of the evanescent couplers. The simulated coupling angles for the synchronous and asynchronous couplers of the octagon resonators were calculated over the wavelength range of 1500 - 1630 nm. The corresponding topological phase of the lattice follows a path across the topological phase map, depicted by the yellow line across Fig. 3.1b, where bandgaps I and III change from CIs to AFIs and bandgap II changes from NI to AFI as θ_a increases and θ_b remains relatively constant. The projected band diagrams of semi-infinite lattices were calculated at three progressive wavelengths along this path, marked as X, Y, and Z in Fig. 3.1b. The band diagrams shown in Figs. 3.5a-c illustrate the change in bandgap characterization as the wavelength, and thus θ_a, is increased.

To observe these topological phase changes, we measured the transmission spectra of the microring lattice around these wavelengths, shown in Figs. 3.5d-f. Close correspondence between the measured transmission spectra and the projected band diagrams could be seen for all three cases. In particular, high transmission is observed in wavelength ranges corresponding to topologically non-trivial bulk bandgaps where CI or AFI edge modes are expected. Within one FSR of the microring resonators, the two shorter wavelength spectra demonstrated only two bulk bandgaps with edge modes (I and III), while the longer wavelength spectrum has three distinct bulk bandgaps with edge modes, as predicted by the projected band diagrams. At the shortest wavelength, the transmission in the center bulk bandgap (II) is low, since the lattice behaves as a NI and thus no edge mode exists, instead the lattice is completely isolating to the flow of light. The spatial distribution of the light intensity at various wavelengths also followed the expected behaviours for the appropriate types of bandgaps, as shown in Figs. 3.5g-i.

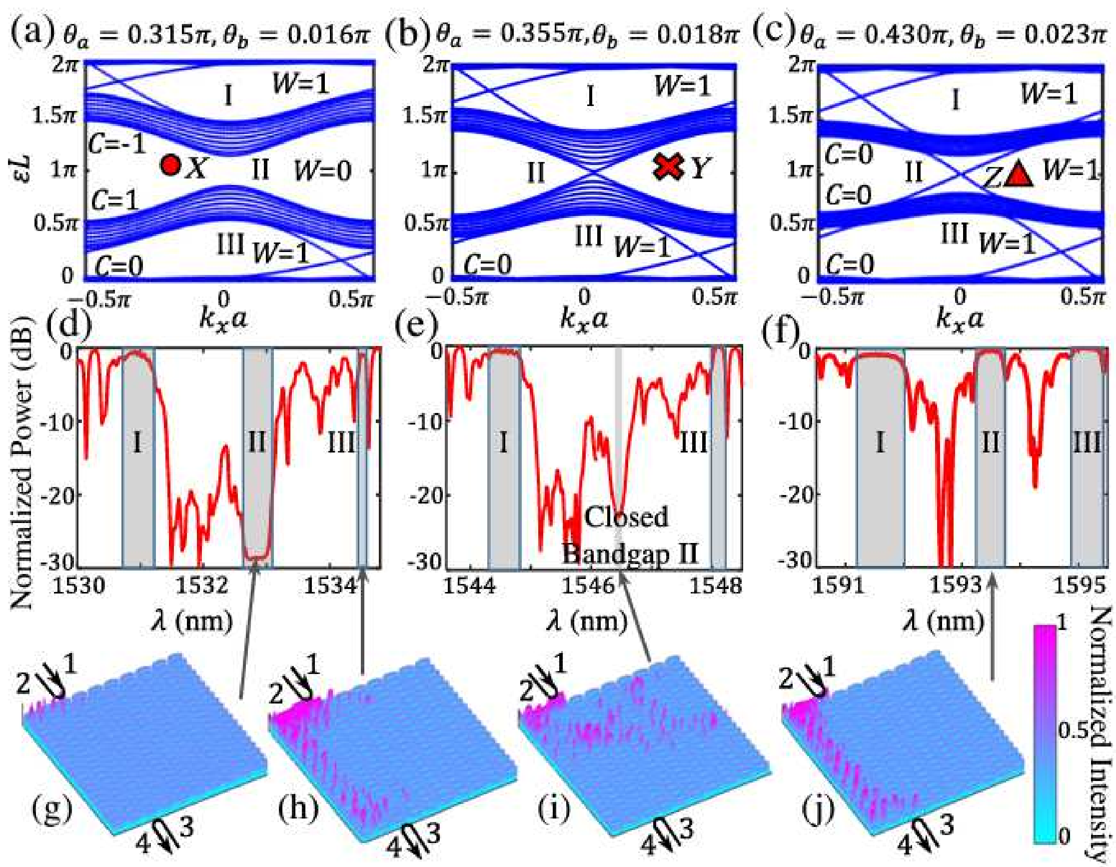

Figure 3.5: Topological phase changes in the octagon lattice due to frequency dispersion in the coupling angles: (a)–(c) Projected band diagrams of a semi-infinite lattice with boundaries along x around (a) $\lambda_X = 1532.5$ nm, (b) $\lambda_Y = 1546.5$ nm, (c) $\lambda_Z = 1593.5$ nm. (d)–(f) Measured transmission spectra of the lattice over one FSR centered around λ_X, λ_Y, and λ_Z. (g)–(j) Scattered light intensity distributions obtained from NIR camera showing different topological behaviors at various input wavelengths: (g) normal insulator located in topologically trivial bulk band gap II, (h) CI edge mode in bulk band gap III, (i) bulk modes in closed band gap II, (j) AFI edge mode in reopened bulk band gap II. Adapted from [60].

We also fabricated octagon lattices with different coupling gap, coupling length, and waveguide widths to verify the topological behaviours of the lattice in different regions of the phase map, marked by L, M, and N in Fig. 3.1b. The NIR images of these samples, provided in Figs. 3.6a-c, also showed edge modes formed in topologically nontrivial band gaps of these lattices as predicted by the phase map. These results also provided additional evidence that our Floquet microring lattice behaves as predicted.

Sample	L_s (μm)	W_1 (nm)	W_2 (nm)	g (nm)	θ_a (π)	θ_b (π)	λ (nm)	Edgemode
L	13.14	400	600	275	0.254	0.031	1627	CI (bandgap I)
M	16.06	400	600	200	0.5	0.027	1600	AFI (bandgap II)
N	16.06	400	610	225	0.307	0.277	1527	AFI (bandgap II)

Table 3.4: Design parameters of additional fabricated octagon TPI lattice samples. Adapted from the Supplemental Material of [60].

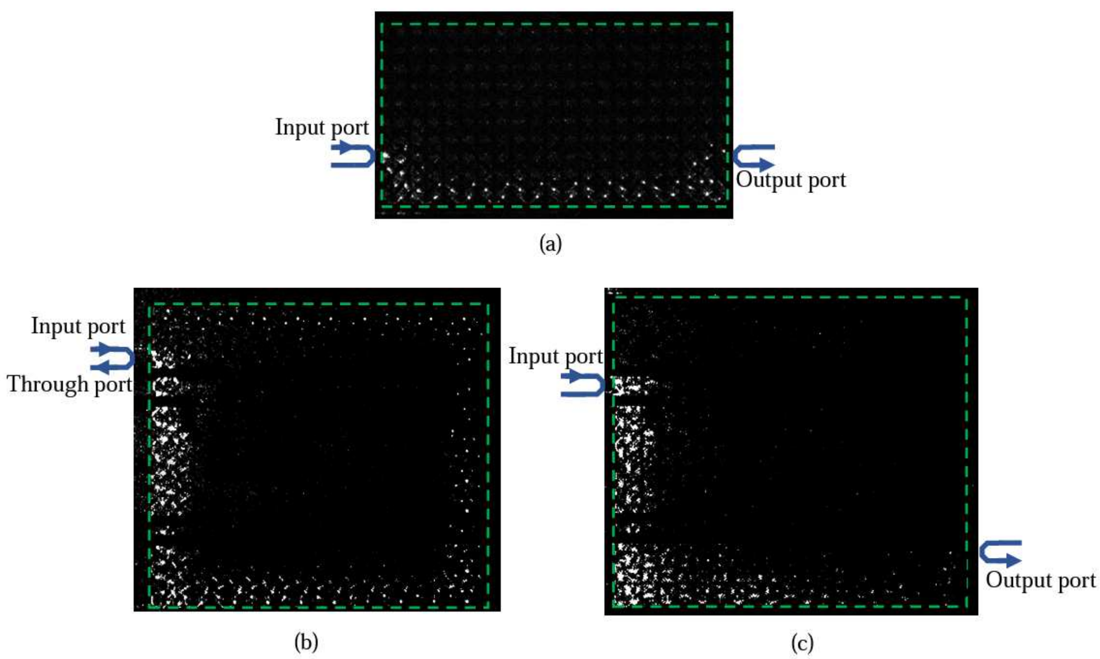

Figure 3.6: NIR images of scattered light distribution showing (a) CI edgemode in bandgap I of sample L, (b) AFI edgemode in bandgap II of sample M, and (c) AFI edgemode in bandgap II of sample N. Adapted from the Supplemental Material of [60].

3.4 Conclusions

In conclusion, we experimentally demonstrated a Floquet TPI based on a 2D lattice of strongly coupled octagonal resonators. The system emulates a periodically varying Hamiltonian through the periodic evolution of light around each octagon. By exploiting asynchronism in the evanescent coupling between waveguides of different widths, we realized strong and asymmetric direct couplings between adjacent resonators, which allowed us to observe chiral AFI edge modes. Our lattice also exhibited rich topological behaviours, including NI, CI, and AFI, through the tuning of the coupling angles. This work thus introduces a versatile nanophotonic platform for investigating Floquet TPIs and exploring their applications. [60]

Chapter 4

Broadband Resonance-Enhanced Frequency Generation by Four-Wave Mixing in a Silicon Floquet Topological Photonic Insulator

Floquet topological photonic insulators (TPIs), whose light transport properties are dictated by the periodic drive sequence of the lattice, provide more flexibility for controlling and trapping light than undriven topological insulators. This can enable novel nonlinear optics applications in topological photonics. In this Chapter, I employed Floquet defect mode resonance (FDMR) in a 2D silicon Floquet microring lattice to demonstrate resonance-enhanced frequency generation by stimulated four-wave mixing (FWM) using Floquet bulk modes in the presence of Kerr nonlinearity. The compact, cavity-less resonance mode, induced through a periodic perturbation of the lattice drive sequence, has the largest reported Q-factor for a 2D topological resonator of $\sim 10^5$ with low group velocity dispersion (GVD), which enables efficient broadband frequency generation over several Floquet-Brillouin zones of the Floquet topological insulator. I achieved wavelength conversion over a 10.1 nm spectral range with an average enhancement of 12.5 dB in the conversion efficiency due to the FDMR. This work could lead to robust light sources generated directly on a topologically-protected photonic platform.

4.1 Introduction

As covered in Chapter 1, Floquet topological insulators [39, 40] based on periodically-driven quantum systems can exhibit much richer topological behaviors than static systems, such as the existence of anomalous Floquet insulator (AFI) phase not observed in time-independent topological insulators. Here, we exploit the periodicity of the quasienergy of the FDMR and its low GVD in a 2D microring lattice to demonstrate resonance-enhanced stimulated FWM over several Floquet-Brillouin zones. While nonlinear self-phase modulation effects have been investigated for soliton propagation in a 2D Floquet TPI based on periodically-coupled waveguide arrays [57], our work represents the first investigation of parametric nonlinear interactions of Floquet bulk modes in a 2D topological resonator with Kerr nonlinearity, leading to enhanced broadband frequency generation on a Floquet topological platform.

Parametric processes based on third-order nonlinearity have important applications such as frequency generation and wavelength conversion. These processes have been demonstrated in various conventional integrated optics devices, such as FWM in silicon waveguides [84] and third-harmonic generation in chalcogenide photonic crystal waveguides [85]. As mentioned in Chapter 1, the emergence of nonlinear topological photonics has led to a growing interest in achieving these parametric processes on a TPI platform, which could exploit the topological protection of edge modes to realize robust wavelength sources and frequency converters [53, 55, 59, 66–69]. For example, one-dimensional arrays of silicon nanodisks emulating the generalized Su–Schrieffer–Heeger model have been used to obtain enhanced third-harmonic generation at telecom frequencies through Mie resonances and the topological localization of edge states [68]. Plasmonic metasurfaces consisting of 2D hexagonal arrays of nanoholes in graphene sheets under static magnetic fields have also been demonstrated to form Chern insulator edge states, which were used to achieve FWM in the 13 THz frequency range [69]. However, the conversion efficiencies (CEs) achieved in these works were fairly poor. Various methods for improving the CE of FWM have been demonstrated, including slow-light waveguides [86, 87], resonant field enhancement [88–91], and graphene-enhanced resonators [92–94].

In this Chapter, we exploit the high Q-factor and low dispersion of FDMRs in a silicon Floquet microring lattice to achieve efficient broadband wavelength conversion by stimulated FWM in Floquet bulk modes. A unique feature of the FDMR is that it is cavity-less, since its spatial localization pattern is defined not by any lattice boundaries or interfaces but instead by the hopping sequence of a Floquet bulk mode. The lack of physical interfaces enables the FDMR to have a very high Q-factor, with values as high as $\sim 10^5$ for our silicon structure. Combined with the low GVD of the Floquet bulk mode, we achieved broadband wavelength conversion over 10.1 nm (from signal to idler wave), with an average CE enhancement of 12.5 dB due to the resonance effect. This work could lead to efficient broadband and tunable wavelength conversion, parametric amplification and entangled photon pair generation directly on a topologically-protected photonic platform.

4.2 Theoretical Background

Four-wave mixing is the process in which a material with a 3rd-order nonlinearity χ^3 absorbs 2 photons and emits that energy in 2 photons. In general, these 4 photons can be of 4 different frequencies, hence four-waves are mixed. In the stimulated, non-degenerate case, $\omega_{p1} + \omega_{p2} = \omega_s + \omega_i$, all 4 frequencies are determined by the three input waves, generally referred to as the pump 1, pump 2, and signal waves. In this way, the frequency of the idler wave is determined by the input of the other 3 waves. In the stimulated, degenerate case, $\omega_p 1 \equiv \omega_p 2 = \omega_p$, and so there are only 2 input waves which serve as the pump and the signal. In this case, the determination of which input photons fulfill which role is arbitrary, and two idler waves, $\omega_{i1} = 2\omega_p - \omega_s, \omega_{i2} = 2\omega_s - \omega_p$ are produced. These two idler waves are found $\pm\Delta\omega$ from the input waves, where $\Delta\omega = |\omega_p - \omega_s|$ is the frequency difference between the input waves.

In order to achieve maximum CE enhancement due to resonance, the pump, signal and idler waves must be aligned with the cavity resonances, while simultaneously satisfying the phase matching condition $2\beta_p = \beta_s + \beta_i$, where β_p, β_s and β_i are the propagation constants of the pump, signal and idler, respectively, in the resonator. However, dispersion of the resonant modes causes a phase mismatch, defined as $\Delta\beta = 2\beta_p - \beta_s - \beta_i$, which increases with the separation between the signal and idler waves, causing a precipitous degradation in the CE [95]. For a fixed pump frequency ω_p, the phase mismatch can be estimated as $\Delta\beta \approx -\beta_2(\omega_p)\Delta\omega$, where $\beta_2 = d^2\beta/d\omega^2$ is the GVD and $\Delta\omega$ is the spectral separation between the signal and the pump. Thus, a requirement for achieving broadband wavelength conversion is that the resonance modes must have low GVD.

4.2.1 Floquet Defect Mode Resonance and Frequency Conversion

FDMR can be regarded as the Floquet counterpart of point-defect resonance in static lattices, except that here the resonance mode arises from a periodic perturbation applied to the drive sequence of the Floquet lattice [76]. The Floquet TPI design we consider here is a 2D square microring lattice which has been recently explored [50, 60], and described in Chapter 2, as shown in Fig. 4.1a. In the device fabricated for this FWM experiment, we remove microring D, effectively setting the coupling angle θ_b to 0, which also reduces coupling losses and propagation losses in the lattice, allowing high-Q and strongly-localized FDMRs to be realized for enhanced nonlinear interactions. The resulting lattice, also shown in Fig. 4.1a, is thus characterized by a single coupling angle θ_a between 3 resonators in each unit cell, and resembles a proposed AFI microring lattice [9].

The Floquet nature of the lattice arises from the periodic circulation of light in each microring, with the driving Hamiltonian dictating the sequence of couplings to neighbor resonators over one roundtrip, as described in Chapter 2. We also note that unlike a similar microring lattice used to realize Chern insulator behaviour [8], our lattice does not use off-resonance link rings as couplers between site resonators, but instead employs direct evanescent coupling between neighbor resonators. This allows stronger coupling with

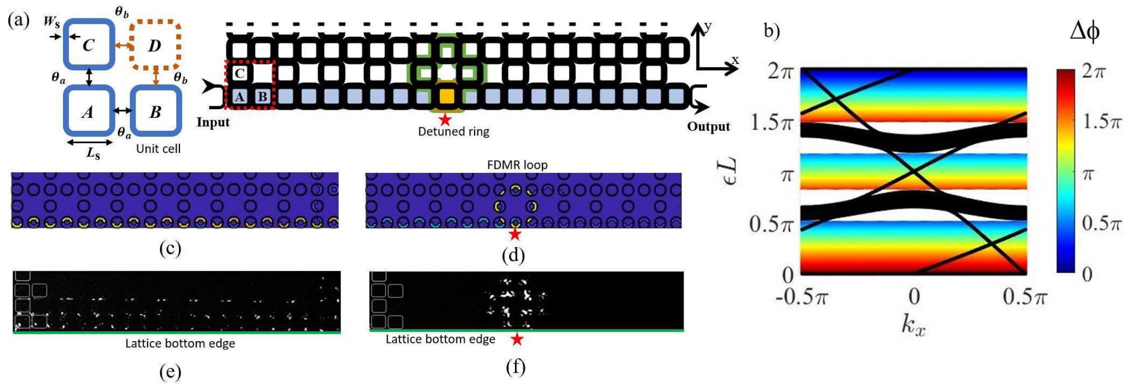

Figure 4.1: (a) Schematic of 2D Floquet microring lattice with each unit cell consisting of 3 identical microrings A, B, C with neighbor coupling angle θ_a. The 4th microring D is omitted, setting $\theta_b \equiv 0$. The FDMR loop, shown in green, is excited by applying a phase detune to 3/4 of the defect microring (indicated by red star). (b) Projected quasienergy band diagram of a Floquet lattice with $\theta_a = 0.441\pi$ showing all 3 bandgaps hosting AFI edge modes. The colored gradients depict FDMR quasienergy bands which move across the band gaps with increasing phase detune $\Delta\phi$ applied to the defect ring. (c) Simulated spatial distribution of an edge mode along the bottom lattice boundary at $\varepsilon = 1.7\pi/L$, and (d) the induced FDMR at the same quasienergy. (e) Near-infrared image of an edge mode and (f) induced FDMR at 1511.97 nm wavelength in the fabricated lattice. Details of the simulation results for (b)-(d) provided in the supplementary material.

lower dispersion to be achieved, so that our Floquet TPI exhibits nearly identical nontrivial band gaps over many Floquet-Brillouin zones, which is necessary for achieving broadband wavelength conversion by FWM.

We designed our microring lattice to have coupling angle $\theta_a = 0.441\pi$ so that it exhibits AFI behavior in all its three bandgaps over each Floquet-Brillouin zone [50]. Figure 4.1b shows the projected quasienergy band diagram, plotted as εL where ε is the quasienergy and L is the roundtrip length of the microrings, within one Floquet-Brillouin zone of a lattice with boundaries along the x-direction. Each Floquet-Brillouin zone also corresponds to one free spectral range (FSR) of the microrings. In Fig, 4.1b, the black lines trace the quasienergies of the transmission bands and edge modes crossing three topologically nontrivial band gaps. The simulated intensity distribution of the edge mode at quasienergy $\varepsilon = 1.7\pi/L$ (located in band gap III) is shown in Fig. 4.1c, which confirms light spatially localized along the bottom lattice boundary.

The FDMR is induced by applying a phase detune $\Delta\phi$ to the bottom three-quarters of a microring located on the bottom edge of the lattice (marked by a red star in Fig. 4.1a). This phase detune is applied through the thermo-optic effect. Heating current is applied to a resistive circuit fabricated above the target defect ring. Local temperature change of the SOI structure can exceed 100°C. This increase in temperature increases the effective refractive index of the waveguide mode, thus increasing the roundtrip phase of the light. The phase detune introduces a shift in the on-site potential of the defect resonator during three-quarters of each evolution period. This perturbation has the same periodicity of the driving sequence, since light experiences this phase detune each time it completes a roundtrip around the defect microring. The effect of the perturbation is to push a Floquet bulk mode from each transmission band into the band gap below, forming a flat-band state with a quasienergy shift proportional to the amount of phase detune. These flat bands are depicted by the horizontal color gradients in the band gaps in Fig. 4.1b. The simulated spatial intensity pattern of the FDMR at quasienergy $\varepsilon = 1.7\pi/L$ is shown in Fig. 4.1d, which shows light traveling in a loop pattern and constructively interfering with itself to form a strong resonance [76]. We note that this loop pattern is not due to light confinement by any physical lattice interfaces but follows the hopping sequence of a Floquet bulk mode in the microring lattice and extends far beyond the defect site resonator. Due to the periodic nature of the Floquet TPI, the FDMRs are also periodic in quasienergy, which allows resonance-enhanced FWM to be achieved over multiple Floquet-Brillouin zones.

4.3 Experimental Realization

We fabricated a Floquet microring lattice with 10×10 unit cells on an SOI substrate, an image of which is shown in Fig. 4.2. The microring waveguides were designed for the fundamental TE mode with 450 nm width and 220 nm height, lying on a 2 μm-thick SiO_2 substrate and covered by a 3 μm-thick SiO_2 cladding. Each microring was designed to have a square shape to allow for strong coupling between adjacent resonators, which is necessary

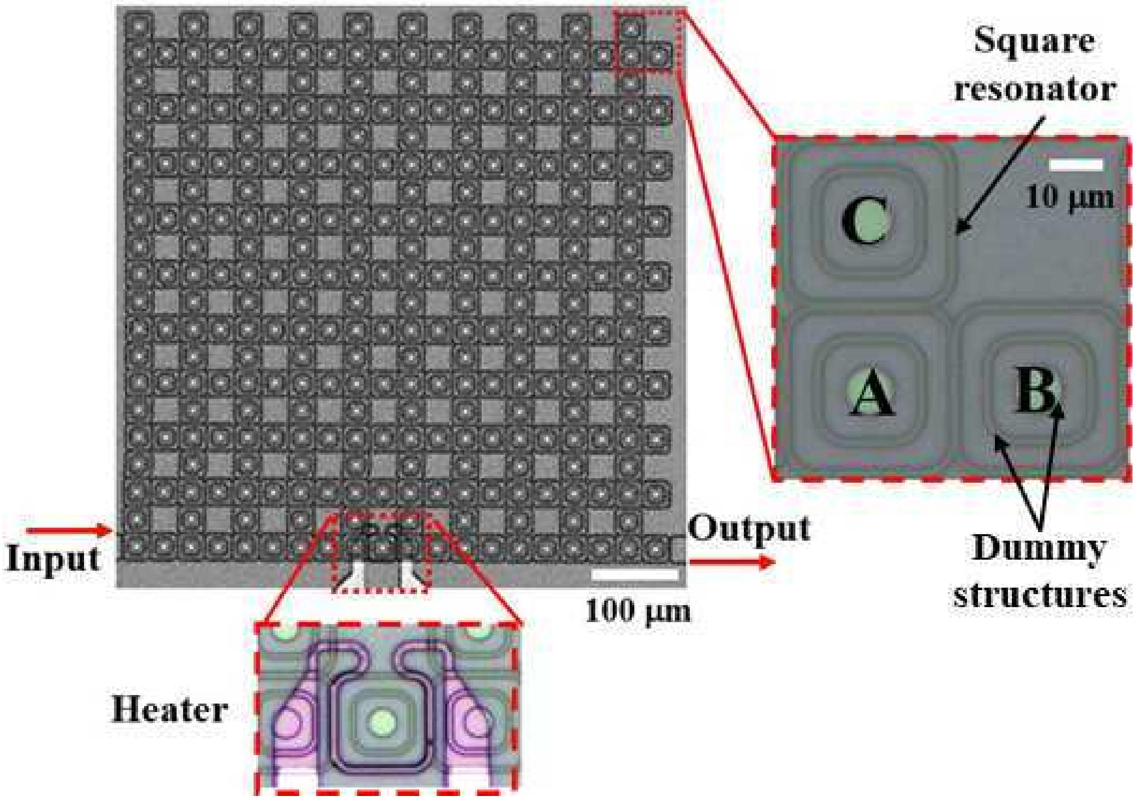

Figure 4.2: Microscope image of the 10×10 unit cell lattice with close-up images showing the metal heater on the defect microring and a unit cell. The dummy structures inside of the resonators achieve a uniform pattern density for more consistent fabrication results.

to realize the AFI phase. The side lengths of the square were 19.64 μm with coupling gap of 180 nm between neighbor resonators, which provides a large coupling angle θ_a with low dispersion. The corners of the square were rounded with 5 μm radius to reduce scattering loss. The overall circumference of each microring was chosen to provide sufficiently large FSR (∼5 nm) to observe distinct topological bandgaps. A close-up image of a single unit cell is provided in Fig. 4.2. Simulations showed that the coupling angle remained relatively constant across multiple microring FSRs, with values of 0.431π, 0.441π and 0.450π at the signal (1524.1 nm), pump (1529.1 nm), and idler (1534.2 nm) wavelengths, respectively, used to demonstrate FWM. The visible wavelength camera used to record these microscope images was an Edmund Optics EO-1312C (59-366) CMOS Color USB Camera, whose performance characteristics are summarized in Table 4.1.

To excite an edge mode along the bottom boundary of the lattice, an input waveguide

Characteristic	Value	Unit
Resolution	2048 x 1536	Pixels
Pixel Size	3.2	μm
Sensor Size	6.554 x 4.915	mm
Quantum Efficiency (Max)	34 (blue), 36 (green), 39 (red)	%
Pixel Clock	5 - 43	MHz
Frame Rate	11	FPS
Exposure Time	0.057 - 1744	ms
Spectral Range	400 - 750	nm

Table 4.1: Edmund Optics EO-1312C (59-366) CMOS Color USB Camera performance characteristics. [96]

was coupled to a microring at the bottom left corner and the transmitted light collected via an output waveguide coupled to a microring at the bottom right corner. A metallic heater with a resistance of $R \sim 300\ \Omega$ was used to apply a phase detune to three-quarters of a resonator on the bottom edge of the lattice via the thermo-optic effect, thereby generating an FDMR which is coupled to the AFI edge mode propagating along the bottom boundary.

We first measured the transmission spectrum of the AFI edge mode by sweeping the wavelength of an input TE-polarized laser source with 3 μW of on-chip power over several FSRs of the microrings and measuring the transmitted power at the output waveguide. We use a setup similar to that in Chapter 3 to measure the edge mode spectrum. A tunable semiconductor laser (Santec TSL 510), whose specifications are laid out in Table 3.1, was used to generated a continuous wave signal to probe the transmission spectrum of the lattice. A fiber polarization controller, Thorlabs FPC562, was used to manually ensure the input light was TE-polarized. The light was butt-coupled onto the SOI chip using an OZ Optics lensed fiber (TSMJ-3A-1550-9/125-0.25-7-2.5-14-2-AR). Transmitted light was then butt-coupled off the chip using an identical lensed fiber, where the optical power was then measured by a Newport power meter (Model 2936-C), whose specifications are laid out in Table 3.2. The result is presented by the red trace in Fig. 4.3a, which shows three distinct wavelength regions in each FSR with relatively high and flat transmission due to edge mode propagation. We identify these regions as the three topological band gaps of the lattice, as predicted by the projected band diagram in Fig. 4.1b. Figure 4.1e shows a near-infrared (NIR) image of the scattered light intensity of the lattice at 1511.97 nm wavelength, which confirms the presence of an edge mode in this band gap propagating along the bottom boundary. We next applied 17.8 mW of electrical power to the heater to induce a phase detune in the defect ring. The measured transmission spectrum at the output waveguide is presented by the blue trace in Fig. 4.3a, which is identical to the red trace except for the appearance of three sharp resonance dips. These dips correspond to an FDMR mode formed in band gap III of each microring FSR. We note that the FDMR mode in band gap I is not visible due to weak coupling to the edge mode, while band gap II is too narrow to support a well-localized resonance mode. Figure 4.1f shows the NIR image of the scattered light intensity taken at 1511.97 nm resonance wavelength with heating applied, which confirms the spatial localization of the resonance mode in a loop pattern. We note that the introduction of the FDMR does not alter the topological properties of the lattice, as evidenced by the high edge-mode transmission at off-resonant wavelengths in the band gaps. In our FWM experiment below, idler waves were generated at the FDMR resonance wavelengths and measured at the output waveguide, providing further evidence of topologically-protected edge modes propagating along the sample boundary after the FDMR was turned on.

Figure 4.3b shows the tuning of an FDMR across band gap III by varying the heater power from 13.9 mW to 21.2 mW. The linewidth of the resonance is also seen to vary across the band gap, which is due mainly to the dependence of the coupling between the edge mode and the FDMR loop on the roundtrip phase of the defect microring [76]. From the plot, we obtain the sharpest resonance dip near the mid gap at 17.8 mW heater power, yielding an FDMR with Q-factor of 72,600. As previously shown [76], the FDMR also ex-

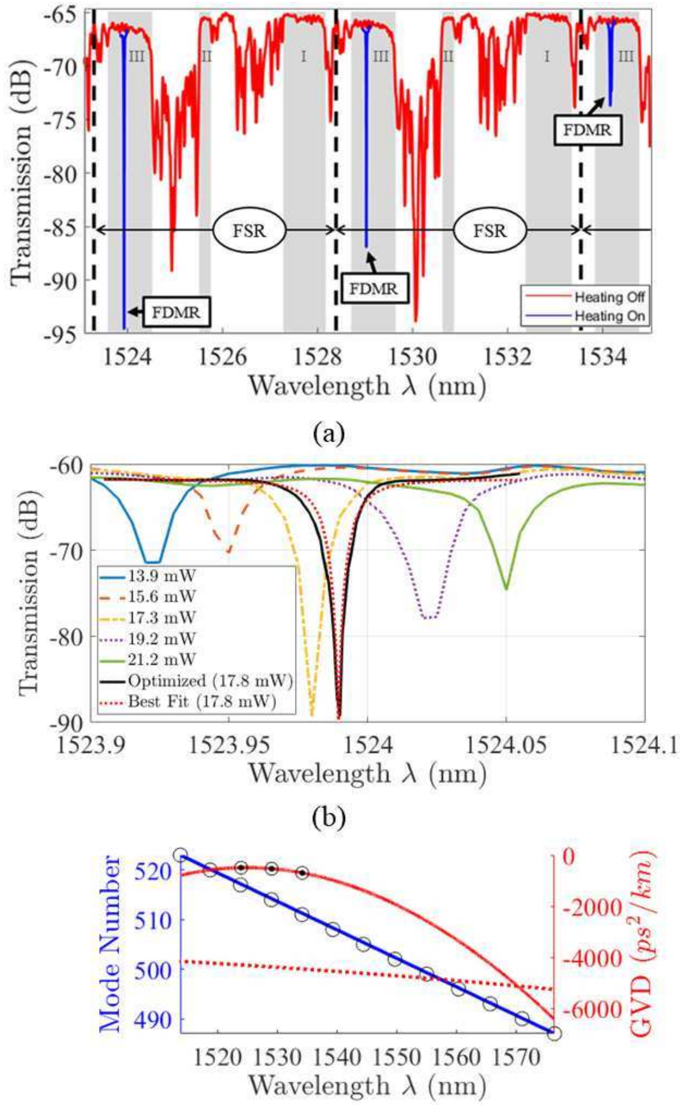

Figure 4.3: (a) Floquet TPI lattice spectrum in red with microring FSR marked by black dashes, FDMR in blue and lattice band gaps in gray. (b) FDMR resonance spectra with heating power from 13.9 mW to 21.2 mW, optimized FDMR achieving a Q-factor here of 7.26×10^4 with fitted curve. (c) FDMR resonance mode number versus wavelength with linear best fit line (blue). The group velocity dispersion computed from experimental resonance wavelengths is shown by solid red line and the simulated dispersion is shown by the dotted line. The black data points at the signal, pump, and idler wavelengths provide group velocity dispersions (β_2) of -495±2, -535±2, and -697±2 ps^2/km, respectively.

hibits the strongest spatial localization as measured by its inverse participation ratio around the band gap center, which is important for achieving strong nonlinear effects. By fitting the resonance spectrum of the FDMR using an all-pass ring resonator model [19], we extracted the effective coupling rate between the FDMR and the edge mode of $\mu = 20.6$ GHz and an effective propagation loss of 4.54 dB/cm in the FDMR loop.

From Fig. 4.3a we observe that the spectral distance separating the FDMR resonance dips is equal to the microring's FSR at 5.1 nm, although the roundtrip length of the FDMR loop is three times the microring circumference. This is due to the fact that the resonance modes in band gaps I and II are suppressed. Figure 4.3c plots the resonance mode number m (blue circles) as a function of the measured resonant wavelength λ_m from 1510 nm to 1580 nm. The resonance mode numbers are determined relative to the value $m = 514$ computed for the 1529.1 nm resonance from the formula $m = 3L \cdot n_{eff}/\lambda_m$, where n_{eff} is the simulated effective index of the microring waveguide at 1529.1 nm and $3L = 329.9$ μm is the effective FDMR roundtrip length. We observe that the FDMR exists over a broad wavelength range with nearly constant mode spacing, as indicated by the best linear fit line. To estimate the GVD of the FDMR mode, we first calculated its propagation constant $\beta(\lambda_m) = 2\pi n_m/\lambda_m$, where the effective index n_m is computed from the resonant wavelengths in Fig. 4.3c as $n_m = m\lambda_m/3L$. We then performed a least-square fit to the β vs. ω dispersion curve using a 4th-degree polynomial and computed the second-order derivative $\beta_2 = d^2\beta/d\omega^2$ to obtain the GVD [90]. Figure 4.3c plots the GVD curve in solid red, from which we obtain experimental GVD values of -495$\pm$2, -535$\pm$2, and -697$\pm$2 ps^2/km at the signal, pump, and idler wavelengths, respectively. For comparison, we also plotted in dashed red the simulated GVD of the FDMR loop obtained by averaging the GVDs of the SOI waveguide sections and the coupling regions comprising the loop. The simulated GVD of the FDMR is comparable to that of a straight SOI waveguide [97], with GVD ~ -4733 ps^2/km around the pump wavelength of 1529 nm, which is larger than the experimental value. It has been demonstrated that GVD is strongly sensitive to cross-sectional area and aspect ratio of the SOI waveguide [98], and this is likely the source of discrepancy between the simulated and experimental values. However, the fact that the experimental GVD is less than or comparable to that of a straight waveguide over the 1510-1580 nm wavelength range demonstrates the low dispersion and broadband nature of the FDMR.

In the FWM experiment, with the heater power set at 17.8 mW, we tuned the signal and pump wavelengths to coincide with the FDMR at 1524.1 nm and 1529.1 nm, respectively. We used the Santec 510 and 210 lasers (Tables 3.1 and 4.2) to independently provide optical power at each wavelength. The spectral shapes of these resonances were similar, with Q-factor of 73,000 at the signal wavelength and 95,000 at the pump wavelength. However, at the 1534.2 nm resonance where the idler wave was generated, a split resonance spectrum was prominent, which was caused by coherent back-scattering into the counter-propagating mode in the FDMR loop and was not observed in neighbor resonances. As a result, we obtained a lower effective Q-factor of 36,000 for this resonance mode. By applying 2.55 mW of optical power for both the pump and signal into the input waveguide, we obtained the wavelength spectrum at the output waveguide in Fig. 4.4, which shows an idler generated at both 1519.1 nm and 1534.2 nm. However, due to a slight red shift in the FDMR resonances caused by the nonlinear thermo-optic effect at high optical powers, the CE, defined as the ratio of the idler power to the signal power, was relatively low, around -46 dB and -49 dB for the up-converted and down-converted idler wavelengths, respectively. This nonlinear thermo-optic red-shift at high optical powers is explored further in Appendix B. To optimize the CE, we swept the pump and signal wavelengths over the corresponding FDMR resonances to obtain the maximum generated idler power. Figure 4.5 shows the variations in the generated idler I power and wavelength as the pump wavelength is swept (Fig. 4.5a) and as the signal wavelength is swept (Fig. 4.5b). In each plot, the darker spectra in the foreground were recorded without the heating power applied, so that no FDMR was induced and the idler I wave was generated purely from FWM of the edge modes propagating along the bottom lattice boundary. The lighter spectra in the background show the idler

Characteristic	Value	Unit
Wavelength Tuning Range	1510-1630	nm
Wavelength Resolution	10	pm
Absolute Wavelength Accuracy	±100	pm
Wavelength Repeatability	±50	pm
Wavelength Stability	±10	pm
Peak Output Power	8	mW
Power Repeatability	±0.01	dB
Power Stability	±0.01	dB
Power Flatness vs. Wavelength	±0.2	dB
Linewidth	1	MHz
Optical Output Connector	FC/APC	
Optical Fiber	SMF	
Communication	GP-IB	
Operating Temperature	20-30	°C

Table 4.2: Santec tunable semiconductor laser TSL-210V performance characteristics. [99]

I power enhancement resulting from the FDMR when the heating power was applied. The pump and signal wavelengths were sampled in 5 pm steps and the spectral shape of each idler I spectrum corresponded to the line shapes of the input lasers.

We observe that the idler power generated by edge mode FWM with the heating power turned off exhibits minimal wavelength dependence, which reflects the flat, wide-band transmission characteristics of the Floquet edge modes across the bandgaps. However, when the heating power was turned on, the peak optical power of the resonance-enhanced idler wave follows the shape of the resonance spectrum of the FDMR, approaching the edge mode results when either the pump or signal was tuned out of the resonance. The peak idler power generated due to FDMR is about 12 dB higher than due to the edge modes alone, and the 3dB bandwidth at which the idler power drops by a half is measured to be 51 pm and 45 pm for the pump- and signal-wavelength sweeps, respectively, which is in agreement

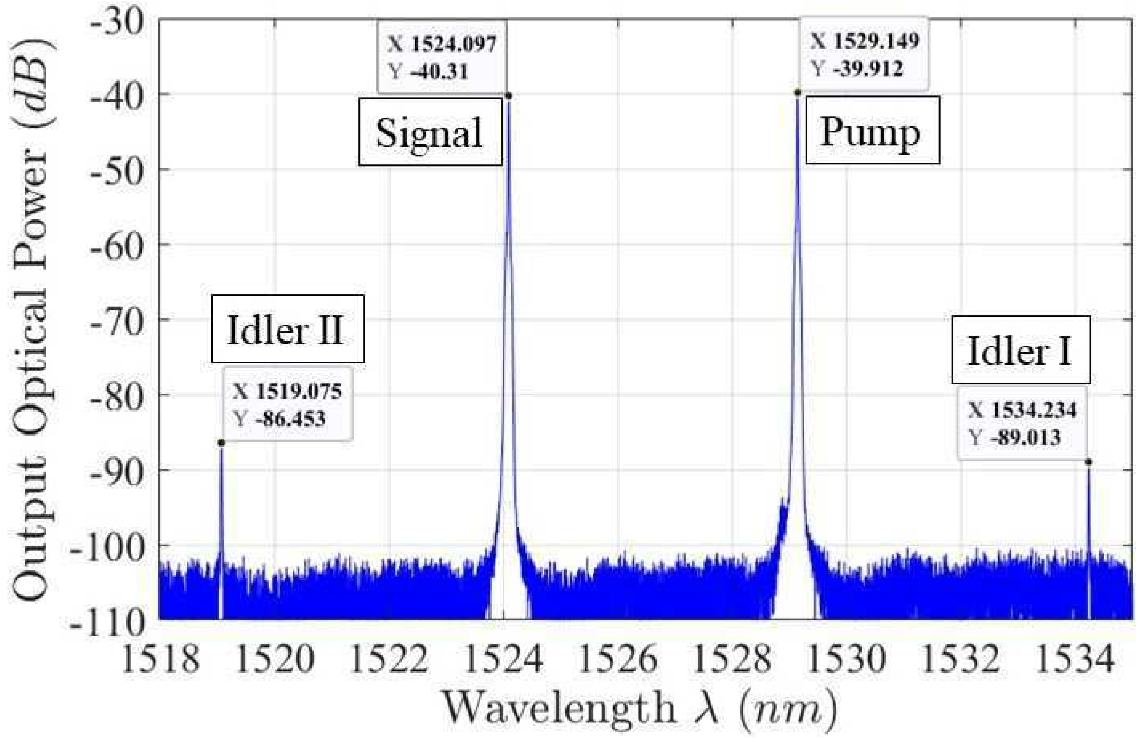

Figure 4.4: Transmission spectrum measured in the output waveguide of the Floquet microring lattice showing the generation of two idler waves by FWM. The pump and signal were tuned to the linear FDMR resonance wavelengths.

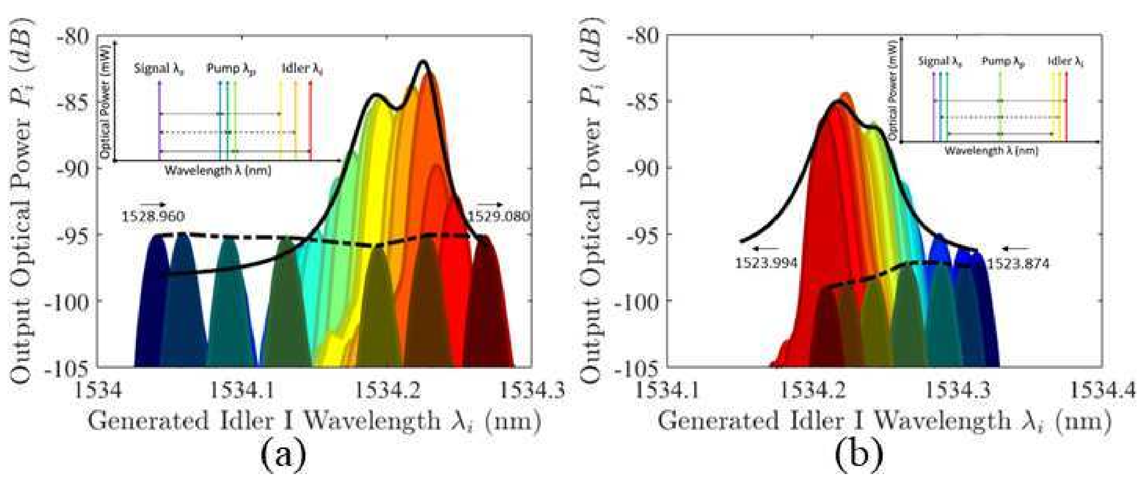

Figure 4.5: Spectra of output optical power at the idler I wavelength. The darker foreground series are recorded without heating power applied showing FWM purely by edge modes; the lighter background series are recorded with a 17.8 mW heater power applied showing enhanced FWM by FDMR present. (a) λ_p swept from blue (1528.960 nm) to red (1529.080 nm) wavelengths, λ_i shifts from blue to red twice as quickly. (b) λ_s swept from blue (1523.874 nm) to red (1523.994 nm) wavelengths, λ_i shifts proportionally in reverse.

with the linewidth of the linear idler FDMR spectrum.

Since the generated idler wavelength is given by $1/\lambda_i = 2/\lambda_p - 1/\lambda_s$, we obtain the rates of change of the idler wavelength with respect to the pump and signal wavelengths to be $\delta\lambda_i/\delta\lambda_p = 2(\lambda_i/\lambda_p)^2$ and $\delta\lambda_i/\delta\lambda_s = -(\lambda_i/\lambda_s)^2$, indicating that the idler wavelength changes twice as fast as the pump wavelength changes and in the opposite direction as the signal wavelength changes. These trends are also confirmed by the wavelength sweeps in Figs. 4.5a and 4.5b. The wavelength conversion bandwidth, defined as the wavelength separation from the signal to the idler waves, is 10.1 nm and spans over 3 Floquet-Brillouin zones of the Floquet microring lattice. Such large conversion bandwidth is enabled by the low dispersion of the Floquet modes in the FDMR.

With the pump and signal wavelengths set at the 1529.1 nm and 1524.1 nm resonances, respectively, we swept the input optical powers of both the pump and signal from 102 μW to 1.23 mW in the input waveguide. At each input power setting, we optimized the spectral locations of the pump (1529.039 nm to 1529.121 nm) and signal (1523.929 nm to 1523.974 nm) wavelengths to maximize the idler power (1534.169 nm to 1534.227 nm). Figure 4.6 compares the CE of FWM enhanced by the FDMR and that due only to the edge modes, as a function of the pump (and signal) power. For comparison, the effective propagation length of the edge modes from input waveguide to output waveguide was 1119 μm, which is more than 3 times the effective circumference of the FDMR loop. For both cases, we observe that the CE increases with input powers, with the FDMR providing a relatively constant average enhancement of 12.5 dB over the edge mode. At the highest available input pump power of 1.23 mW in the input waveguide, we obtained an internal CE of -37.4 dB with the FDMR present and -48.3 dB without. We also note that both CE trends do not show sign of levelling off at high powers, indicating that the detrimental effect of free carrier absorption (FCA) in the silicon microrings is negligible at these input power levels.

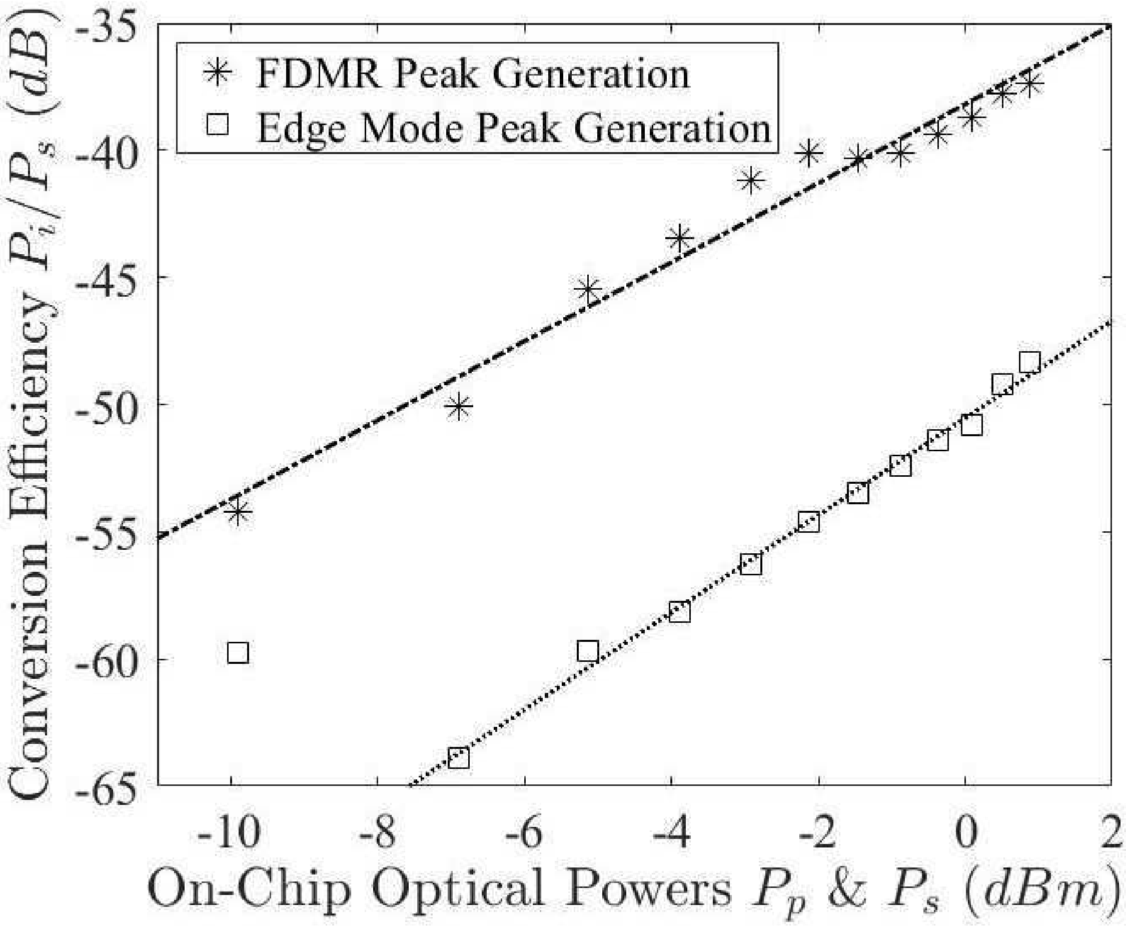

Figure 4.6: FWM CE versus on-chip optical power of pump and signal waves. The linear fits have slopes of 1.55 and 1.91 for the FDMR and edge mode, respectively. On average, the FDMR enhances the CE by 12.5 dB above that of the edge mode.

4.4 Conclusions

The 330 μm roundtrip length of the FDMR gives an effective loop radius of 52.5 μm, allowing our device to be directly compared to that of a 50 μm-radius SOI microring resonator [91]. In their single-ring device, 2 mW of input pump power was required to reach a CE of -35 dB, with saturation effect due to FCA observed at 5 mW of input pump power and a CE of -28 dB. Projecting along the fitted curve in Fig. 4.6, an input pump power of 5 mW would result in a resonance-enhanced CE of -27.3 dB in our FDMR, which is comparable to the single-ring device performance. We note, however, that the FDMR performance is somewhat degraded by mode splitting due to coherent backscattering. By optimizing the device to suppress this effect and achieve optimum trade-off between field enhancement and phase detune caused by the nonlinear thermo-optic effect, it is possible to further improve the CE in the FDMR. The edge mode achieved a CE of -48.8 dB/mm at 1.23 mW pump power, which is comparable to the value of -43 dB/mm reported for a bare silicon waveguide [87] but at a much higher pump power of 15.8 mW. It has also been shown [87] that by using the slow-light effect in a coupled-resonator optical waveguide (CROW) consisting of 8 microrings, a CE improvement of 28 dB over a bare waveguide could be achieved. The same approach can also be used to further increase the CE of our structure by coupling many FDMR loops together. It should be emphasized that while our FDMR provides comparable CE's to those reported for conventional silicon microrings, the main benefit of the FDMR is that it provides a light source directly on a topological platform, which can potentially be used to realize robust photonic devices due to the property of topological protection.

In summary, we report the first demonstration of resonance-enhanced FWM by localized bulk modes in a Floquet TPI lattice using a compact, cavity-less resonance effect induced through a periodic perturbation of the drive sequence. The strongly-localized FDMR, with tunable quasienergy across the TPI bandgap, provides high Q-factors and low dispersion, which enable efficient wavelength conversion over a broad bandwidth. Combined with the topological protection of the Floquet edge modes, the system could provide a robust topological photonic platform for nonlinear optics applications such as wavelength conversion, parametric amplification, frequency comb and entangled photon pair generation. One particular example where the robustness of topologically protected edge modes could have the most impact is in quantum photonic applications, which rely on single photon and entangled photon states that are susceptible to decoherence by device imperfections. Our FDMR can serve as a compact and efficient emitter of single photons that are directly coupled to the edge modes for robust device operations, as will be demonstrated in Chapter 5. [77]

Chapter 5

Resonance-Enhanced Entangled Photon Pair Generation Using Topological Floquet Defect Mode Resonance

As quantum phenomena are sensitive to any form of loss, the benefits of topological photonic insulators (TPIs) and their unique ability to transport light via topologically-protected edge states are amplified for quantum photonic applications. Topological edge states have been used to generate robust quantum photon sources using spontaneous four-wave mixing (SFWM) in silicon topological microring lattices [55, 59]. These structures require high pump powers and long lattice boundaries in order to maximize nonlinear interactions. Resonance-enhancement of photon pair generation by SFWM has been demonstrated in conventional resonators [100], but not on a topological platform, mainly due to the lack of compact, high-Q resonators that can be formed in a topological lattice. Here, we expand upon my previous work on stimulated FWM [77, 101] to exploit the Floquet defect mode resonance (FDMR) [76] and experimentally demonstrate enhancement of entangled photon pair generation. The wavelength-tunable FDMR, with Q-factors up to 10^5 and free spectral range (FSR) $\sim$ 5 nm, was thermo-optically excited in a silicon microring lattice and coupled to a topological edge state, enabling us to achieve second-order cross correlation of photon pairs 1400 times higher than without resonance. These measurements were a collaborative work and were taken with Dr. Afzal at the Integrated Hybrid Quantum Circuits Lab of Professor Shabir Barzanjeh at the University of Calgary.

5.1 Introduction

Entangled photon pairs are quantum light sources which are necessary for quantum information applications, such as quantum walks [102–104], computing, cryptography, and communication [105, 106]. Heralded single-photon sources provide their own applications in linear optical quantum computing (LOQC) [107] and quantum key distribution [108, 109]. Time-correlated photons have been generated on the SOI platform through SFWM in nanoscale waveguides [110–112], photonic crystal waveguides [113], single microring resonators [112], and coupled-resonator optical waveguides [114]. These time-correlated photons are identified through coincidence counting, where two single-photon detectors receive signals at the generated wavelengths in small time-bins. By varying the time delay between the signals, we can identify the coincidence counts which arise from SFWM. A similar result is the heralded single-photon, where the detection of one of the photons in this photon pair would "herald" the existence of the other. The determination of time-correlation does not suffice to determine entanglement, as entangled photons must be correlated in all aspects, not only in time. This is generally probed through a Franson interferometer type experiment by violating Bell's inequality [115, 116], though it can also be proven through rigorous frequency filtering, guaranteeing time-energy entangled photon pairs. Entanglement has been measured on the SOI platform in single microring resonators [100, 117, 118], coupled silicon microring devices [119], and coupled photonic crystal nanocavities [120].

The topological photonic platform can provide improved performance when compared to conventional silicon-on-insulator (SOI) devices through robustness to random fabrication variations. As quantum phenomena are inherently sensitive to any form of loss, this benefit is amplified in the quantum photonics regime. SFWM using edge modes in a Chern insulator based on a 2D lattice of silicon ring resonators has been demonstrated for correlated photon pair generation [59]. More recently, entangled photon emitters have also been achieved by FWM in a silicon anomalous Floquet insulator (AFI) microring lattice [55].

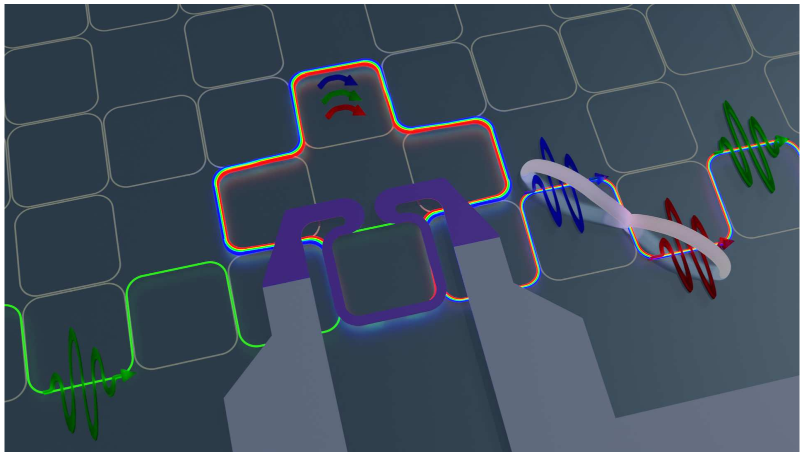

Figure 5.1: Artistic depiction of spontaneous four-wave mixing (SFWM) in an FDMR on a TPI lattice. Input pump light ω_p in green travels along the edge mode from the left. The purple heating element covers the target defect ring. SFWM generates idler photons ω_i in red and signal photons ω_s in blue. The output signal/idler photon pairs are entangled and travel towards the output of the lattice on the right, along with the additional pump photons.

It should be noted that in these works, the nonlinear processes occur via the propagation of edge modes in topological insulators, which require long lattice lengths and high input pump powers for efficient entangled photon pair generation. Having demonstrated stimulated FWM with conversion-efficiency enhancement through FDMR [77, 101], I expanded to SFWM and a demonstration of enhanced entangled photon-pair generation on the same platform. Figure 5.1 provides an artisitc depiction of this SFWM process in an FDMR on a TPI lattice.

5.2 Theoretical Background

SFWM allows us to generate entangled photon pairs for quantum photonics applications. Entangled photon-pair generation in a χ^3 medium is based on spontaneous degenerate four-wave mixing, in which a single input wave serves as the pump, with $\omega_{p1} \equiv \omega_{p2} = \omega_p$. In this case, the solution of $2\omega_p = \omega_s + \omega_i$ can be, and in fact is, solved by any combination of signal and idler frequencies. Vacuum fluctuations allow for any signal and idler pair to be spontaneously generated, and so other efforts must be made to choose what frequency these photons are generated at. In particular, an optical resonator can preferentially enhance

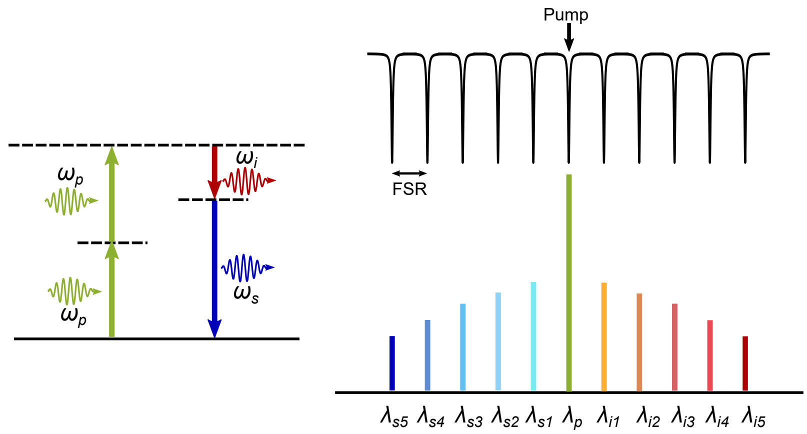

Figure 5.2: (left) Schematic of the energy diagram of spontaneous four-wave mixing (SFWM), with two input pump photons ω_p in green and two output photons, idler ω_i and signal ω_s in red and blue, respectively. (top right) Schematic of the resonance spectrum of an optical resonator, depicting the free spectral range (FSR) and the pump wavelength location. (bottom right) Schematic of output light from SFWM, depicting the wavelength relationship between the pump wavelength, idler wavelengths, and signal wavelengths.

photon pairs at the resonance frequencies. These generated photon pairs are especially interesting to measure as there are no other strong sources at these frequencies, so it is likely that pairs of photons measured at the appropriate $[\omega_s, \omega_i]$ come from the same atomic interaction. More specifically, it is likely these two photons are both emitted from the same atom which has been excited by $2\omega_p$ photons. If they are measured at the same time, these two photons are said to be "time-correlated", providing evidence of this quantum interaction. A schematic of the energy diagram and the expected spectral response of this SFWM process with resonance enhancement are shown in Fig. 5.2.

A relation can be made between the number of photons counted and the coincident counts made with respect to time, the coincidence to accidental ratio (CAR). The CAR is given as a ratio of the true coincidences per accidental coincidence counts per pulse [121] CAR = C/A, and is a function of both the nonlinear process and the measurement equipment. The true coincidences are given by $C = \eta_s \eta_i \mu$, where $\eta_{s,i}$ are the lumped collection efficiencies of the signal and idler photons and μ is the actual number of pairs generated per pulse. The accidental coincidence counts are given by $A = N_s N_i$, where N_s (N_i) are the detected counts by the signal (idler) detectors. $N_{s(i)} = (\mu + \mu_{N_{s(i)}})\eta_{s(i)} +$

$D_{s(i)}$, where $\mu_{N_{s(i)}}$ is the probability of generating a noise signal (idler) photon per pulse and $D_{s(i)}$ is the signal (idler) single-photon detector dark count. Putting these equations together,

$$CAR = \frac{\eta_s \eta_i \mu}{[(\eta_s(\mu + \mu_{N_s}) + D_s)(\eta_i(\mu + \mu_{N_i}) + D_i)]} \tag{5.1}$$

Typical coincident to accidental ratios in silicon microring resonators, reviewed in [122], range from from 37 at 5 μW pump power [123], to 352 at 410 μW [117], to 37 at 4.8 mW [124]. This performance can also be compared to FWM in a TPI edge mode, with a CAR of 42 [59].

The photon pair-generation rate (PGR) in a resonator is given by [122]

$$r = \Delta v[\gamma P^{res}(\lambda) L_{eff}^{res}]^2 \mathrm{sinc}^2\left(\beta_2 \Delta\omega^2 \frac{L^{res}}{2} + \gamma P^{res} L_{eff}^{res}\right) \tag{5.2}$$

where $\Delta v = c/\lambda_P Q$ is the ring resonance bandwidth (Hz), γ is the waveguide nonlinearity ($\gamma = \omega n_2/cA_{eff}$, where A_{eff} is the effective area of the waveguide, c is the speed of light, n_2 is the Kerr nonlinearity, and ω is the pump angular frequency), $\Delta\omega$ is the pump-signal (pump-idler) angular frequency separation, β_2 is the second-order waveguide dispersion and *res* indicates the resonantly enhanced quantities:

$$P^{res}(\lambda) = P \times \frac{F}{\pi} \times \frac{(\lambda_P/2Q)^2}{(\lambda - \lambda_P)^2 + (\lambda_P/2Q)^2} \tag{5.3}$$

$$L^{res} = L \times \frac{F}{\pi} \tag{5.4}$$

$$L_{eff}^{res} = \frac{1 - e^{-\alpha L}}{\alpha} \times \frac{F}{\pi} \tag{5.5}$$

where $F = Q\lambda_P/n_g L$ is the cavity finesse, with n_g and α the group index and propagation loss of the ring resonator waveguide at λ_P (in a circular microring, $L = 2\pi R$).

The equation for pair generation rate in a straight waveguide is provided in [125],

$$r = \Delta v[\gamma P_0 L_{eff}]^2 \mathrm{sinc}^2\left(\beta_2 \Delta\omega^2 \frac{L}{2} + \gamma P_0 L\right) \tag{5.6}$$

where P_0 is the input pump power. It follows the same form as that for the resonator, but without resonance-enhanced parameters of effective length and power.

The correlation of photon pairs is characterized using the second-order cross-correlation function, $g_{si}^{(2)}(t)$, which provides the normalized probability of detecting signal and idler photons separated by time t [126], given by

$$g_{si}^{(2)}(t) = \frac{N_{si}}{R_s R_i} \times \frac{1}{T_{Acq} T_{CoinW}} \tag{5.7}$$

where N_{si} is the number of coincidence counts within the coincidence window, $R_{s/i}$ is the incidence rate of the signal/idler photons, T_{Acq} is the coincidence counting period and T_{CoinW} is the width of the coincidence window. For correlated photon pairs, we expect $g_{si}^{(2)}(0)$ to have an inverse power dependence, and $g_{si}^{(2)}(t)$ to have a peak within the range of $t = 0$.

The second-order cross-correlation is called such as it is proportional to the second power of the electric field, or the intensity of the electric field. [127] This characteristic allows us to classify light as antibunched, coherent, or bunched. Chaotic, or bunched light provides $g^{(2)}(0) > 1$, perfectly coherent light, with a random photon spacing, has $g^{(2)}(\tau) = 1$ for all τ, while antibunched light exhibits $g^{(2)}(0) < 1$. For classical light, $g^{(2)}(0) \geq 1$ and $g^{(2)}(0) \geq g^{(2)}(\tau)$, therefore, both bunched and coherent light are consistent with classical optics, while antibunched is purely a non-classical phenomenon.

In the entangled light source case, we look for the bunched behaviour in the cross-correlation function as it suggests the photons are being emitted at the same time, ie. from the same atomic event. As for the auto-correlations, the single-wavelength paths should be completely random and provide a coherent source behaviour.

5.3 Experimental Realization

Our Floquet TPI was based on a 2D square microring lattice described in Chapter 4 [77], with each unit cell (shown in Fig. 5.3a) consisting of 3 identical microrings. An SEM image of the lattice with 10×10 unit cells is shown in Fig. 5.3a. The transmission spectrum is shown in red in Fig. 5.5a, from which we can identify topologically nontrivial bandgaps by

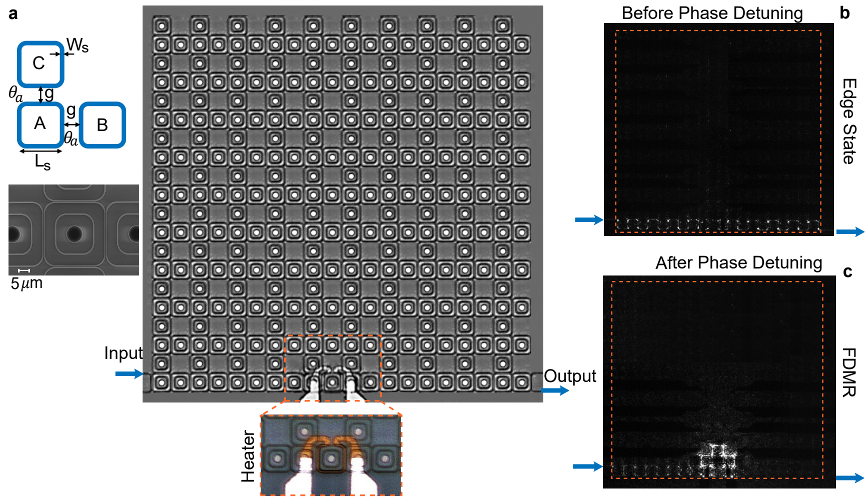

Figure 5.3: (a) (top left) Schematic unit cell, $W_s = 450$ nm, $L_s = 19.64$ μm, $\kappa_a = 0.99$ or $\theta_a = 0.455\pi$. (bottom left) SEM image of a single rounded-square microring resonator. (center) SEM image of 10 x 10 unit cell Floquet TPI lattice with (inset) metallic heater along the bottom edge. (b) NIR image of edgemode, observed before phase detune is applied. (c) NIR image of FDMR, observed after phase detune is applied.

regions of high and flat transmission (labeled I, II, and III in each FSR). An NIR image of the edge mode is shown in Fig. 5.3b and an NIR image of the FDMR is shown in Fig. 5.3c. The simulated spatial distribution of the mode is presented in Fig. 5.4, with most of the light localized to the FDMR loop in the center of the bottom edge of the lattice. The transmission spectrum in the output waveguide with 11 mA of heater current applied is shown by the blue trace in Fig. 5.5a. We observe the appearance of sharp resonance dips in each bandgap of each FSR, indicating the excitation of a resonance mode coupled to the edge state. The resonance wavelength can be tuned by varying the heater current.

For our silicon devices, we expected a Kerr nonlinearity of about $n_2 \sim 4.5x10^{-18}\ m^2/W$ [128]. From Lumerical simulations of our silicon microring waveguide [79], we obtained $A_{eff} = 0.197\mu m^2$, $n_{eff} = 2.35$, and $n_g = 4.31$ using values at 1550 nm of $n_{Si} = 3.47$ and n_{SiO_2} = 1.44. For our FDMR with round-trip length $L = 330\mu m$, pictured in Fig. 5.3c and simulated in Fig. 5.4, operated around the 1529 nm wavelength range, we measured average Q-factors of 70,000 providing a finesse $F \sim 75$. From measurements of the FDMR resonance spectra, we also calculated $\alpha \sim 4.54$ dB/cm, $\beta_2 \sim -535$ ps^2/km, with $\Delta\nu = 2.76 \times 10^9$ Hz

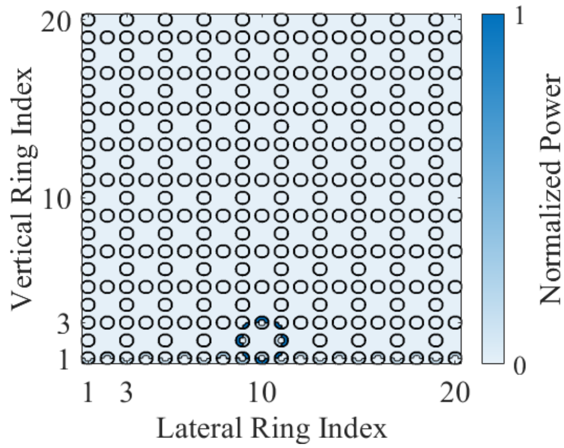

Figure 5.4: Simulated spatial distribution of FDMR coupled to the topological edge mode.

resonance bandwidth. From these parameter values, we obtained $\gamma = 101 m^{-1} W^{-1}$, and $L_{eff}^{res} = 11 \times 10^{-3}$m. The power in the resonator at resonance depends on both the input power and the detune from the resonant wavelength, as given by Eq. 5.3. Assuming the pump wavelength exactly matches the center of the FDMR resonance, $P^{res}(\lambda) = P \times 33.3$, where P is the input power in the waveguide.

The final pair-generation rate depends on both the input laser power and the spectral distance between the input laser and the generated signal frequency. For example, choosing $\Delta\omega = (2\pi) * 6.410^{11}$ Hz and an in-waveguide power of ~ 1.23 mW pump power, the expected PGR is given by $r \sim 4 \times 10^6$ Hz. Comparing reported results in microring resonators, [122] provides a review of PGRs in silicon microring resonators, from 165 Hz at 5 μW [123], to 21 MHz at 410 μW [117], to 123 MHz at 4.8 mW [124]. Figure 5.6 provides a plot of the theoretically expected photon pair generation rate vs. pump power in the FDMR and using the edge mode alone. These results show a 13,000 times improvement in the pair generation rate when enhancing the spontaneous FWM interaction with a resonance, compared to a waveguide of the same length as the FDMR roundtrip length.

Our experimental setup is based on [111] for time-correlation measurements, with frequency filtering added to the signal- and idler-collection paths to ensure time-energy entanglement. Figure 5.7 describes our experimental setup for measuring time-correlated photon

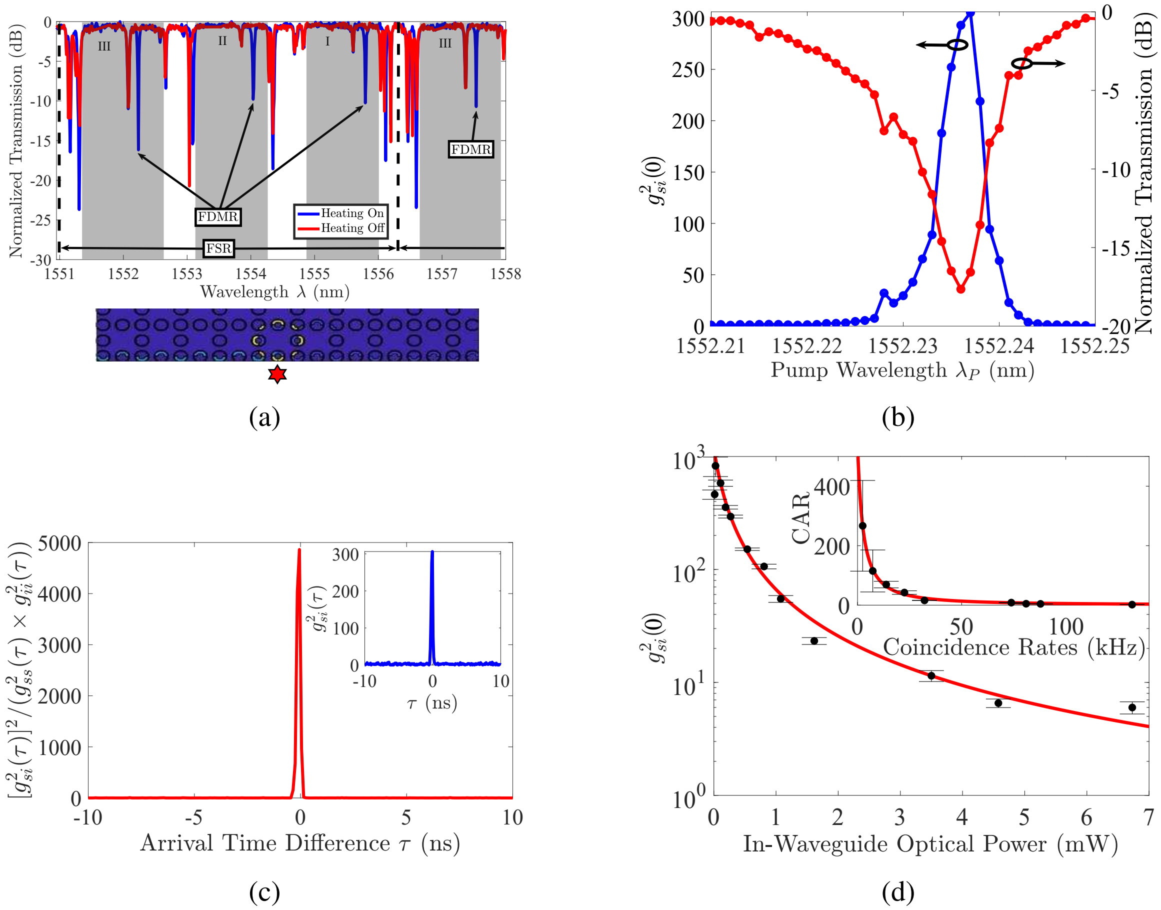

Figure 5.5: Experimental results from the first round of measurements. (a) Normalized transmission spectrum covering 1.3 FSR of the Floquet microring lattice (dB) versus wavelength (nm) with no heater current in red, and 11 mA heater current in blue. (bottom) Simulated spatial distribution of FDMR, heater marked by red star. Adapted from [77]. (b) Second-order cross-correlation $g_{si}^{(2)}(\tau)$ at $\tau = 0$ versus pump wavelength (nm) in blue, compared to a normalized transmission spectrum of the FDMR (dB) in red. (c) The Cauchy-Schwarz relation versus arrival time difference (ns) in red, where the inequality is violated in the coincidence window of -400 $\leq \tau \leq$ 400 ps. (inset) Second-order cross-correlation $g_{si}^{(2)}(\tau)$ versus arrival time difference (ns) in blue, where the peak at $\tau \equiv 0$ demonstrates time-correlated photons. (d) Second-order cross-correlation $g_{si}^{(2)}(\tau)$ at $\tau = 0$ versus in-waveguide optical pump power (mW) in black, with a guide to the eye in red. (inset) Coincidence-to-accidental ratio (CAR) versus coincidence count rate (kHz) in black, with a guide to the eye in red.

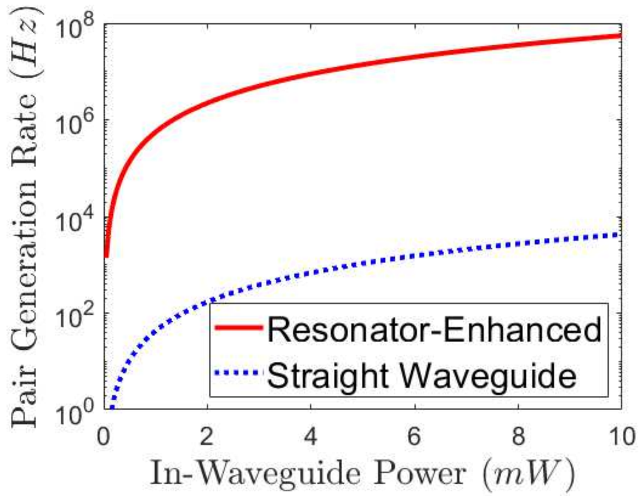

Figure 5.6: Theoretically expected photon pair generation rate (Hz) versus in-waveguide pump power (mW), with resonance-enhancement in red and a straight waveguide in dashed blue.

pairs. The pump photons are provided by a tunable semiconductor continuous-wave laser at telecom wavelengths. An erbium-doped fibre-amplifier (EDFA) could increase the power of the input pump signal, however the use of the amplifier necessitates a band-pass filter which rejects the amplified spontaneous emission (ASE) surrounding the target wavelength of the laser. In our experiment we found the noise floor of the laser to be quite significant and the generation without amplification substantial enough to forgo the implementation of an EDFA. On the SOI chip, the signal and idler photons are generated through SFWM. The three wavelengths are then collected at the output fibre, where the light is first sampled by a 99:1 splitter for alignment and power measurements. Next, the light is split by a 50:50 coupler and the signal and idler photons are filtered by tunable 25 GHz filters, with stop-band rejection of -40 dB, centered at the signal and idler wavelengths. Time-correlation measurement was performed through coincidence counting using two superconducting-nanowire single-photon detectors (SNSPDs) and a time-correlated single photon counter, with a timing resolution of 100 ps. The SNSPDs used in this experiment were ID Quantique - ID281, whose performance characteristics are summarized in Table 5.1. We could have employed time-gating in the experiment through the use of an electro-optic modulator, which would

Characteristic	Value	Unit
System Detection Efficiency (SDE)	$\geq$90	%
Maximum Dark Count Rate	<100 - <1	cps
Maximum Detection Rate	>30	Mcps
Timing Jitter	<30	ps
Output Pulse Width / Voltage	>5 / >100	ns / mV

Table 5.1: ID Quantique - ID281 superconducting-nanowire single-photon detector performance characteristics. [129]

reduce the average number of accidental coincidence counts more aggressively the total number of coincidence counts. However, as our pair generation rate at low powers was already so low, we did not want to reduce our generation further.

Measurements of coincidence counts were taken for various levels of pump power, pump-signal frequency separation within an FSR versus across multiple FSR, and with the FDMR turned on versus using the topological edge mode only. With the FDMR turned on, coincidence counts were measured against detuning of the pump wavelength from the target resonance.

In the SFWM experiment, we applied a pump beam with in-waveguide powers between 0.01 mW and 7.5 mW at the 1552.236 nm FDMR resonance wavelength. With 270 μW of in-waveguide optical power, the normalized resonance spectrum is shown in red in Fig. 5.5b with a Q-factor of 74,000. The correlation of detected photons was characterized using the 2nd-order cross-correlation function, $g_{si}^{(2)}(\tau)$. The peak of $g_{si}^{(2)}(\tau)$ at $\tau \equiv 0$ in blue in the inset of Fig. 5.5c demonstrates time-correlated photons for 270 μW of in-waveguide pump power at 1552.236 nm. A formal proof of a non-classical light source requires the violation of the Cauchy-Schwarz inequality, $\left[g_{si}^{(2)}(0)\right]^2 / \left[g_{ss}^{(2)}(0) \cdot g_{ii}^{(2)}(0)\right] \leq 1$. By measuring the self-correlation counts for signal/idler ($g_{ss/ii}^{(2)}(0)$) with either the idler/signal photon path blocked, the Cauchy-Schwarz relation is measured and shown in red in Fig. 5.5c, where the inequality is violated in the coincidence window of -400$\leq \tau \leq$ 400 ps. To in-

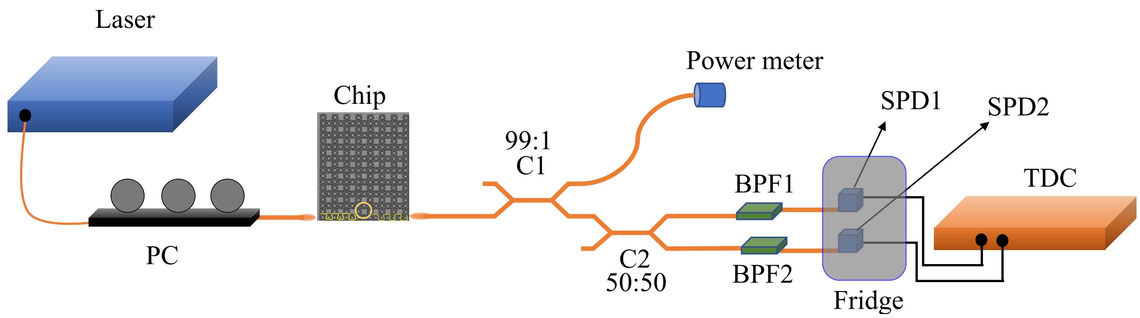

Figure 5.7: Time-correlated photon pair experimental setup schematic. A continuous-wave (CW) laser produces the λ_p wave, which is modulated by the electro-optic modulator (EOM) through a radio-frequency (RF) pulse generator. This modulated pump is then amplified by the erbium-doped fibre amplifier (EDFA), which makes the rejection of the amplified spontaneous emission (ASE) noise a necessity with a narrow band-pass filter (BPF). This amplified pump is then coupled to the silicon-on-insulator (SOI) chip where FWM generates the λ_S and λ_i waves which are then separated by wavelength demultiplexing (WDM). The pump is then filtered from the output waves through another BPF. Finally, the output signals are refined through a BPF each to be counted at the superconducting-nanowire single-photon detectors (SPDs). The electronic signals are then sent to the time correlator, which measures the number of correlated photon pairs measured. Based on the setup from [111].

vestigate the resonance-enhancement of the FDMR, the wavelength of the pump photons was swept across one resonance, allowing for $g_{si}^{(2)}(0)$ to be compared to the strength of the resonance, as shown in Fig. 5.5b. The peak of cross-correlation in blue coincides with the deepest point of the transmission of the resonance in red, demonstrating successful resonance-enhancement of the generation of entangled photon pairs, with 2nd-order cross-correlation up to 300 times stronger than off-resonance. We also experimentally determined the power dependencies of $g_{si}^{(2)}(0)$ and the CAR, both demonstrating the expected inverse power relationship as shown in Fig. 5.5d. We expect these values to decrease as the input optical power increases because the denominators, driven by accidental counts and noise, will increase faster than the numerators, the detection of real coincidence counts or photon pairs.

In a second round of measurements, we took more care in our experimental setup and increased our integration time. We applied a pump beam with in-waveguide powers be tween 0.08 mW and 1.7 mW at the 1545 nm FDMR resonance wavelength. With 285 μW of in-waveguide optical power, the normalized transmission spectrum of the lattice is shown in Fig. 5.8a, with the blue trace measured without phase detuning and the orange trace measured after phase detuning. The FDMR resonance spectrum at 1545.27 nm is show in red in Fig. 5.8b. In this run, the signal and idler spectral locations were at FDMR wavelengths two FSR below (1535 nm) and above (1555 nm) the pump wavelength. The peak of $g_{si}^{(2)}(\tau)$ at $\tau \equiv 0$ in blue in the inset of Fig. 5.8c again demonstrates time-correlated photons for 285 μW of in-waveguide pump power at 1545.27 nm. The Cauchy-Schwarz relation is again measured and shown in red in Fig. 5.8c, where the inequality is violated in the coincidence window of -400 $\leq \tau \leq$ 400 ps. As shown in Fig. 5.8b, the peak of cross-correlation in blue again coincides with the deepest point of the resonance in red, demonstrating successful resonance-enhancement of the generation of entangled photon pairs, this time with 2nd-order cross-correlation up to 1400 times stronger than off-resonance. This value is about 9 times smaller than the resonance improvement expected in the pair generation rate. Again, the power dependencies of $g_{si}^{(2)}(0)$ and the CAR, both demonstrated the expected inverse power relationship as shown in Figs. 5.8d and 5.8e. Finally, we recorded the on-chip coincidence rate vs in-waveguide optical power in order to compare to other works which quote coincidence rate without referring to an optical power. This relationship is shown in Fig. 5.8f.

5.4 Conclusions

In summary, we demonstrated resonance-enhanced generation of entangled photon pairs through SFWM in a silicon TPI platform using an FDMR coupled to a topological edge mode. The high-Q, compact size, and thermo-optical tunability of the FDMR can be exploited to realize efficient, robust, and tunable quantum sources on a topological nanophotonic platform. [130, 131]

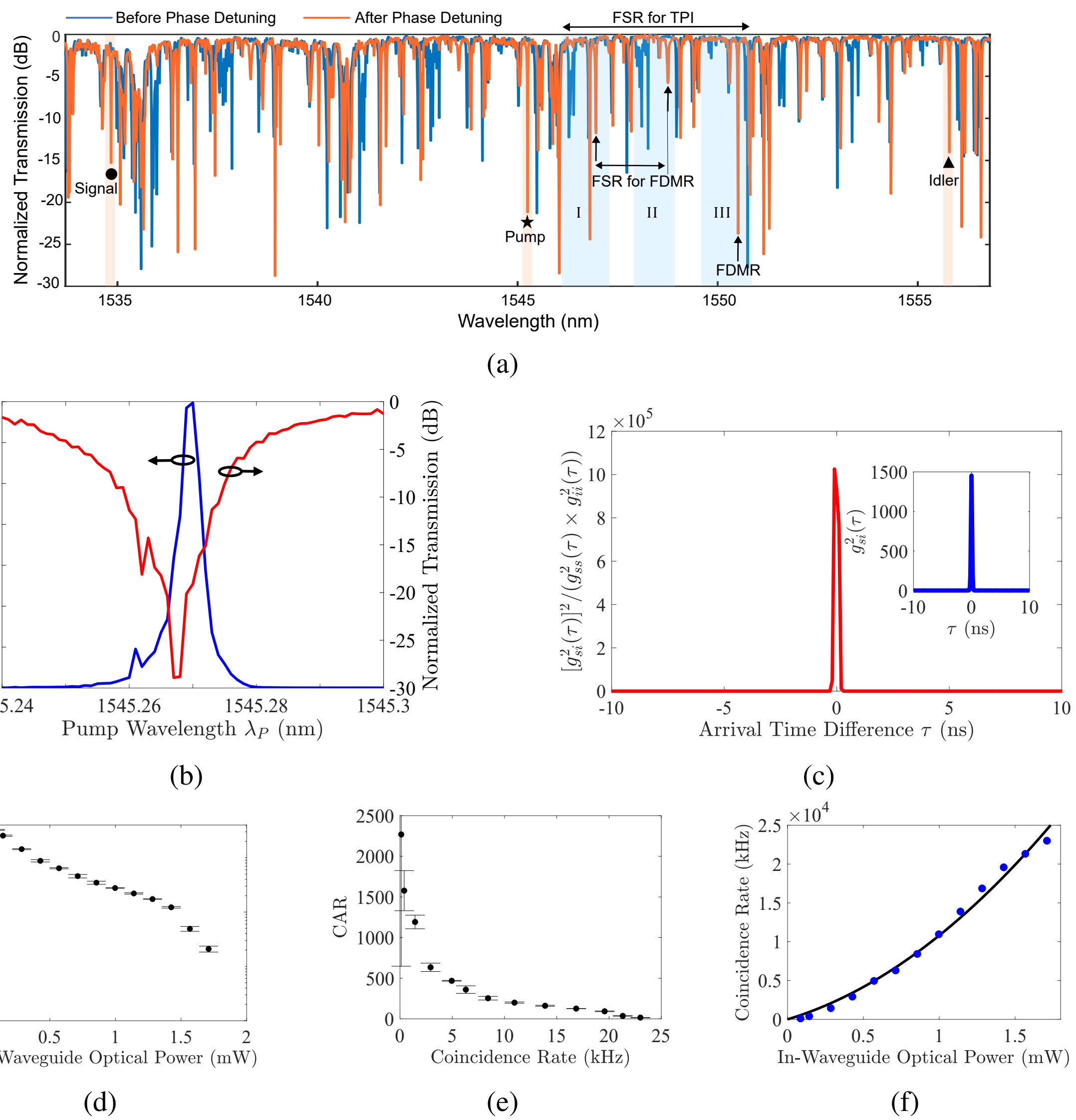

Figure 5.8: Experimental results from the second round of measurements. (a) Normalized transmission spectrum covering 4 FSR of the Floquet microring lattice (dB) versus wavelength (nm) with no heater current in orange, and 11 mA heater current in blue. (b) Second-order cross-correlation $g_{si}^{(2)}(\tau)$ at $\tau = 0$ versus pump wavelength (nm) in blue, compared to a normalized transmission spectrum of the FDMR (dB) in red. (c) The Cauchy-Schwarz relation versus arrival time difference (ns) in red, where the inequality is violated in the coincidence window of -400 $\leq \tau \leq$ 400 ps. (inset) Second-order cross-correlation $g_{si}^{(2)}(\tau)$ versus arrival time difference in blue, where the peak at $\tau \equiv 0$ demonstrates time-correlated photons. Measured for 285 μW of in-waveguide pump power at 1545 nm. (d) Second-order cross-correlation $g_{si}^{(2)}(\tau)$ at $\tau = 0$ versus in-waveguide optical pump power (mW). (e) Coincidence-to-accidental ratio (CAR) versus coincidence rate (kHz). (f) Coincidence rate (kHz) versus the in-waveguide optical pump power (mW) in blue, with a fit plotted in black.

Chapter 6

Active Photonic Applications of Floquet Defect Mode Resonance in Modulation and Routing

We explored routing and modulation on a topological platform by utilizing specially fabricated lattices with embedded pn junctions and multiple metallic heaters. Modulation of the FDMR using pn junctions was generally unsuccessful. While a small resonance dip was observed to move with bias voltage, the extinction was less than 3 dB and modulation of the bias voltage did not result in a noticeably modulated signal. The cause of this poor performance may be high loss in the defect ring or significant coupling coefficient changes caused by the doped silicon. The same pn junction structure was applied to a single all-pass microring resonator (APMR) of circumference comparable to a rounded-square microring in the lattice. This structure successfully modulated a 27.4 dB transmission dip in the optical power with up to 24.6 dB of voltage modulation, at a 3 dB bandwidth of 348 MHz. Considering the optical resonance demonstrated a bandwidth of $\sim$ 4.29 GHz, and the maximum bandwidth measured directly from a tabletop function generator was 370 MHz, we believe this measurement of the modulation bandwidth was limited to the capabilities of the experimental equipment. In pursuit of routing light across the lattice, 4 Floquet defect mode resonance (FDMR) were successfully coupled together, routing light in a CROW-like manner. This came with the same difficulties in alignment of resonant wavelengths as is experienced in fabricated CROW structures. A drop port transmission peak of 3.45 dB was observed, in conjunction with NIR images showing the spatial pattern of light crossing the lattice.

6.1 Introduction

This project aims to expand the application of topological photonic insulators to active (electrically-controlled) photonic devices. I have shown that introducing a phase-detune to a target defect ring along the edge of the lattice can shift a bulk mode into the bandgap of the Floquet lattice, producing an FDMR. By embedding a pn junction in the FDMR loop, it is possible to electrically modulate the resonant frequency at high speed through the plasma effect. This fast resonant frequency change can be used for signal modulation, optical switching, and light routing [132–134], all on a photonics platform which is topologically robust to lattice-level defects. This allows for the implementation of on-off switches, time gating, and modulation even at single-photon levels. Furthermore, the application of multiple defect rings, inducing multiple FDMR, allows for the investigation of coupled FDMR structures.

6.2 Theoretical Background

The devices and structures submitted to the AMF Silicon Photonics fabrication process allowed us to experimentally explore the applications of FDMR for optical modulation and routing. Thermo-optic heaters using TiN layers were implemented for large, time-independent phase-shifts, while pn junctions along the silicon rib waveguide provided modulation through free-carrier injection. There were two different TPI lattice designs, one 10x10 unit cell lattice with both TiN heaters and pn junctions for optical modulation and one 10x5 unit cell lattice with only TiN heaters to explore routing and slow-light structures. Each device uses 3 rounded-square microrings per unit cell, with each microring approximately 30 μm x 30 μm in size and coupling gaps on the order of 252 nm.

In the optical modulation design, a defect ring along the bottom edge is fitted with both a resistive heater element and a pn junction modulator, a schematic of which is provided in Fig. 6.1a. The resistive element provides significant phase detune to the bottom half of the target ring through the thermo-optic effect, moving a bulk mode of the lattice into the bandgap of the lattice. The pn junction serves to inject free carriers into the silicon rib waveguide, providing a fast change in the resonant frequency of this target mode, resulting in a modulation of the transmitted signal. The cross-sectional schematic of the pn junction is shown in Fig. 6.2. This process is outlined in time in Fig. 6.3a and in wavelength in Fig. 6.3b. The edge mode of the lattice is unaffected by either of these effects since the perturbation is only local to the location of the FDMR. A second defect ring further along the bottom edge of the lattice is fitted with a heating element with two pn junctions located along the generated FDMR, a schematic of which is shown in Fig. 6.1b. The heater serves the same purpose as in the first defect ring, but the pn junctions are situated on different rings. This device would allow us to investigate the time dependence of these phase perturbations as the phase added on each side of the FDMR can be driven independently of the other. Having only 1 set of high-speed probes limited our ability to investigate these effects. Transmission measurements were made at the through port and the output port of the TPI lattice. We further characterized the dependence of the FDMR resonant frequency and quality factor on the heating current applied, as well as the performance of the pn junctions. We also explored the modulation bandwidth of the heater/pn junction combination.

In the signal routing design, presented in Fig. 6.4, 3 defect rings were chosen in a vertical pattern to provide 4 FDMR loops which span the height of the lattice, connecting the input optical signal to “OUTPUT 3” through a series of coupled resonances. These 4 coupled FDMRs form a 1D array of coupled resonators, or “Coupled Resonator Optical Waveguide” (CROW) structure, which could function as a basis for slow-light applications, such as further enhanced FWM. A further 3 defect rings were chosen horizontally between the vertical CROW and the right edge of the lattice. This set of 6 FDMR form a second CROW structure which connects the input optical signal to “OUTPUT 2”, through a total of 9

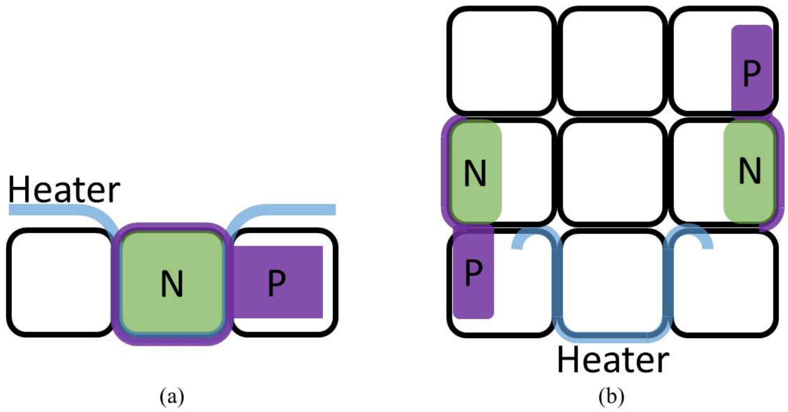

Figure 6.1: Schematic of the modulation devices with (a) a combination of heater (blue) and pn junction (purple/green) on the same defect ring and (b) a heater (blue) defect ring with two independent pn junctions (purple/green) located on opposing sides of the heater-induced FDMR.

FDMR. The coupling between ring 3 and 4 would experience a phase shift as the 1D CROW lattice is sheared by 90 degrees. Transmission measurements were made at the through port and the 3 output ports as various combinations of FDMR are generated. The heating current applied to each defect ring was tuned to align the resonant frequencies and achieve strong CROW filter behaviour.

6.3 Experimental Realization

6.3.1 Floquet Defect Mode Resonance in Modulation

The pn junction modulation was first tested using a 20 μm radius microring, giving a circumference of 125 μm, which is approximately the circumference of a single rounded-square resonator in the TPI lattices. A microscope image of one of these APMR filters is shown in Fig. 6.5. The pn junction layout is similar to that in Fig. 6.1a. The coupling gap between the resonator and the bus waveguide is 375 nm, giving an estimated coupling strength $\kappa \sim 0.1742,\ \kappa^2 \sim 0.0304$. With the relation $\tau = \sqrt{1-\kappa^2}$, this suggests a $\tau \sim 0.9847,\ \tau^2 \sim 0.9696$. Using the resonance spectra of the ring resonator, we are able to fit the minimum transmission T_{min} and the contrast of the cavity F using a custom MATLAB least-squares fitting function with $T = \frac{T_{min}+F*\sin(\phi/2)^2}{1+F*\sin(\phi/2)^2}$. These characteristics are related to

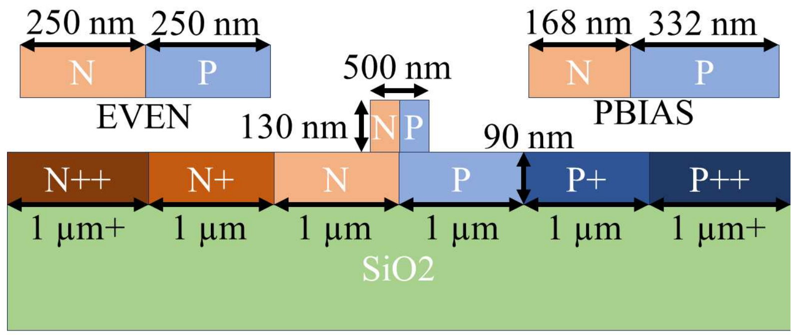

Figure 6.2: Cross-sectional schematic of the pn junction. The distinction between the EVEN and PBIAS junction designs is highlighted at the top corners of the figure, where the EVEN junction has p and n-doped regions 250 nm wide, while the PBIAS junction has a wider p-doped region of 332 nm, compared to the n-doped region of 168 nm.

the transmission coefficient τ and roundtrip attenuation coefficient α_{rt} via $T_{min} = \left(\frac{\tau - a_{rt}}{1-\tau a_{rt}}\right)^2$ and $F = \frac{4\tau a_{rt}}{(1-\tau a_{rt})^2}$. The resonance spectra with their fits are shown in Fig. 6.6. These fits provided $\tau^2 = 0.9742$ and 0.9697 and $a_{rt} = 0.9845$ and 0.9840, which suggests a propagation loss of 10.8 dB/cm to 11.1 dB/cm. These fits also return Q-factors of 46,147 and 44,052, with optical bandwidths of 4.19 and 4.38 GHz and extinction of 27.4 dB and 25.8 dB.

The Agilent E4438C ESG Vector Signal Generator provided an RF output voltage between 250 kHz and 3.0 GHz, providing up to 20 mW of high frequency modulated electrical power. This signal was transmitted to the high-speed probe using a Pasternack Enterprises Flexible RG58 Coax Cable with a 50 Ω impedance and a maximum operating frequency of 5 GHz. The highspeed probe was a Picoprobe 40A-GS-330-EDP, with a bandwidth of 40 GHz, a ground and signal probe, 330 micron spacing between the probe tips, and an extended diagonal probe. The modulated optical signal was measured by an EOT Amplified InGaAs Detector ET-3500AF with a bandwidth of 20 kHz to 10 GHz, the performance characteristics of the highspeed photodetector are summarized in Table 6.1.

The current-voltage relationship of the pn junction, specifically the one fabricated on the FDMR modulation lattice, is provided in Fig. 6.7a. The cross-sectional structure of

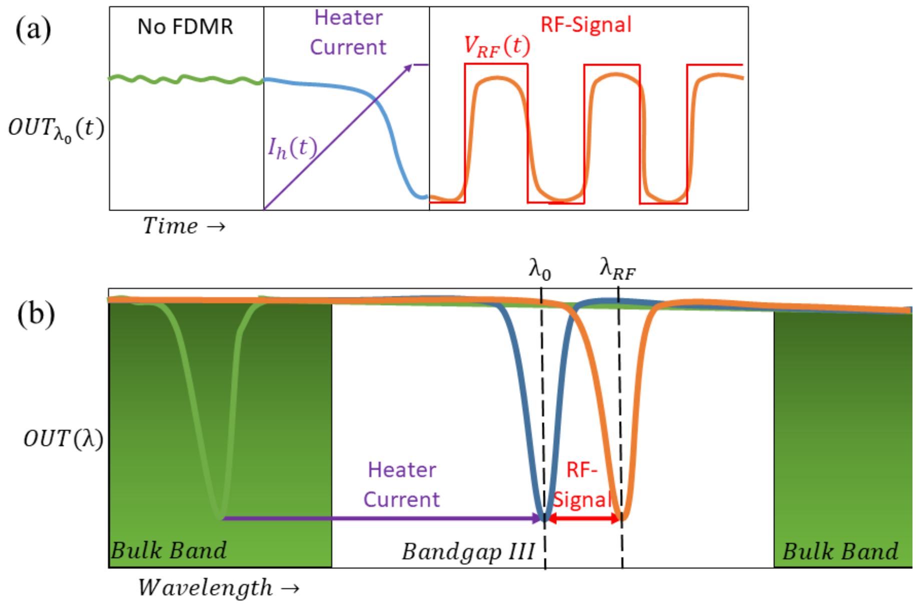

Figure 6.3: (a) Output optical power at the center wavelength versus time as no phase is applied (green), as the heater current $I_h(t)$ is applied (blue), and finally as the pn junction bias voltage $V_{RF}(t)$ is modulated (orange). (b) Output optical power spectrum under the three conditions produced by no phase applied (green), the heater current applied (blue), and the pn junction bias voltage applied (orange).

the pn junction was identical between the FDMR lattice and the single APMR modulator. The modulation bandwidth of the 1550.502 nm resonance of the APMR is presented in Fig. 6.7b. The modulator was operated at -1.5 V offset with V_{pp} of 2.4 V, meaning the entire modulation occurs in the reverse bias, low current regime, relying entirely on the field effect to move the density of free carriers in the junction.

The two lattices used to explore high-speed modulation of the FDMR are pictured in Fig. 6.8a and Fig. 6.8b. Their designs are identical apart from the thickness of the p-doped region of the junction. The first design had p and n-doped regions 250 nm wide, while the second design had a wider p-doped region of 332 nm, compared to the n-doped region of 168 nm. The full transmission spectrum of the even modulation lattice is presented in Fig. 6.9. When moderate heating current was applied to the defect ring resonator (shown in blue), there were small transmission dips introduced to the regions of high transmission in the lattice (shown in red). However, upon investigating these transmission dips further, their

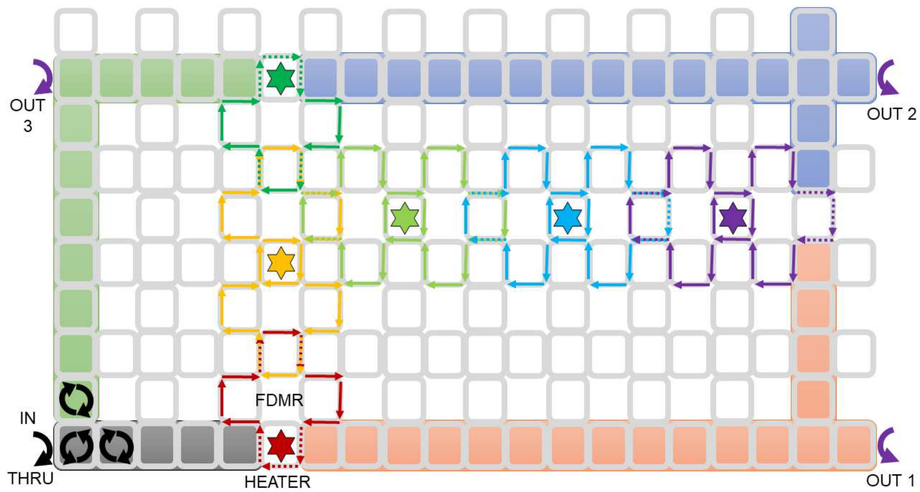

Figure 6.4: Schematic of the FDMR signal routing device. The defect rings are marked by stars and their corresponding FDMR are outlined with coloured arrows, indicating the left-handedness of the resonances. The edge modes are marked with coloured sections, where the colour changes after interacting with an FDMR. There is one input port IN, a through port THRU, and three drop ports, OUT 1, 2 and 3.

extinction was only on the order of 3 dB, as demonstrated in Fig. 6.10. While introducing the FDMR through applied heating current certainly affected the flat, high-transmission edgemode behaviour, the quality factor of the introduced resonances was extremely low. As such, modulation of the FDMR at high frequencies was not observed. Applying no heating current isolated the pn junction bias voltage, where Fig. 6.11 demonstrates no change in the transmission spectra between 0 V and 5 V of reverse bias voltage applied to the pn junction.

Clearly the fabricated devices on this chip are capable of supporting high-Q resonances, as demonstrated by the single APMR structure. Additionally, the pn junction design is capable of modulating the effective index of the APMR structure at high speed. However, the implementation of this pn junction via doped silicon integrated into the TPI lattice is preventing the effective implementation of FDMR. The next subsection will demonstrate that FDMR can still be introduced effectively in the routing lattice through the thermo-optic effect using only the metallic heaters.

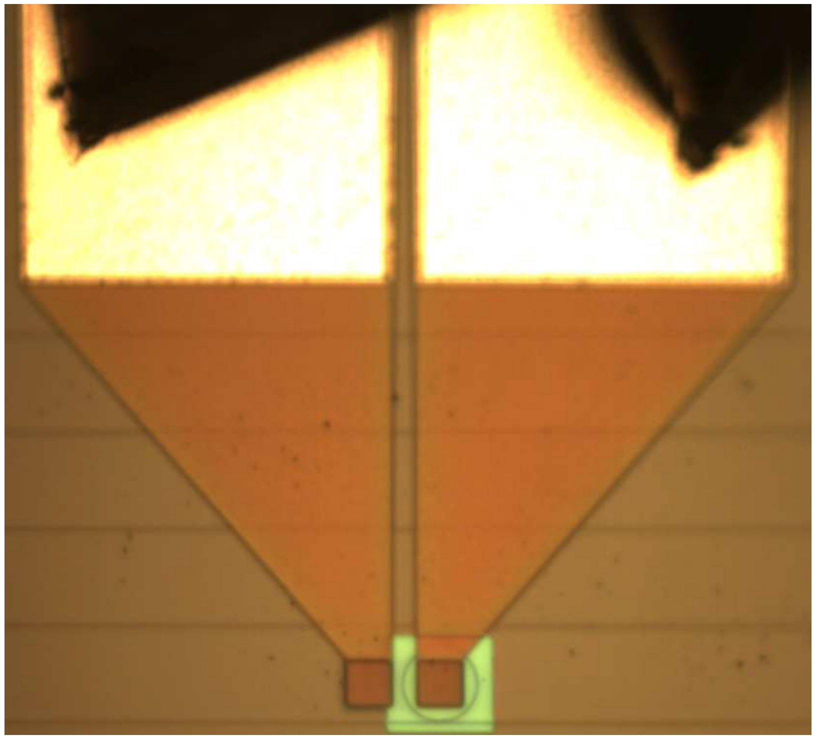

Figure 6.5: Microscope image of single-ring pn junction modulator. The metal contact pads are bright yellow, with dark metal probes landed on them. Where doping and the rib waveguide require the slab layer, the slab silicon layer appears green. Silicon waveguides and areas without the slab layer appear a darker brown/red. The dark red traces between the metal contacts and the ring are the high-speed modulation metal traces.

Characteristic	Value	Unit
Detector Material	InGaAs	
Rise Time/Fall Time	35/35	ps
Conversion Gain	1620 at 1310 nm	V/W
Bandwidth	0.02 - 10	GHz
Active Area Diameter	32	μm
Noise Equivalent Power (NEP)	30 at 1310 nm	$W/\sqrt{Hz}$
DC Monitor Output	1	V/mA
Maximum Linear Rating	450	mV$_{p-p}$
Output Connector	SMA	
Fiber Optic Connection	FC/UPC	

Table 6.1: EOT Amplified InGaAs Detector ET-3500AF (35-2135AF) performance characteristics. [135]

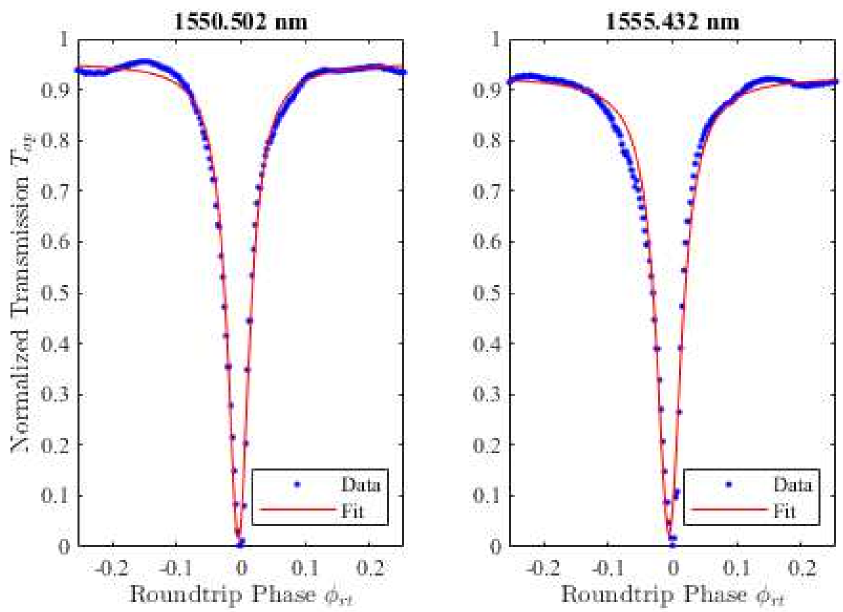

Figure 6.6: Resonance dip transmission spectra versus roundtrip phase ϕ_{rt} for single all-pass microring resonances at 1550.502 nm and 1555.432 nm. Experimental data plotted using blue dots with a fit function plotted in red. The transmission coefficients τ^2 were calculated to be 0.9742 and 0.9697, the roundtrip attenuation coefficients were calculated to be 0.9845 and 0.9840. The Q-factors were calculated to be 46,147 and 44,052, with optical bandwidths of 4.19 and 4.38 GHz and extinction of 27.4 dB and -25.8 dB.

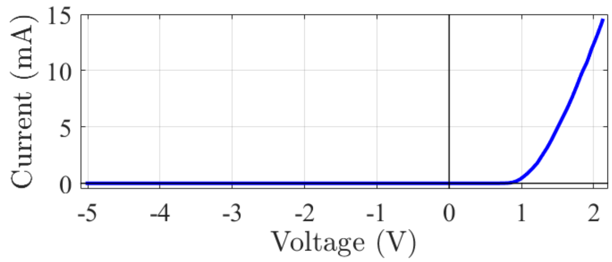

(a)

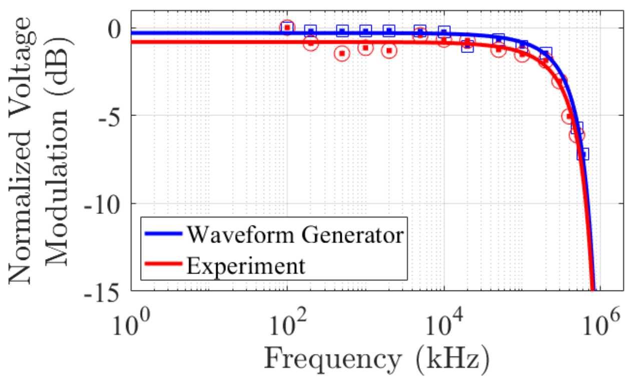

(b)

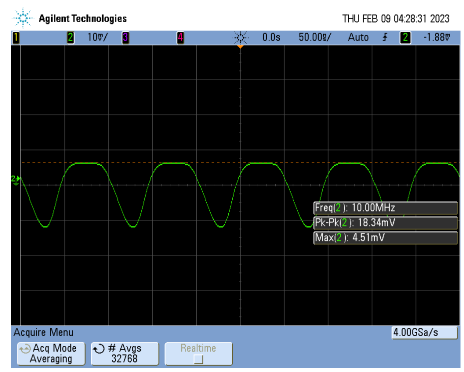

(c)

Figure 6.7: (a) Characteristic IV-curve of the pn junction implemented in the FDMR modulation TPI lattice. (b) Voltage modulation versus frequency of modulation for the all-pass microring resonator at 1550.502 nm using a pn junction. (c) Screenshot of a measured waveform sampled at 10 MHz modulation of the all-pass microring resonator at 1550.502 nm.

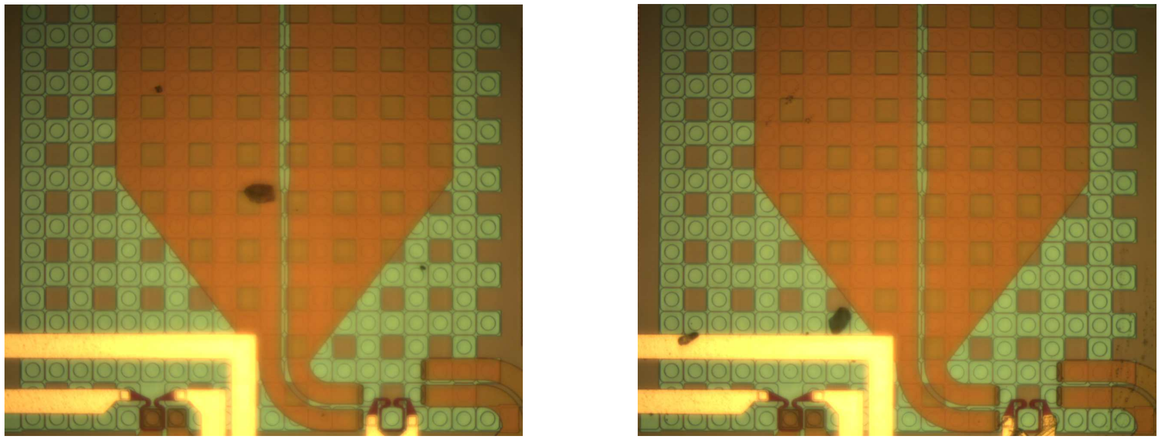

(a) (b)

Figure 6.8: Microscope images of the lattices used to explore FDMR modulation using (a) even pn junctions and (b) p-biased pn junctions. Their designs are identical apart from the thickness of the p-doped region of the junction. The defect rings are surrounded by metallic heating elements (darker purple colour). The metal traces are bright yellow and connect the heating elements to metal contact pads (not shown). Areas of the lattice with a slab silicon layer are green. Silicon waveguides and areas without the slab layer appear a darker brown/red. The imposing dark red fins exiting the top of the images are the high-speed modulation metal traces, which connect to the p and n sides of the pn junctions.

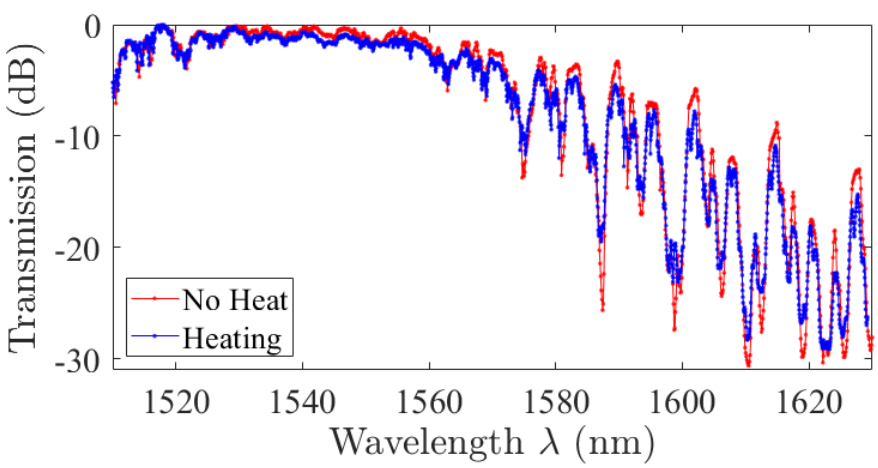

Figure 6.9: Transmission spectra of the even-biased TPI lattice with no heating applied to the defect ring in red, and significant heating current applied in blue. While transmission dips were introduced to the high-transmission edgemodes, their quality factor was not high enough to support high-speed modulation.

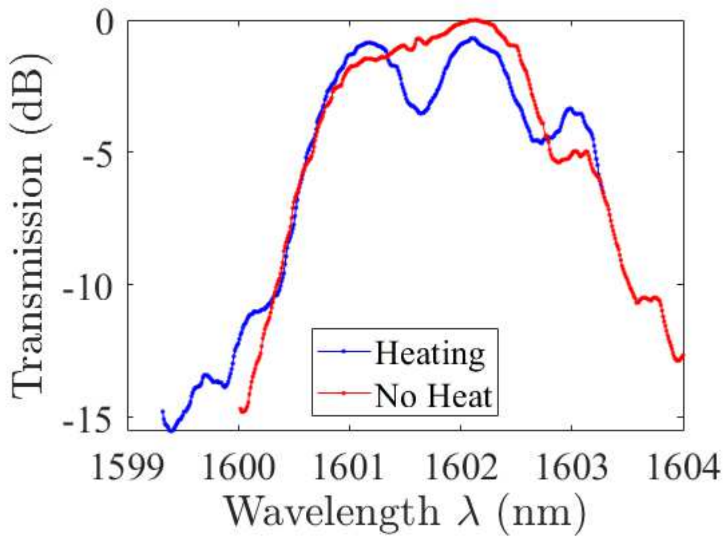

Figure 6.10: Transmission spectrum of a single flatband of the even-biased TPI lattice with no heating applied to the defect ring in red, and significant heating current applied in blue. While two transmission dips are clearly introduced, their maximum extinction is 2.84 dB.

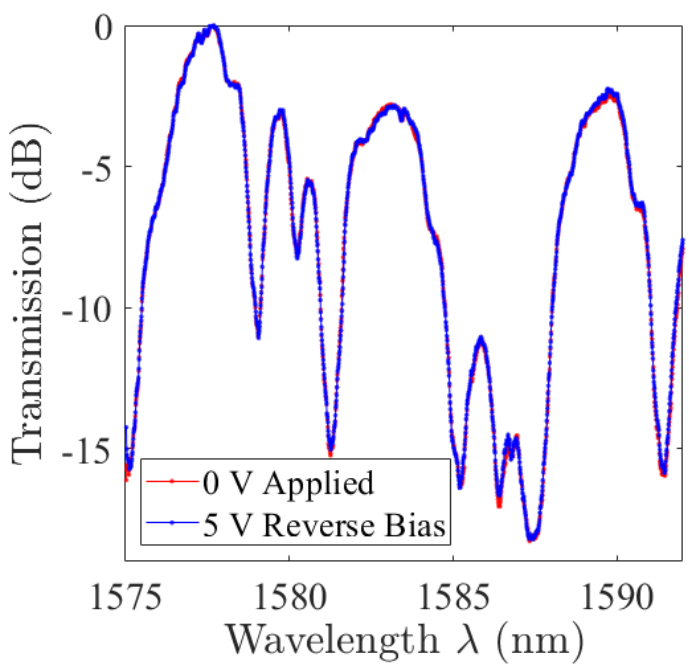

Figure 6.11: Transmission spectrum of 2 FSR of the even-biased TPI lattice with no bias voltage applied to the pn junction in red, and 5 V of reverse bias applied to the pn junction in blue. The pn junction on its own clearly has no effect on the transmission spectrum of the TPI lattice.

6.3.2 Floquet Defect Mode Resonance in Optical Routing

The lattice used to explore coupled FDMR and optical routing is pictured in Fig. 6.12. The lattice is 5 x 10 unit cells and contains 6 thermo-optic heating elements, representing an experimental realization of the schematic presented in Fig. 6.4. The experimental setup limited the number of metallic heaters that could be controlled at one time, so only the vertical path of 3 heaters, or 4 coupled FDMR, was experimentally explored. The overall transmission spectra of the lattice are presented in Fig. 6.13, with the drop ports at Out 1, Out 2, and Out 3 in bright red, dark red, and black, respectively, and the through port in blue. These spectra were recorded with no heating current applied to any heaters.

Using the Sensors Unlimited Inc. SU320M-1.7RT InGaAs NIR MiniCamera from Chapter 3, we were able to visualize the spatial localization of the light travelling through the lattice. With the wavelength tuned to a topologically non-trivial bandgap, the lattice supported an edgemode. When the first metallic heater applied a phase detune to the target ring along the bottom edge of the lattice, we were able to see a resonance localized within the first 3 microrings of the lattice and the edgemode intensity past the defect ring lessened, as shown in Fig. 6.14a. Adding heating current to the second metallic heater dimmed the edgemode even further and introduced light into FDMR 7 microrings deep into the bulk of the lattice, as shown in Fig. 6.14b. Finally, applying heating current to all three metallic heaters vertically allowed us to complete the 4-FDMR CROW structure across the lattice. As seen in Fig. 6.14c, no light passes through the edgemode of the lattice and light can now be seen scattering at the corners of resonators along the top edge of the lattice. While using the NIR camera to record scattered light from the lattice, we were also able to observe the heating of the metallic elements through their NIR emission, as shown in Fig. 6.15. In this image, from bottom to top, the heaters are experiencing 1.8 mA, 2.8 mA, and 3.8 mA of heating current applied.

We were able to measure transmission spectra out of the drop port at the top left of the lattice, marked by ”OUT 3” in the schematic in Fig. 6.4, for varying heating currents

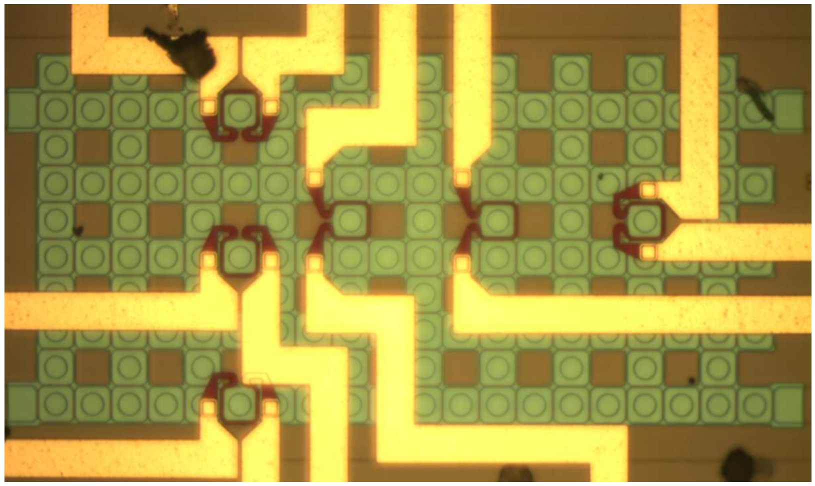

Figure 6.12: Microscope image of the lattice used to generate coupled FDMR to route signals across the lattice. The defect rings are surrounded by metallic heating elements (darker purple colour). The metal traces are bright yellow and connect the heating elements to metal contact pads (not shown). Areas of the lattice with a slab silicon layer are green. Silicon waveguides and areas without the slab layer appear a darker brown/red.

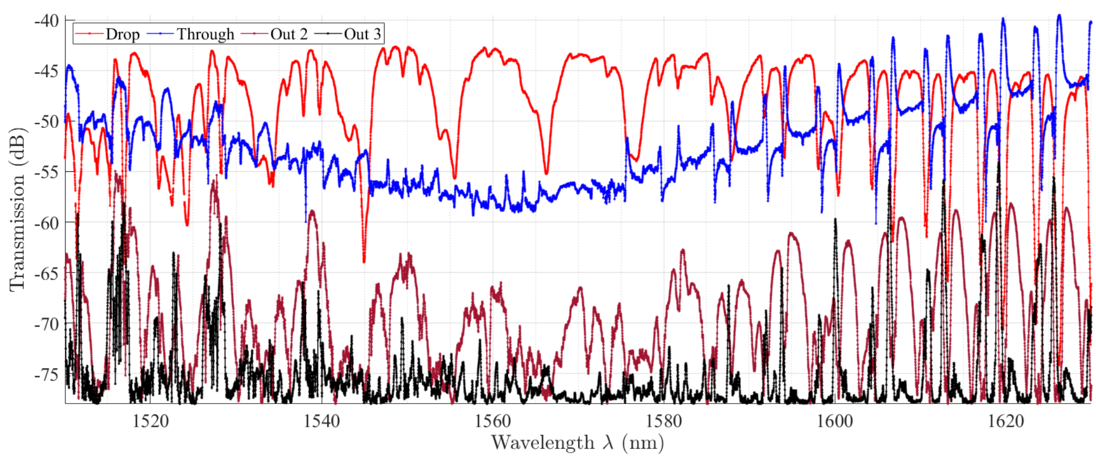

Figure 6.13: Transmission spectra of the routing lattice with no heating applied at the drop ports of Out 1 (red), Out 2 (dark red), and Out 3 (black), and the through port (blue).

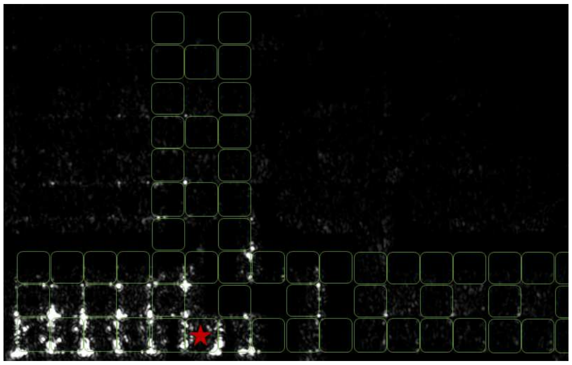

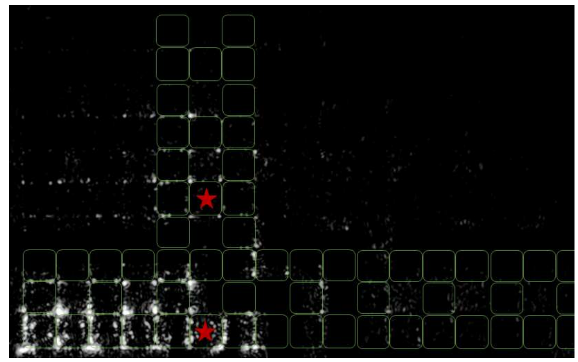

(a) (b)

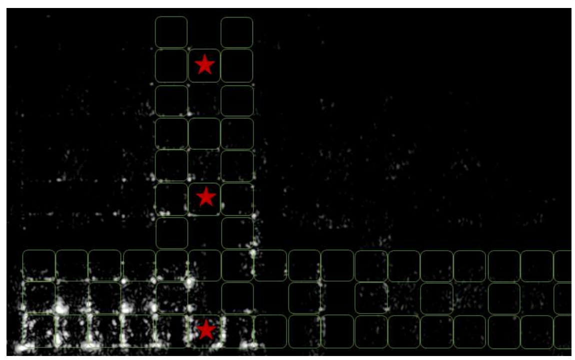

(c)

Figure 6.14: NIR images of the routing lattice at 1619.274 nm. A green schematic of the areas of interest of the TPI lattice is overlaid to guide the eye. Active defect rings are marked by red stars. (a) 1 FDMR is excited with 3.3 mA of heating current applied to the first metallic heater. Light is localized to the bottom edge of the lattice and the edgemode is dimmed past the defect ring. Light spreads as far as 3 microrings into the bulk at the FDMR location. (b) 3 FDMR are excited with 3.1 mA of heating current applied to the first heater and 2.8 mA applied to the second. Light is localized to the bottom edge of the lattice and the edgemode is even more dimmed past the FDMR location. The addition of the second heater has spread light as far as 7 microrings into the bulk of the lattice. (c) 4 FDMR are excited with 3.0 mA of heating current is applied to the first heater, 3.1 mA to the second, and 1.8 mA to the third. Light is localized to the bottom edge of the lattice, though no light in the edgemode passes the defect ring. The addition of the third heater has now allowed light to pass the entire way across the lattice, spanning 9 microrings vertically.

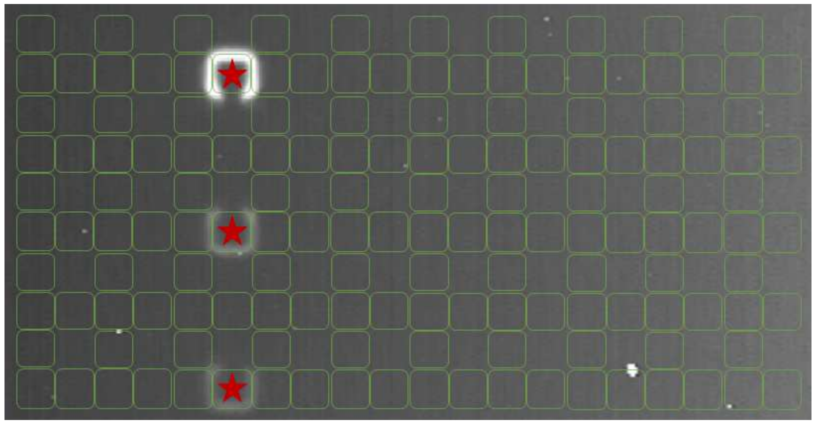

Figure 6.15: NIR image of three metallic heaters glowing as 1.8 mA, 2.8 mA, and 3.8 mA is applied to heaters 1, 2, and 3, respectively. A green schematic of the TPI lattice is overlaid on the NIR image to provide context. The defect rings are marked by red stars.

applied to the metallic heaters. Heaters 1 and 2 were previously aligned quantitatively by minimizing the transmission dip in the OUT 1 drop port and qualitatively by maximizing the brightness of the observed resonances in the NIR image, similar to Fig. 6.14b. 2.6 mA and 7.3 mA were applied to heaters 1 and 2. As pictured in Fig. 6.16, the final heater current was swept from 1.5 mA to 8.8 mA, effectively sweeping the resonant wavelength of that FDMR. The peak transmission was maximized to 3.45 dB above the noise floor when the resonant wavelength of the final FDMR was aligned with the previous 3, induced by the first 2 heaters. The total transmission loss at port OUT3, relative to the OUT1 drop port high-transmission was 36 dB.

In a second set of measurements, we were able to use the New Imaging Technologies WiDy SenS 640 V-ST NIR Camera to visualize the spatial localization of the light in the lattice. The performance characteristics of this camera are summarized in Table 6.2. The software used by this camera allowed for in-depth pre-processing which included bad pixel cancellation and on-the-fly cutoffs for maximum and minimum pixel intensities.

The transmission spectrum at the OUT 1 Drop port is shown in Fig. 6.17, with no heaters active in red and all heaters active in blue. The magenta dots mark wavelengths of interest at a bulk passband λ_1 (1618.022 nm), a transmission dip λ_2 (1619.280 nm), a high-transmission edgemode λ_3 (1620.200 nm), and another transmission dip λ_4 (1621.288 nm).

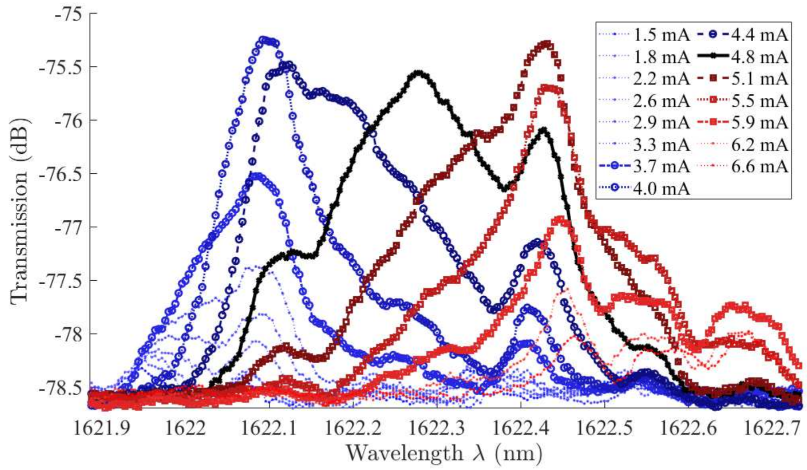

Figure 6.16: Transmission spectra at the OUT 3 port of the routing lattice at around 1622 nm versus heating current applied to the third heater. A maximum transmission peak of 3.45 dB above the noise floor was observed. Heaters 1 and 2 were previously aligned quantitatively by maximizing transmission dip in the OUT 1 drop port and qualitatively by maximizing the brightness of the observed resonances in the NIR image. 2.6 mA and 7.3 mA were applied to heaters 1 and 2. Heater 3 was swept from 1.5 mA to 6.6 mA.

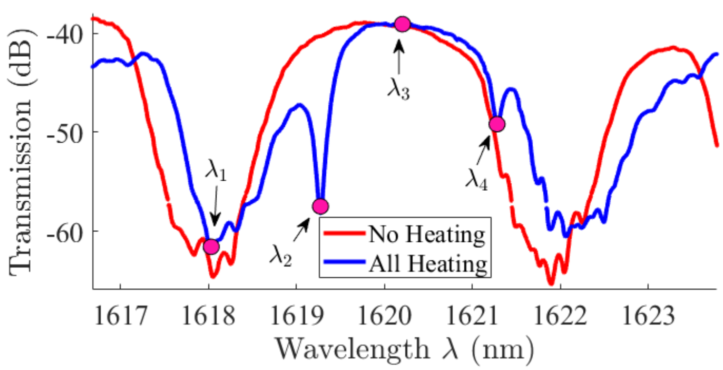

Figure 6.17: Transmission spectra at the OUT 1 Drop port of the routing lattice showing one FSR of the lattice between 1616 nm and 1623 nm with no heaters active (red) and all heaters active (blue). 2.6 mA, 2.4 mA, and 4.9 mA were applied to heaters 1, 2, and 3, respectively. The magenta dots mark wavelengths of interest at a bulk passband λ_1 (1618.022 nm), a transmission dip λ_2 (1619.280 nm), a high-transmission edgemode λ_3 (1620.200 nm), and another transmission dip λ_4 (1621.288 nm).

Characteristic	Value	Unit
Material	InGaAs	
Resolution	640 x 512	Pixels
Pixel Pitch	15	μm
Quantum Efficiency	$>$70	%
Frame Rate	Up to 230	FPS
Exposure Time	0.01 - 1000	ms
Spectral Range	900 - 1700	nm

Table 6.2: New Imaging Technologies WiDy SenS 640 V-ST NIR Camera performance characteristics. [136]

Looking first at the behaviour of the lattice in a bulk passband at λ_1, we can see in Fig. 6.18a that the transmission dips in the spectrum of the lattice correspond to light spreading out through the bulk from the input port. Additionally, we can see that while the spatial distribution changes with heat applied in Fig. 6.18b, the light is still spread throughout the lattice in a way that reduces transmission, as seen in the transmission spectrum in Fig. 6.17.

Next, looking at the behaviour of the lattice in a edgemode in the bandgap of the lattice at λ_3, we can see in Fig. 6.19a that the high and flat transmission corresponds to light being localized along the bottom edge of the lattice. Additionally, we can see in Fig. 6.19b that adding heating current to all three heaters does not change the behaviour of the edgemode.

Now we can investigate the implementation of the 4 FDMR CROW structure at λ_2. Figure 6.20a shows that with no heating current applied, the edgemode is present along the bottom edge of the lattice. This corresponds with the high transmission at this wavelength in Fig. 6.17 in red, with no heating applied. However, once we apply current to all three metallic heaters, we align their resonances at this wavelength and see light cross the lattice in Fig. 6.20b. Additionally, we see that the light at the bottom right of the lattice, previously travelling through the edgemode, is no longer making it past the defect ring at the bottom of the lattice.

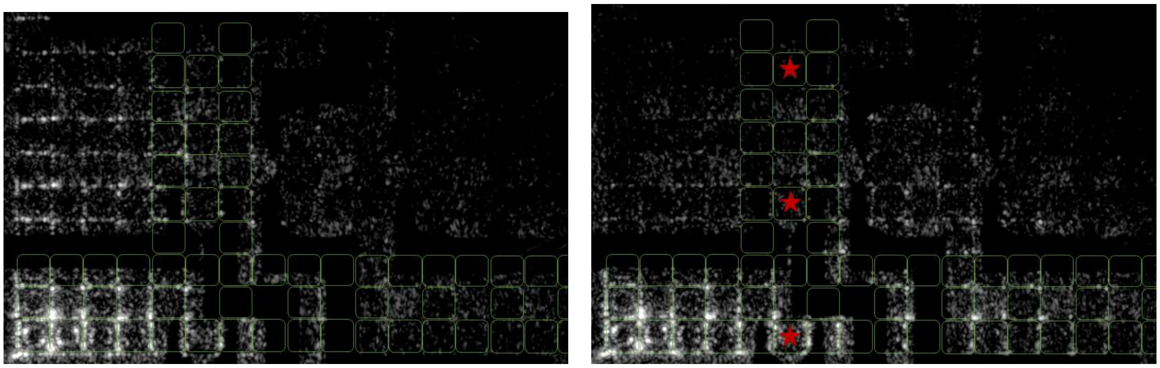

(a) (b)

Figure 6.18: NIR images of a bulk mode in the routing lattice with 10 mW of input optical power at λ_1. A green schematic of the areas of interest of the TPI lattice is overlaid to guide the eye. Active defect rings are marked by red stars. (a) With no heating current applied to any metallic heater. Light spreads into the bulk of the lattice from the input port. (b) With 2.6 mA of heating current is applied to the first heater, 2.4 mA to the second, and 4.9 mA to the third. Light again spreads through the bulk of the lattice, though the spatial localization has changed. It is clear that this is not an edgemode as the light intensity quickly diminishes along the bottom of the lattice.

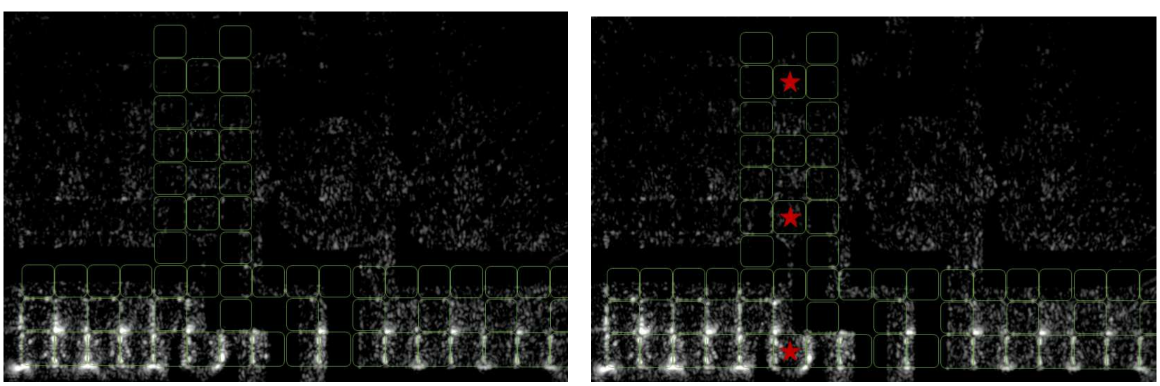

(a) (b)

Figure 6.19: NIR image of an edgemode in the routing lattice with 10 mW of input optical power at λ_3. A green schematic of the areas of interest of the TPI lattice is overlaid to guide the eye. Active defect rings are marked by red stars. (a) With no heating current applied to any metallic heater. Light is localized within the first unit cell along the bottom edge of the lattice. (b) With 2.6 mA of heating current is applied to the first heater, 2.4 mA to the second, and 4.9 mA to the third. Light again is localized within the first unit cell along the bottom edge of the lattice.

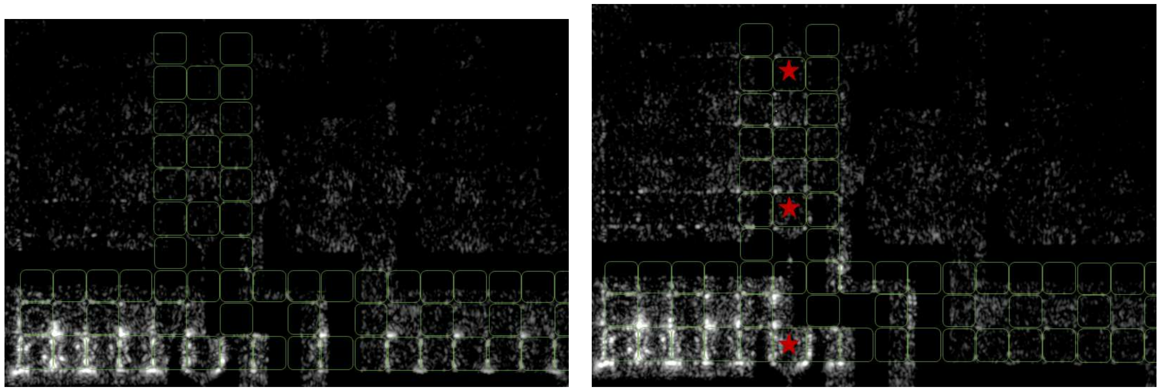

(a) (b)

Figure 6.20: NIR image of the lattice probed at λ_2. A green schematic of the areas of interest of the TPI lattice is overlaid to guide the eye. Active defect rings are marked by red stars. (a) With no heating current applied to any metallic heater. An edgemode is present, light is localized within the first unit cell along the bottom edge of the lattice. (b) With 2.9 mA of heating current is applied to the first heater, 3.0 mA to the second, and 1.9 mA to the third. 4 FDMR are excited, with light now routed vertically, scattering 9 microrings deep across the bulk of the lattice.

One final set of measurements investigated both the 4 FDMR structure at λ_2 and λ_4. This wavelength gap represents the FSR of a single FDMR, about 2.01 nm, which is about a third of the TPI lattice FSR of about 6.42 nm at these wavelengths. Figures 6.21a and 6.21c again demonstrate the spatial localization of the edgemode which supports high transmission through the lattice. These images are taken without heating applied to the defect rings. Once heating is applied, Figs. 6.21b and 6.21d show the absence of light in the second half of the edgemode, instead routed vertically across the lattice. Furthermore, comparing these two figures demonstrates the spatial localization difference corresponding to the difference in transmission dip in the spectrum of Fig. 6.17 at these two wavelengths.

6.4 Conclusions

For the active modulation of signals, the induced FDMR produced a resonance dip that was too shallow to effectively support high-speed modulation. It was also observed that the pn junction on its own was unable to generate a large enough change in the effective refractive index to induce the FDMR. However, this issue appears to be limited to the combination

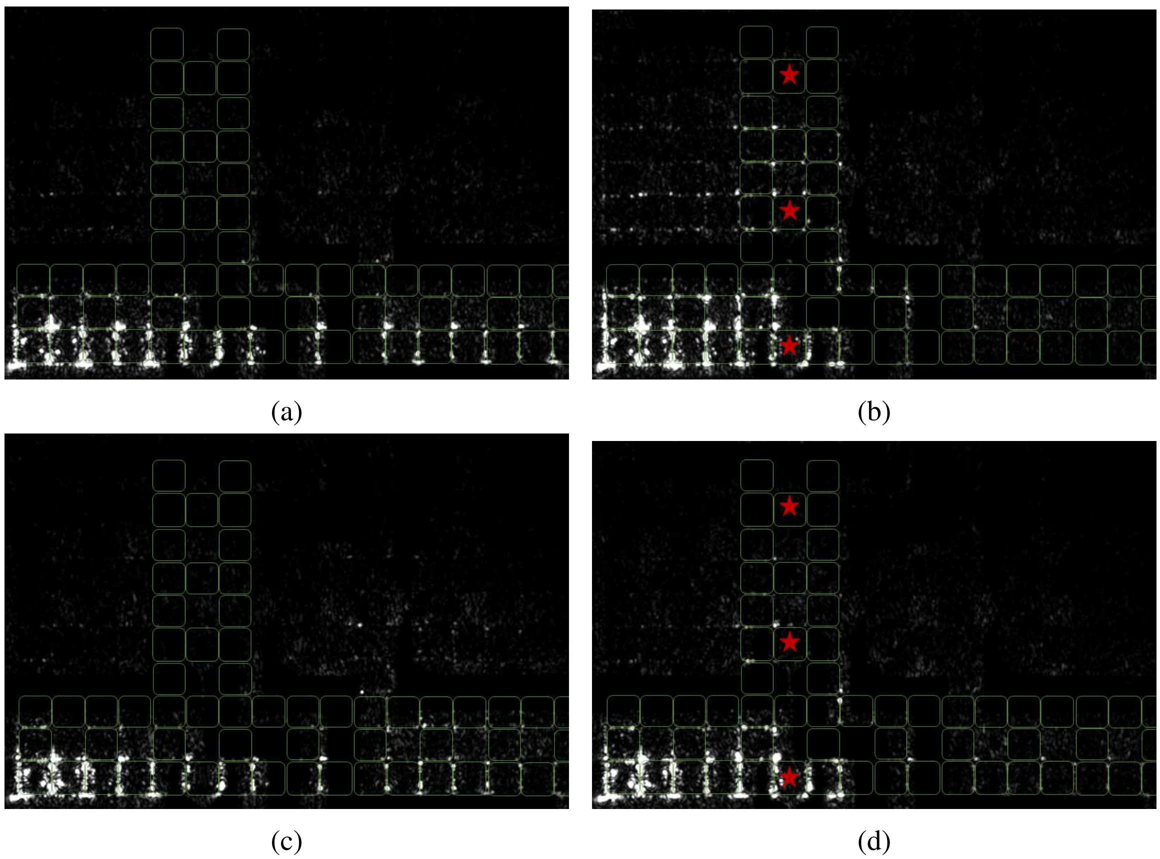

Figure 6.21: NIR images of the routing lattice with 0.03 mW of input optical power at (a-b) λ_2 and at (c-d) λ_4 (a,c) An edgemode, with no heating current applied to any metallic heater. Light is localized within the first unit cell along the bottom edge of the lattice. (b,d) 4 excited FDMR with heating current applied to the first, second, and third metallic heater. The light has now been routed vertically, with light scattering 9 microrings deep across the bulk of the lattice.

of doped-silicon on the TPI lattice, as the pn junction functioned as intended on a single APMR, and the TPI lattice supported significant FDMR when only the metallic heater was present.

This lack of signal modulation performance may have been due to high loss in the defect ring due to the doping levels of the silicon. Alternatively, the doping may have changed the coupling coefficient between the defect ring and the neighbouring rings. As the doping was present across the coupling junctions, the coupling coefficient could have been very different from what was designed. This could have resulted in the coupling between the FDMR mode and the edge mode being too weak or too strong, producing a broad resonance.

For the routing of signals across the TPI lattice using coupled FDMR, the level of transmission was low. While light did make it across to the opposite output port of the lattice, the transmission peak was quite small. This may be a case of changing many design parameters at once, as the 5 nm bending radius had previously been implemented on a slab waveguide SOI device, but perhaps this bending radius was too tight for a RIB waveguide. It is also possible that light in any of the coupled FDMR reflected into counter-propagating modes in the FDMR, coupling back into a counter-propagating edgemode. The loss in the effective CROW system may also be quite significant, reducing the amount of optical power that can be routed across the lattice.

For both the modulation and routing TPI lattices, the passbands are very broad when compared to similar lattices in our previous work. This is likely due to the lack of random variation in the lattice microrings as these devices were fabricated at AMF, while previous devices were fabricated by ANT. Future work on active applications of FDMR in TPI lattices should investigate the impacts of advanced fabrication elements such as localized doped silicon on the TPI, edgemode, and FDMR characteristics, as well as the impacts of localized loss and coupling changes on the ability for light to couple from the topologically-protected edgemode to the induced FDMR.

Chapter 7

Generation of Hofstadter's Butterfly Spectrum Using Circular Arrays of Microring Resonators

In each of the previous chapters, we investigated two-dimensional topological photonic insulators, which are periodic in two spatial dimensions. Recently, there has also been interest in exploring TPIs with synthetic dimensions, such as one-dimensional coupled waveguide arrays with the mode spectrum serving as the second dimension [137] or one-dimensional microring arrays [138, 139] with a periodic frequency spectrum serving as the second dimension. By reducing the spatial dimensions of a 2D TPI from two to one, these devices can be greatly reduced in size compared to 2D lattices. In this chapter, we explore a 2D topological microring system with a synthetic dimension formed by the periodic variation of the microring resonance frequency. We propose a simple topological photonic structure based on a circular array of microrings with periodic resonant frequency detunings, generating a 2-dimensional lattice where the synthetic dimension is the roundtrip phase variation. This lattice can be implemented on an integrated optics platform. We show that this ring-of-rings structure exactly emulates the Harper equation and propose an experimental approach for measuring Hofstadter's butterfly spectrum at optical frequencies. Hofstadter's butterfly spectrum, which characterizes the energy bands of electrons in a two-dimensional lattice under a perpendicular magnetic field, has been emulated and experimentally characterized in periodic bandgap structures at microwave and acoustic frequencies. However, measurement of the complete spectrum at optical frequencies has yet to be demonstrated.

7.1 Introduction

Here, we propose a topological photonic system based on a circular array of microring resonators which can be used to measure the Hofstadter spectrum. This spectrum describes the energy bands of electrons in a two-dimensional periodic lattice with a perpendicular magnetic field [140, 141], which forms a topological system that eventually led to the discovery of the quantum Hall effect. Hofstadter explored the relationship between the periodicity of this lattice and the allowed energy states of the electrons in this arrangement, leading to the well-known butterfly spectrum. In a recent work, Hafezi *et al.* proposed a two-dimensional microring resonator lattice with a coupling phase gradient imposed on it to emulate a synthetic gauge potential [7]. This synthetic gauge field forms the basis of the 2D TPI behaviour of that lattice. It was shown that Bloch modes in the lattice satisfy the Harper equation exactly and the Hofstadter spectrum can be generated from the reflection spectra. Hafezi *et al.* has since demonstrated a 2D topological system capable of sampling a single flux value α per device [8]. This design was then followed by Kudyshev *et al.* with a theoretical proposal for a 2D topological lattice with tunable α values [142]. Despite these works, the Hofstadter spectrum has not yet been measured in its entirety at optical frequencies due to the complexity of the proposed structures and the lack of practical methods to vary the periodic potential and measure the eigenfrequency spectra. Furthermore, the recent experimental devices and proposed geometries are purposely finite, with topologically protected edge states present in the bandgaps of the energy spectrum.

The proposed ring-of-rings (ROR) structure emulates an infinite 1D microring lattice with a periodicity equal to the ring circumference. We show that by varying the resonant frequencies of the microring resonators, we can emulate the Harper equation exactly. We also suggest a method for experimentally obtaining the Hofstadter butterfly spectrum by coupling a straight waveguide to the ROR structure. By measuring the through-port spectrum of the device, we show that it is possible to obtain the eigenfrequencies of the Harper equation and generate the Hofstadter spectrum experimentally.

7.2 Theoretical Background

We first show that an infinite, one-dimensional array of microring resonators can exactly emulate Harper's equation. We consider an infinite chain of coupled microring resonators as pictured in Fig. 7.1a. Each ring m is coupled to its neighbours by a constant coupling coefficient μ and detuned from some reference frequency ω_o by δ_m. Using the energy coupling model for coupled resonators [143], we can write the equation of motion for microresonator m as

$$i\frac{da_m}{dt} = (\omega_o + \delta_m)a_m - \mu a_{m-1} - \mu a_{m+1} \tag{7.1}$$

Assuming a time dependence of $e^{-i\omega t}$, we obtain the following eigenvalue equation,

$$a_{m+1} + a_{m-1} - \frac{\delta_m}{\mu}a_m = (\frac{\omega_o - \omega}{\mu})a_m \tag{7.2}$$

To match the above equation with the Harper equation [144],

$$\psi_{m-1} + \psi_{m+1} + 2\cos(2\pi m\alpha + k_y)\psi_m = \varepsilon\psi_m \tag{7.3}$$

we choose $\delta_m = \Delta\omega\cos(2\pi m\alpha + k_y)$ and identify $\varepsilon = \frac{\omega_o - \omega}{\mu}$. The frequency detuning profile of the microring chain is thus periodic with period $1/\alpha$, where $\alpha = \frac{q}{N}$ is a rational number with q and N being integers and $q \leq N$. In the original problem of electrons in a 2D lattice, k_y accounts for all values of Bloch mode wave numbers in the y-direction. In our 1D microring lattice, k_y can be realized simply by a phase shift in the periodic frequency detuning profile, serving as a synthetic dimension.

Since the sequence of frequency detunings δ_m is periodic with period N/q, from a practical implementation point of view, we can replace the infinite microring chain by a ring of N microrings, as shown in Fig. 7.1b (omitting the input waveguide). The number of

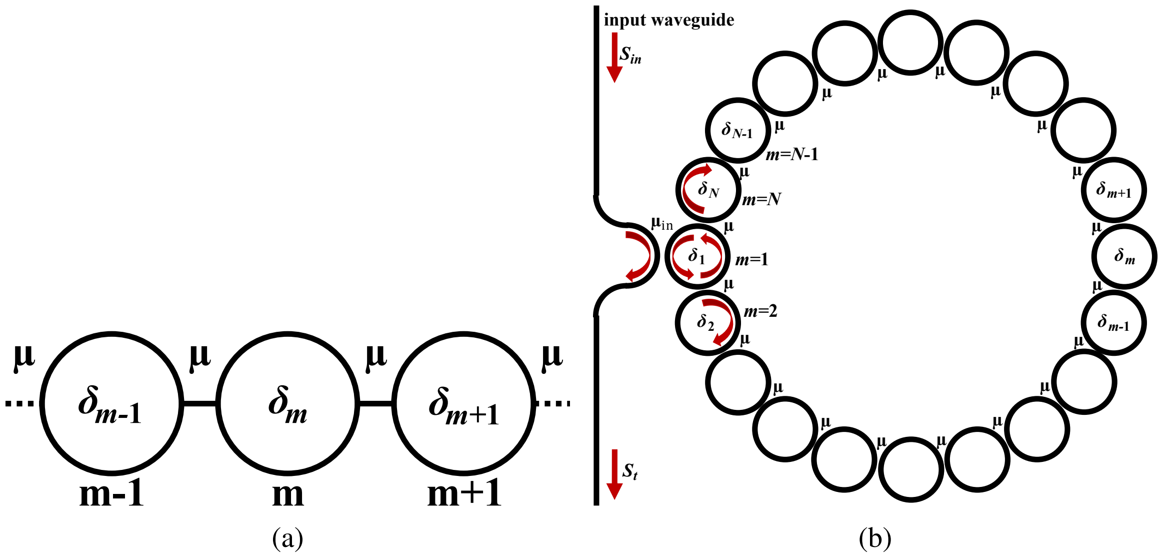

Figure 7.1: Schematic of **(a)** an infinite 1D chain of microring resonators and **(b)** a ring of N microring resonators for emulating an infinite periodic chain of coupled microrings. Each microring has a resonance detuning of δ_m and identical coupling coefficients μ to its neighbours. The input waveguide coupled to microring 1 via coupling coefficient μ_{in} is used to excite Bloch modes in the array. Adapted from [145].

microrings N is assumed to be even so that each microring supports only a clockwise or counterclockwise mode. We label the microrings $m = 1, 2, \ldots, N$, with ring 1 coupled back to ring N. The ROR structure supports Bloch modes of the form $a_m = u_m e^{ik_x m}$, where k_x represents the propagation constant along the chain and we have assumed a lattice spacing of 1. The mode amplitude u_m has the same periodicity of the ROR structure with periodic boundary condition, $u_{m+N} = u_m$, from which we obtain the Floquet boundary condition for a_m: $a_{m+N} = a_m e^{ik_x N}$. Using this boundary condition to write $a_{N+1} = a_1 e^{ik_x N}$ and $a_0 = a_N e^{-ik_x N}$, we obtain the eigenvalue matrix equation for the Bloch modes of the ROR structure:

$$
\begin{vmatrix}
-\Delta_1 & 1 & 0 & \cdots & e^{-ik_xN} \\
1 & -\Delta_2 & 1 & 0 & \vdots \\
\vdots & \ddots & \ddots & \ddots & \vdots \\
\vdots & 0 & 1 & -\Delta_{N-1} & 1 \\
e^{ik_xN} & \cdots & 0 & 1 & -\Delta_N
\end{vmatrix}
\begin{vmatrix}
a_1 \\ a_2 \\ \vdots \\ a_{N-1} \\ a_N
\end{vmatrix}
= \varepsilon
\begin{vmatrix}
a_1 \\ a_2 \\ \vdots \\ a_{N-1} \\ a_N
\end{vmatrix}
\tag{7.4}
$$

where $\Delta_m = \Delta\cos(2\pi m\alpha + k_y)$ and $\Delta = \frac{\Delta\omega}{\mu}$.

For a given α value, solving the matrix Eq. 7.4 provides N eigenvalues ε, which correspond to the eigenfrequencies of the ROR structure. These eigenvalues are periodic functions of the propagation constants k_x and k_y. By sweeping k_x and k_y from 0 to 2π, the eigenfrequencies merge to form distinct, continuous bands which correspond to the transmission bands of the microring chain at the given α value. The entire Hofstadter spectrum is obtained by plotting the transmission bands for fractional values of α between 0 and 1. Figure 7.2 shows the spectrum obtained for ROR structures with N ranged from 2 to 49 and q swept from 0 to N. The result is similar to the butterfly pattern originally obtained by Hofstadter [141].

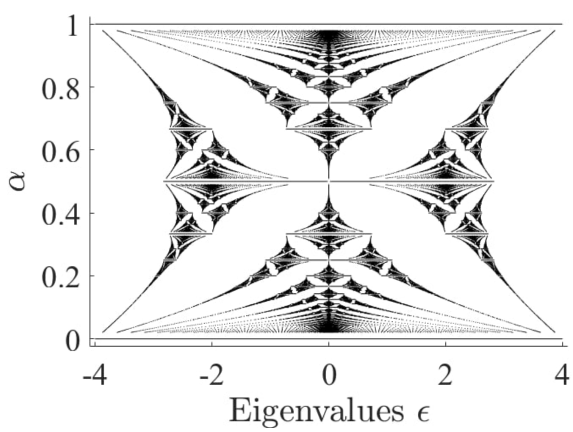

Figure 7.2: Plot of the α parameter versus eigenvalue ε for ROR devices with $N < 50$. The spectrum exactly replicates the well-known Hofstadter butterfly.

7.3 Experimental Proposal and Simulated Results

The ROR structure can be implemented on an integrated optics material platform such as silicon-on-insulator (SOI). The resonant frequency detunings can be achieved by thermo-optic tuning of individual microrings using microheaters fabricated on top of the resonators. For example, heating elements on SOI microrings can tune the resonant frequency over a full free spectral range of the microring [146]. For a fixed number of microrings N in the ROR, discrete values of $\alpha = q/N$, for $q = 0, 1, ...N$, as well as a continuous range of k_y values between 0 and 2π, can be realized by adjusting the currents through the heaters. In order to excite the lattice and measure its eigenfrequency spectrum, a straight waveguide weakly coupled to microring 1, as pictured in Fig. 7.1b, is used to excite the k_x spectrum of Bloch modes. Specifically, at a fixed k_y value and excitation frequency ω inside an allowable energy band of the lattice, the input light with amplitude S_{in} excites a discrete spectrum of Bloch modes in microring 1 with amplitudes $a_1[i] = i\kappa_i S_{in}$, $i = 1$ to M, where M is the number of supported Bloch modes and κ_i is the amplitude coupling coefficient of the input light to Bloch mode i. Each Bloch mode i then propagates around the ROR with propagation constant $k_x[i]$, so that after one complete roundtrip, the mode amplitude $a_1[i]$ in microring 1 satisfies the relation

$$a_1[i] = i\kappa_i S_{in} + \alpha_i \tau_i a_1[i] e^{ik_x[i]N} \tag{7.5}$$

where $\tau_i = \sqrt{1-\kappa_i^2}$ and α_i represents the roundtrip amplitude attenuation of mode i due to waveguide loss. At the waveguide output, the transmitted light consists of a superposition of amplitudes $s_t[i]$, each due to Bloch mode i, equal to

$$s_t[i] = \tau_i S_{in} + i\kappa_i \alpha_i a_1[i] e^{ik_x[i]N} \tag{7.6}$$

By solving for $a_1[i]$ from Eq. 7.5 and substituting the result into Eq. 7.6, we obtain

$$s_t[i] = \frac{\tau_i - \alpha_i e^{ik_x[i]N}}{1 - \alpha_i \tau_i e^{ik_x[i]N}} S_{in} \tag{7.7}$$

The amplitude of mode i is minimized at resonant frequencies satisfying the condition $k_x[i]N = m(2\pi)$, where m is an integer. The total transmitted power at the waveguide output is given by

$$P_t = P_{in} \sum_{i=1}^{M} \left| \frac{\tau_i - \alpha_i e^{ik_x[i]N}}{1 - \alpha_i \tau_i e^{ik_x[i]N}} \right|^2 \tag{7.8}$$

where $P_{in} = |S_{in}|^2$ is the input power. For large N, the terms in the summation either have small amplitudes due to resonance or they do not coherently add up because of the random phases. As a result, the power transmission P_t/P_{in} will be small for frequencies inside an allowable energy band. On the other hand, for frequencies outside the allowable energy bands, no Bloch modes are excited in the ROR structure, so all the input power will be transmitted to the output. Thus, we can identify the energy bands of the microring lattice by the low-transmission frequencies in the power spectrum measured at the waveguide output, and the bandgaps by the frequencies at which the transmission is high. In this manner, the entire Hofstadter spectrum can be acquired by sweeping α and k_y parameters through thermo-optic tuning of the microrings and measuring the through-port spectra of the device.

We simulated the response of a realistic $N = 20$ ROR device at a reference wavelength of 1550 nm with propagation loss of 3 dB/cm, coupling coefficient $\mu = 150$ GHz, maximum resonant frequency detuning $\Delta\omega = 2\mu$, input waveguide power coupling of $\kappa_{in}^2 = 4.8\%$ and a microring finesse of 60. These coupling values were chosen as they provided the deepest transmission minima while also spreading the spectra appropriately in frequency so that the dips could be easily identified. Figure 7.3 plots the through-port frequency response of the ROR structure for different values of α in blue. For each α value, k_y is varied from 0 to 2π to fully cover the energy bands. The regions of flat-band transmission near

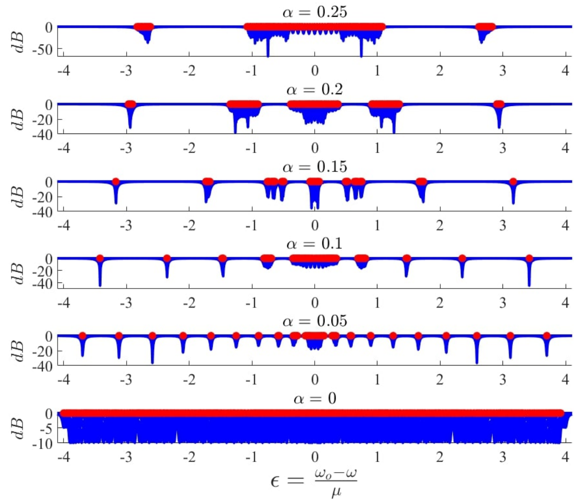

Figure 7.3: Blue traces show the through-port transmission spectra of an ROR with $N = 20$ microrings, with k_y swept from 0 to 2π, probed at α values from 0 to 0.25. The red dots mark the discrete eigenfrequencies of an infinite periodic microring lattice.

0 dB correspond to the bandgaps of the microring lattice. In between these bandgaps are regions of low transmission, which are identified as the allowable energy bands. The exact eigenfrequencies ε of the infinite periodic lattice are shown by the red dots, which match with the frequencies where the through-port transmission of the ROR is low. By sweeping $\alpha = q/N$ for $q = 0, 1, 2, ...N$ and marking the minimum of the transmission dips for each α value with black dots, we generate the Hofstadter spectrum shown in Fig. 7.4a. The result is seen to match the overall theoretical spectrum in Fig. 7.2, although with less detail in the vertical direction due to the small number of discrete values of α available for $N = 20$ microrings. More detail is revealed if we increase the number of microrings to $N = 50$, as shown by the spectrum in Fig. 7.4b.

In a realistic device, fabrication errors inevitably introduce variations in the coupling coefficients between the microrings, which may blur the spectrum features. We explored the effect of disorder in the lattice in the form of coupling variations as well as errors in setting the frequency detunings for the same $N = 20$ ROR device above. We imposed a random variation of ±10% in both the coupling coefficients μ between the microrings and the thermo-optically controlled resonant frequency detunings δ_m. We note that for $\mu = 150$ GHz and SOI microring radius $R = 11.27\mu m$, the coupling gaps are $\backsim$ 285 nm. A ±10%

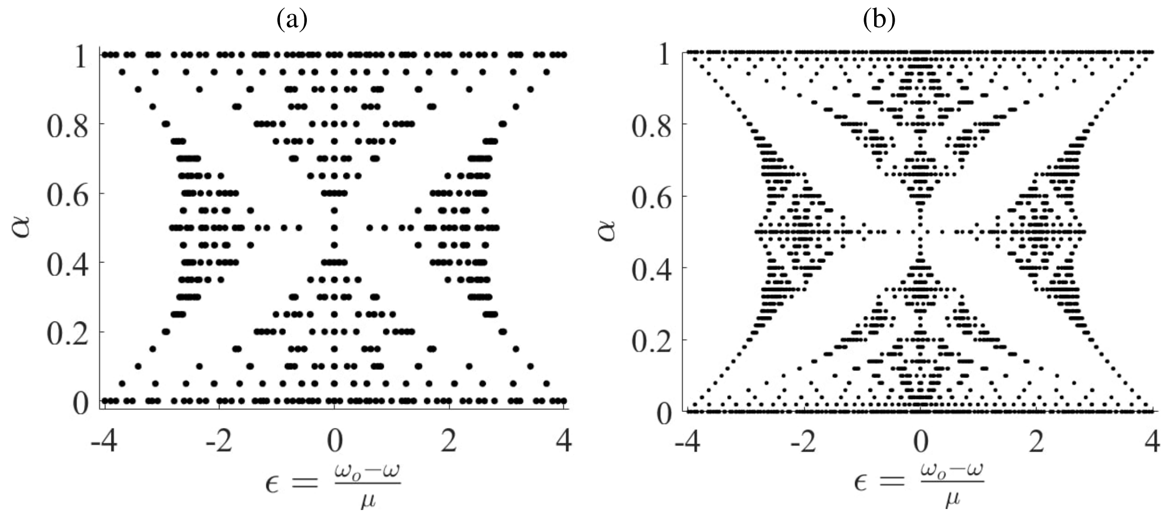

Figure 7.4: Black dots mark transmission dips of the through-port spectra of an ROR with **(a)** $N = 20$ and **(b)** $N = 50$ microrings, with k_y swept from 0 to 2π, probed at α values from 0 to 1.

variation in μ thus corresponds to a fabrication error of ±28nm in the coupling gaps, which is well within the capabilities of electron beam lithography. We performed 50 simulations with uniformly distributed coupling and resonant frequency variations. As shown in Fig. 7.5, the grayscale dots represent the probability of identifying the eigenfrequencies from the transmission dips in the through-port spectra. It is seen that the measured eigenfrequencies are centered on and distributed around the exact values shown by the red circles. The result demonstrates the accuracy with which a realistic ROR device with $N = 20$ microrings can replicate the ideal butterfly spectrum in the presence of lattice disorder. The structure is therefore robust to manufacturing and implementation errors and our proposed experiment provides a practical method for measuring the Hofstadter's butterfly at optical frequencies. We have designed and fabricated realistic test structures to explore these results experimentally in the future. The details can be found in Appendix A.

7.4 Conclusions

In summary, we proposed a ROR structure with periodic resonant frequency detunings for emulating Harper's equation and experimentally obtaining the Hofstadter butterfly spec-

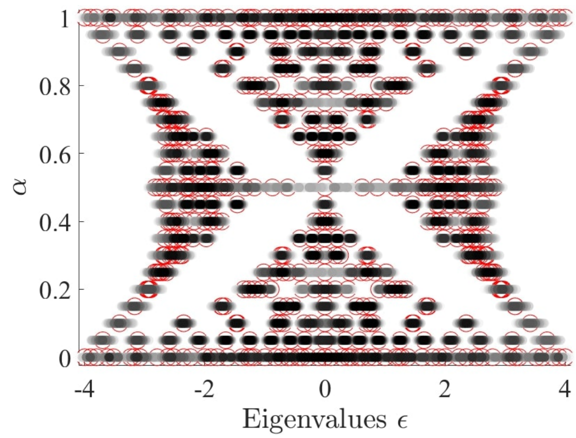

Figure 7.5: Hofstadter spectrum of a realistic $N = 20$ ROR device with uniformly distributed random variations in the coupling coefficient and resonant frequency detunings. The grayscale dots represent the probability of identifying the eigenfrequencies of the microring lattice over 50 simulated spectra. The red circles indicate the exact eigenfrequencies of an infinite chain of microrings.

trum at optical frequencies. The structure can be implemented on an integrated optics platform using heaters to control the frequency detuning of each microring, which allows the detune periodicity α to be varied discretely and the effective magnetic field k_y to be swept continuously. An input waveguide coupled to one of the microrings is used to excite the full k_x spectrum of Bloch modes in the lattice. The periodic roundtrip phase profile emulates the synthetic gauge field that can lead to nontrivial topological photonic behaviour. The proposed ROR structure provides a robust platform for experimental investigation of various aspects of the complex Hofstadter spectrum at optical frequencies, as well as the topological properties of circular and 2D periodic photonic lattices with synthetic dimensions. [145]

Chapter 8

Conclusions & Future Work

Through the research contained in this thesis, I have made many contributions to the collection of knowledge regarding Floquet defect mode resonance (FDMR) and its applications in nonlinear, quantum, and active topological silicon photonics. I assisted with the device design and simulation of the first experimental demonstration of anomalous Floquet insulator (AFI) on a nanophotonic platform in Chapter 3. This lattice provided a versatile foundation for investigating 2D Floquet topological photonic insulators (TPIs) and formed the basis for the realization of AFI and FDMR in future research. In pursuit of nonlinear photonics applications, I employed FDMR in a 2D silicon Floquet TPI lattice to demonstrate resonance-enhanced frequency generation through stimulated four-wave mixing (FWM) on a topological platform in Chapter 4. This work could support robust light sources generated directly on topologically-protected photonic platforms. Furthermore, this work directly lead to my experimental demonstration of resonance-enhanced entangled photon pair generation through the use of FDMR coupled to topologically-protected edge modes in a TPI lattice in Chapter 5. In pursuit of active photonics applications, Chapter 6 explored modulation of FDMR using pn junctions, finding that doped silicon affected the coupling between the FDMR and topologically-protected edge mode such that high-Q resonances could not be formed. My experimental demonstration of signal routing through coupled FDMR was more successful, with a CROW-like structure of 4 FDMR routing light across a TPI lattice. Finally, Chapter 7 proposed a 2D topological photonic system with a synthetic dimension in the roundtrip phase variation of the microring resonator lattice sites. In Appendix A, I also designed and fabricated an experimentally-realizable device to explore such systems in the optical frequency regime.

8.1 Conclusions

My research has contributed to the understanding of TPIs, anomalous Floquet TPIs, and the resonant phenomenon of FDMR that can be supported on this platform. This work supports the conclusion that TPIs can provide a material platform which supports robust photonic devices, tolerant to device parameter variation at the lattice level. Additionally, FDMR can be generated and utilized on a silicon TPI, leading to the development of these robust photonic integrated circuits. This work investigated TPIs and identified their potential applications, specifically exploring AFIs and FDMR. The spectral characteristics and phase-defect-dependence of FDMR was evaluated alongside its role in enabling defect-resistant integrated silicon photonic devices. The design, fabrication, simulation, and experimental demonstration of high-quality FDMRs allowed for the exploration of the advantages and challenges in frequency generation, entangled photon-pair generation, optical modulation, and routing on a topological photonic platform. This work has furthered the suitability of TPIs in addressing the problems that device imperfections, fabrication defects, and fluctuating operating environments pose to silicon photonic circuits. Furthermore, it has expanded the possible device applications of TPIs through demonstration of high-quality resonances on a topological platform. This work has also explored the nonlinear, quantum, and active photonics applications of FDMR, demonstrated through stimulated and spontaneous four-wave mixing, and the routing and modulation of optical signals. Overall, this work contributes to the development and application of TPIs and FDMR in integrated silicon photonics.

8.2 Future Work

The Floquet TPI lattices presented in this thesis provide a valuable platform for exploring novel applications of topologically-protected photonic integrated circuits. The novel FDMR, tuned to the center of a TPI topologically-nontrivial bandgap, combined with the inherent low-loss, defect-resistant edgemode of the TPI, resulted in a topologically protected waveguide-resonator system capable of efficient FWM. This system has potential applications in all-optical wavelength conversion, parametric amplification, entangled photon pair generation, and nonlinear signal processing. One particular example where the robustness of topologically protected edgemodes could have the most impact is in quantum photonic applications, which rely on single photon and entangled photon states that are susceptible to decoherence by device imperfections. Our FDMR can serve as a compact and efficient emitter of single photons that are directly coupled to the edgemodes for robust device operations. Combined with the topological protection of the Floquet edge modes, this photonic system could provide a robust topological photonic platform for nonlinear optics applications such as wavelength conversion, parametric amplification, frequency comb, and entangled photon pair generation. By introducing nonlinear materials in TPIs, novel nonlinear topological devices could be realized, including robust nonlinear optical isolators, switches, and enhanced harmonic generation [49, 63, 68, 147]. There are also many interesting applications of TPIs in quantum photonics, such as topologically-protected transport of single photons and photon entanglements, as well as robust quantum light sources and amplifiers [33, 59, 148]. Additionally, the ROR structure proposed in Chapter 7 and detailed in Appendix A provides a robust platform for experimental investigation of various aspects of the complex Hofstadter spectrum at optical frequencies, as well as the topological properties of circular and 1D periodic photonic lattices, effective 2D topological lattices with a synthetic dimension in the roundtrip phase variation.

Bibliography

[1] B. J. Shastri *et al.*, “Photonics for artificial intelligence and neuromorphic computing,” *Nature Photonics*, vol. 15, pp. 102–114, 2 Jan. 2021, ISSN: 1749-4893. DOI: 10.1038/s41566-020-00754-y. [Online]. Available: https://www.nature.com/articles/s41566-020-00754-y.

[2] F. Flamini, N. Spagnolo, and F. Sciarrino, “Photonic quantum information processing: A review,” *Reports on Progress in Physics*, vol. 82, p. 016 001, 1 Nov. 2018, ISSN: 0034-4885. DOI: 10.1088/1361-6633/AAD5B2. [Online]. Available: https://iopscience.iop.org/article/10.1088/1361-6633/aad5b2.

[3] Z. Wang, Y. Chong, J. D. Joannopoulos, and M. Soljačić, “Observation of unidirectional backscattering-immune topological electromagnetic states,” *Nature*, vol. 461, p. 772, 7265 2009.

[4] Y. E. Kraus, Y. Lahini, Z. Ringel, M. Verbin, and O. Zilberberg, “Topological states and adiabatic pumping in quasicrystals,” *Physical Review Letters*, vol. 109, p. 106 402, 10 2012.

[5] R. O. Umucalılar and I. Carusotto, “Artificial gauge field for photons in coupled cavity arrays,” *Phys. Rev. A*, vol. 84, p. 043 804, 4 Oct. 2011. DOI: 10.1103/PhysRevA.84.043804. [Online]. Available: https://link.aps.org/doi/10.1103/PhysRevA.84.043804.

[6] K. Fang, Z. Yu, and S. Fan, “Realizing effective magnetic field for photons by controlling the phase of dynamic modulation,” *Nature Photonics*, vol. 6, 11 2012, ISSN: 17494885. DOI: 10.1038/nphoton.2012.236.

[7] M. Hafezi, E. A. Demler, M. D. Lukin, and J. M. Taylor, “Robust optical delay lines with topological protection,” *Nature Physics*, vol. 7, 11 2011, ISSN: 17452473. DOI: 10.1038/nphys2063.

[8] M. Hafezi, S. Mittal, J. Fan, A. Migdall, and J. M. Taylor, “Imaging topological edge states in silicon photonics,” *Nature Photonics*, vol. 7, 12 2013, ISSN: 17494885. DOI: 10.1038/nphoton.2013.274.

[9] G. Q. Liang and Y. D. Chong, “Optical resonator analog of a two-dimensional topological insulator,” *Physical Review Letters*, vol. 110, p. 203 904, 20 2013.

[10] A. B. Khanikaev, S. H. Mousavi, W.-K. Tse, M. Kargarian, A. H. MacDonald, and G. Shvets, “Photonic topological insulators,” *Nature materials*, vol. 12, pp. 233–239, 3 2013.

[11] L. Lu, J. D. Joannopoulos, and M. Soljačić, "Topological photonics," *Nat. Photonics*, vol. 8, pp. 821–829, 11 2014.

[12] L. Lu, J. D. Joannopoulos, and M. Soljačić, "Topological states in photonic systems," *Nature Physics*, vol. 12, p. 626, 7 2016.

[13] A. B. Khanikaev and G. Shvets, "Two-dimensional topological photonics," *Nat. photonics*, vol. 11, pp. 763–773, 12 2017.

[14] T. Ozawa *et al.*, "Topological photonics," *Rev. Mod. Phys.*, vol. 91, p. 15 006, 1 2019.

[15] M. Z. Hasan and C. L. Kane, "Colloquium: Topological insulators," *Reviews of Modern Physics*, vol. 82, 4 2010, ISSN: 00346861. DOI: 10.1103/RevModPhys.82.3045.

[16] J. K. Asbóth, L. Oroszlány, and A. Pályi, *A short course on topological insulators*. Springer, 2016, vol. 919, pp. 997–1000.

[17] C. Ferrari, F. Morichetti, and A. Melloni, "Disorder in coupled-resonator optical waveguides," *JOSA B*, vol. 26, pp. 858–866, 4 2009.

[18] A Tsay and V Van, "Analytic theory of strongly-coupled microring resonators," *IEEE Journal of Quantum Electronics*, vol. 47, pp. 997–1005, 7 2011, ISSN: 1558-1713. DOI: 10.1109/JQE.2011.2149498.

[19] V. Van, "Optical microring resonators : Theory, techniques, and applications," *Optical Microring Resonators*, Dec. 2016. DOI: 10.1201/9781315303512. [Online]. Available: https://www.taylorfrancis.com/books/mono/10.1201/9781315303512/optical-microring-resonators-vien-van.

[20] B. Bahari, A. Ndao, F. Vallini, A. E. Amili, Y. Fainman, and B. Kanté, "Nonreciprocal lasing in topological cavities of arbitrary geometries," *Science*, vol. 358, pp. 636–640, 6363 2017.

[21] M. A. Bandres *et al.*, "Topological insulator laser: Experiments," *Science*, vol. 359, eaar4005, 6381 2018.

[22] Y. Wang *et al.*, "Topological protection of two-photon quantum correlation on a photonic chip," *Optica*, vol. 6, pp. 955–960, 8 2019.

[23] D. C. Tsui, H. L. Stormer, and A. C. Gossard, "Two-dimensional magnetotransport in the extreme quantum limit," *Physical Review Letters*, vol. 48, p. 1559, 22 1982.

[24] D. J. Thouless, M. Kohmoto, M. P. Nightingale, and M. D. Nijs, "Quantized hall conductance in a two-dimensional periodic potential," *Physical Review Letters*, vol. 49, p. 405, 6 1982.

[25] M. Kohmoto, "Topological invariant and the quantization of the hall conductance," *Annals of Physics*, vol. 160, pp. 343–354, 2 1985.

[26] X.-G. Wen, "Topological orders and edge excitations in fractional quantum hall states," *Advances in Physics*, vol. 44, no. 5, pp. 405–473, 1995. DOI: 10.1080/00018739500101566. eprint: https://doi.org/10.1080/00018739500101566. [Online]. Available: https://doi.org/10.1080/00018739500101566.

[27] C. L. Kane and E. J. Mele, "Quantum spin hall effect in graphene," *Physical Review Letters*, vol. 95, p. 226 801, 22 2005.

[28] C. L. Kane and E. J. Mele, "Z 2 topological order and the quantum spin hall effect," *Physical Review Letters*, vol. 95, p. 146 802, 14 2005.

[29] F. D. M. Haldane and S Raghu, "Possible realization of directional optical waveguides in photonic crystals with broken time-reversal symmetry," *Physical Review Letters*, vol. 100, p. 13 904, 1 2008.

[30] S. Raghu and F. D. Haldane, "Analogs of quantum-hall-effect edge states in photonic crystals," *Physical Review A - Atomic, Molecular, and Optical Physics*, vol. 78, p. 033 834, 3 Sep. 2008, ISSN: 10502947. DOI: 10.1103/PhysRevA.78.033834. [Online]. Available: https://journals.aps.org/pra/abstract/10.1103/PhysRevA.78.033834.

[31] D. Leykam, S Mittal, M Hafezi, and Y. D. Chong, "Reconfigurable topological phases in next-nearest-neighbor coupled resonator lattices," *Phys. Rev. Lett.*, vol. 121, p. 23 901, 2 2018.

[32] S. Mittal, V. V. Orre, D. Leykam, Y. D. Chong, and M. Hafezi, "Photonic anomalous quantum hall effect," *Phys. Rev. Lett.*, vol. 123, p. 43 201, 4 2019.

[33] S. Barik *et al.*, "A topological quantum optics interface," *Science*, vol. 359, pp. 666–668, 6376 2018.

[34] J. Noh, S. Huang, K. P. Chen, and M. C. Rechtsman, "Observation of photonic topological valley hall edge states," *Phys. Rev. Lett.*, vol. 120, p. 63 902, 6 2018.

[35] M. I. Shalaev, W. Walasik, A. Tsukernik, Y. Xu, and N. M. Litchinitser, "Robust topologically protected transport in photonic crystals at telecommunication wavelengths," *Nat. Nanotechnol.*, vol. 14, p. 31, 1 2019.

[36] X.-T. He *et al.*, "A silicon-on-insulator slab for topological valley transport," *Nat. Commun.*, vol. 10, pp. 1–9, 1 2019.

[37] W.-J. Chen *et al.*, "Experimental realization of photonic topological insulator in a uniaxial metacrystal waveguide," *Nature Communications*, vol. 5, p. 5782, 2014.

[38] J. M. Zeuner *et al.*, "Observation of a topological transition in the bulk of a non-hermitian system," *Physical Review Letters*, vol. 115, p. 40 402, 4 2015.

[39] T. Kitagawa, E. Berg, M. Rudner, and E. Demler, "Topological characterization of periodically driven quantum systems," *Phys. Rev. B*, vol. 82, p. 235 114, 23 Dec. 2010. DOI: 10.1103/PhysRevB.82.235114. [Online]. Available: https://link.aps.org/doi/10.1103/PhysRevB.82.235114.

[40] N. H. Lindner, G. Refael, and V. Galitski, "Floquet topological insulator in semiconductor quantum wells," *Nature Physics*, vol. 7, pp. 490–495, 6 2011, ISSN: 1745-2481. DOI: 10.1038/nphys1926. [Online]. Available: https://doi.org/10.1038/nphys1926.

[41] M. C. Rechtsman *et al.*, "Photonic floquet topological insulators," *Nature*, vol. 496, pp. 196–200, 7444 2013, ISSN: 1476-4687. DOI: 10.1038/nature12066. [Online]. Available: https://doi.org/10.1038/nature12066.

[42] M. S. Rudner, N. H. Lindner, E. Berg, and M. Levin, "Anomalous edge states and the bulk-edge correspondence for periodically driven two-dimensional systems," *Physical Review X*, vol. 3, p. 31 005, 3 Jul. 2013. DOI: 10.1103/PhysRevX.3.031005. [Online]. Available: https://link.aps.org/doi/10.1103/PhysRevX.3.031005.

[43] D. Leykam, M. C. Rechtsman, and Y. D. Chong, "Anomalous topological phases and unpaired dirac cones in photonic floquet topological insulators," *Phys. Rev. Lett.*, vol. 117, p. 13 902, 1 2016.

[44] Y.-G. Peng *et al.*, "Experimental demonstration of anomalous floquet topological insulator for sound," *Nat. Commun.*, vol. 7, pp. 1–8, 1 2016.

[45] F. Gao *et al.*, "Probing topological protection using a designer surface plasmon structure," *Nat. Commun.*, vol. 7, pp. 1–9, 1 2016.

[46] S. Mukherjee *et al.*, "Experimental observation of anomalous topological edge modes in a slowly driven photonic lattice," *Nat. Commun.*, vol. 8, p. 13 918, 2017.

[47] M. Pasek and Y. D. Chong, "Network models of photonic floquet topological insulators," *Physical Review B*, vol. 89, p. 75 113, 7 2014.

[48] F. Nathan and M. S. Rudner, "Topological singularities and the general classification of floquet–bloch systems," *New J. Phys.*, vol. 17, p. 125 014, 12 2015.

[49] D. Leykam and Y. D. Chong, "Edge solitons in nonlinear-photonic topological insulators," *Physical Review Letters*, vol. 117, 14 2016, ISSN: 10797114. DOI: 10.1103/PhysRevLett.117.143901.

[50] S. Afzal and V. Van, "Topological phases and the bulk-edge correspondence in 2D photonic microring resonator lattices," *Opt. Express*, vol. 26, no. 11, pp. 14 567–14 577, May 2018. DOI: 10.1364/OE.26.014567. [Online]. Available: http://www.opticsexpress.org/abstract.cfm?URI=oe-26-11-14567.

[51] L. J. Maczewsky, J. M. Zeuner, S. Nolte, and A. Szameit, "Observation of photonic anomalous floquet topological insulators," *Nature Communications*, vol. 8, p. 13 756, 1 2017, ISSN: 2041-1723. DOI: 10.1038/ncomms13756. [Online]. Available: https://doi.org/10.1038/ncomms13756.

[52] S. Mukherjee, H. K. Chandrasekharan, P. Öhberg, N. Goldman, and R. R. Thomson, "State-recycling and time-resolved imaging in topological photonic lattices," *Nat. Commun.*, vol. 9, p. 4209, 1 2018.

[53] Z. Zhang, P. Delplace, and R. Fleury, "Superior robustness of anomalous non-reciprocal topological edge states," *Nature*, vol. 598, pp. 293–297, 7880 2021, ISSN: 1476-4687. DOI: 10.1038/s41586-021-03868-7. [Online]. Available: https://doi.org/10.1038/s41586-021-03868-7.

[54] H Song, H Wang, and V Van, "An analytical method for evaluating the robustness of photonic integrated circuits," *Journal of Lightwave Technology*, vol. 40, pp. 776–784, 3 2022, ISSN: 1558-2213. DOI: 10.1109/JLT.2022.3141394.

[55] T. Dai *et al.*, "Topologically protected quantum entanglement emitters," *Nature Photonics*, vol. 16, pp. 248–257, 3 2022, ISSN: 1749-4893. DOI: 10.1038/s41566-021-00944-2. [Online]. Available: https://doi.org/10.1038/s41566-021-00944-2.

[56] C. Jörg, F. Letscher, M. Fleischhauer, and G. Freymann, "Dynamic defects in photonic floquet topological insulators," *New Journal of Physics*, vol. 19, p. 083 003, 8 2017, ISSN: 1367-2630. DOI: 10.1088/1367-2630/aa7c82. [Online]. Available: http://dx.doi.org/10.1088/1367-2630/aa7c82.

[57] S. Mukherjee and M. C. Rechtsman, "Observation of floquet solitons in a topological bandgap," *Science*, vol. 368, no. 6493, pp. 856–859, 2020. DOI: 10.1126/science.aba8725. eprint: https://www.science.org/doi/pdf/10.1126/science.aba8725. [Online]. Available: https://www.science.org/doi/abs/10.1126/science.aba8725.

[58] S Mittal, J Fan, S Faez, A Migdall, J. M. Taylor, and M Hafezi, "Topologically robust transport of photons in a synthetic gauge field," *Phys. Rev. Lett.*, vol. 113, p. 87 403, 8 2014.

[59] S. Mittal, E. A. Goldschmidt, and M. Hafezi, "A topological source of quantum light," *Nature*, vol. 561, pp. 502–506, 7724 2018. DOI: 10.1038/s41586-018-0478-3.

[60] S. Afzal, T. J. Zimmerling, Y. Ren, D. Perron, and V. Van, "Realization of anomalous floquet insulators in strongly coupled nanophotonic lattices," *Phys. Rev. Lett.*, vol. 124, p. 253 601, 25 Jun. 2020. DOI: 10.1103/PhysRevLett.124.253601. [Online]. Available: https://link.aps.org/doi/10.1103/PhysRevLett.124.253601.

[61] S. Mittal, V. V. Orre, E. A. Goldschmidt, and M. Hafezi, "Tunable quantum interference using a topological source of indistinguishable photon pairs," *Nature Photonics*, vol. 15, pp. 542–548, 7 May 2021, ISSN: 1749-4893. DOI: 10.1038/s41566-021-00810-1. [Online]. Available: https://www.nature.com/articles/s41566-021-00810-1.

[62] S. Chen *et al.*, "Few-layer topological insulator for all-optical signal processing using the nonlinear kerr effect," *Advanced Optical Materials*, vol. 3, 12 2015, ISSN: 21951071. DOI: 10.1002/adom.201500347.

[63] X. Zhou, Y. Wang, D. Leykam, and Y. D. Chong, "Optical isolation with nonlinear topological photonics," *New Journal of Physics*, vol. 19, 9 2017, ISSN: 13672630. DOI: 10.1088/1367-2630/aa7cb5.

[64] M. Jung *et al.*, "A femtosecond pulse fiber laser at 1935 nm using a bulk-structured Bi_2Te_3 topological insulator," *Optics Express*, vol. 22, pp. 7865–7874, 7 2014.

[65] P St-Jean *et al.*, "Lasing in topological edge states of a one-dimensional lattice," *Nat. Photonics*, vol. 11, pp. 651–656, 10 2017.

[66] D. Smirnova, S. Kruk, D. Leykam, E. Melik-Gaykazyan, D. Y. Choi, and Y. Kivshar, "Third-harmonic generation in photonic topological metasurfaces," *Physical Review Letters*, vol. 123, p. 103 901, 10 Sep. 2019, ISSN: 10797114. DOI: 10.1103/PhysRevLett.123.103901. [Online]. Available: https://journals.aps.org/prl/abstract/10.1103/PhysRevLett.123.103901.

[67] Z. Lan, J. W. You, and N. C. Panoiu, “Nonlinear one-way edge-mode interactions for frequency mixing in topological photonic crystals,” *Phys. Rev. B*, vol. 101, p. 155 422, 15 Apr. 2020. DOI: 10.1103/PhysRevB.101.155422. [Online]. Available: https://link.aps.org/doi/10.1103/PhysRevB.101.155422.

[68] S. Kruk *et al.*, “Nonlinear light generation in topological nanostructures,” *Nature Nanotechnology*, vol. 14, pp. 126–130, 2 2019. DOI: 10.1038/s41565-018-0324-7.

[69] J. W. You, Z. Lan, and N. C. Panoiu, “Four-wave mixing of topological edge plasmons in graphene metasurfaces,” *Science Advances*, vol. 6, no. 13, 2020. DOI: 10.1126/sciadv.aaz3910. eprint: https://advances.sciencemag.org/content/6/13/eaaz3910.full.pdf. [Online]. Available: https://advances.sciencemag.org/content/6/13/eaaz3910.

[70] A. Simbula *et al.*, “Realization of high-Q/V photonic crystal cavities defined by an effective Aubry-André-Harper bichromatic potential,” *APL Photonics*, vol. 2, p. 056 102, 5 Apr. 2017, ISSN: 23780967. DOI: 10.1063/1.4979708. [Online]. Available: https://aip.scitation.org/doi/abs/10.1063/1.4979708.

[71] J. Hou, D. Gao, H. Wu, R. Hao, and Z. Zhou, “Flat band slow light in symmetric line defect photonic crystal waveguides,” *IEEE Photonics Technology Letters*, vol. 21, no. 20, pp. 1571–1573, 2009. DOI: 10.1109/LPT.2009.2030160.

[72] J. Noh *et al.*, “Topological protection of photonic mid-gap defect modes,” *Nat. Photonics*, vol. 12, pp. 408–415, 7 2018.

[73] Y. F. Gao *et al.*, “Topologically protected defect modes in all-dielectric photonic crystals,” *Journal of Physics D: Applied Physics*, vol. 53, p. 365 104, 36 Jun. 2020, ISSN: 0022-3727. DOI: 10.1088/1361-6463/AB9047. [Online]. Available: https://iopscience.iop.org/article/10.1088/1361-6463/ab9047https://iopscience.iop.org/article/10.1088/1361-6463/ab9047/meta.

[74] X. Xu *et al.*, “Topological transition and topological line defects in dielectric photonic crystals,” *Optics Communications*, vol. 498, p. 127 262, 2021, ISSN: 0030-4018. DOI: https://doi.org/10.1016/j.optcom.2021.127262. [Online]. Available: https://www.sciencedirect.com/science/article/pii/S0030401821005113.

[75] S. Afzal and V. Van, “Bulk mode resonances in floquet topological insulators based on coupled microring resonator lattices,” in *2019 Conference on Lasers and Electro-Optics Europe and European Quantum Electronics Conference*, Optical Society of America, 2019, ec_p_5. [Online]. Available: http://www.osapublishing.org/abstract.cfm?URI=EQEC-2019-ec_p_5.

[76] S. Afzal and V. Van, “Trapping light in a floquet topological photonic insulator by floquet defect mode resonance,” *APL Photonics*, vol. 6, 11 2021, ISSN: 23780967. DOI: 10.1063/5.0061950.

[77] T. J. Zimmerling, S. Afzal, and V. Van, “Broadband resonance-enhanced frequency generation by four-wave mixing in a silicon floquet topological photonic insulator,” *APL Photonics*, vol. 7, no. 5, p. 056 104, 2022. DOI: 10.1063/5.0087217. eprint: https://doi.org/10.1063/5.0087217. [Online]. Available: https://doi.org/10.1063/5.0087217.

[78] S. Afzal, D. Perron, T. Zimmerling, Y. Ren, and V. Van, "Observation of anomalous floquet insulator edge states in periodically-driven silicon photonic topological microresonator lattices," in *Frontiers in Optics + Laser Science APS/DLS*, Optica Publishing Group, 2019, FM4E.4. DOI: 10.1364/FIO.2019.FM4E.4. [Online]. Available: https://opg.optica.org/abstract.cfm?URI=FiO-2019-FM4E.4.

[79] FDTD Lumerical, *Ansys Solutions Inc*, 2022.

[80] *Santec.com TUNABLE SEMICONDUCTOR LASER TSL-510 Operation Manual*, 2022. [Online]. Available: https://www.santec.com/dcms_media/other/instruments_TSL-510-M-E.pdf.

[81] *Model 1936/2936-C Series Single and Dual-Channel Optical Meters*, 2022. [Online]. Available: https://neurophysics.ucsd.edu/Manuals/Newport/1936-2936_Power_Meter_User's_Manual.pdf.

[82] B. Höckendorf, A. Alvermann, and H. Fehske, "Universal driving protocol for symmetry-protected floquet topological phases," *Phys. Rev. B*, vol. 99, p. 245 102, 24 2019.

[83] Sensors Unlimited, *SU320M-1.7RT InGaAs NIR MiniCamera*. [Online]. Available: http://alacron.com/clientuploads/directory/Cameras/SENSORS\%20UNLIMITED/4110-0005.pdf.

[84] H. Fukuda *et al.*, "Four-wave mixing in silicon wire waveguides," *Opt. Express*, vol. 13, no. 12, pp. 4629–4637, Jun. 2005. DOI: 10.1364/OPEX.13.004629. [Online]. Available: http://www.opticsexpress.org/abstract.cfm?URI=oe-13-12-4629.

[85] B. Luther-Davies *et al.*, "Third-harmonic generation in slow-light chalcogenide glass photonic crystal waveguides," *Optics Letters*, vol. 36, pp. 2818–2820, 15 Aug. 2011, ISSN: 1539-4794. DOI: 10.1364/OL.36.002818. [Online]. Available: https://opg.optica.org/ol/abstract.cfm?uri=ol-36-15-2818.

[86] C. W. Wong, D.-L. Kwong, J. F. McMillan, and M. Yu, "Observation of four-wave mixing in slow-light silicon photonic crystal waveguides," *Optics Express*, vol. 18, pp. 15 484–15 497, 15 Jul. 2010, ISSN: 1094-4087. DOI: 10.1364/OE.18.015484. [Online]. Available: https://opg.optica.org/oe/abstract.cfm?uri=oe-18-15-15484.

[87] F. Morichetti, A. Canciamilla, C. Ferrari, A. Samarelli, M. Sorel, and A. Melloni, "Travelling-wave resonant four-wave mixing breaks the limits of cavity-enhanced all-optical wavelength conversion," *Nature Communications*, vol. 2, 1 2001. DOI: 10.1038/ncomms1294. [Online]. Available: https://doi.org/10.1038/ncomms1294.

[88] S. Azzini *et al.*, "Stimulated and spontaneous four-wave mixing in silicon-on-insulator coupled photonic wire nano-cavities," *Applied Physics Letters*, vol. 103, 3 2013, ISSN: 00036951. DOI: 10.1063/1.4812640.

[89] M. Ferrera *et al.*, "Low-power continuous-wave nonlinear optics in doped silica glass integrated waveguide structures," *Nature Photonics*, vol. 2, 12 2008, ISSN: 17494885. DOI: 10.1038/nphoton.2008.228.

[90] M. Ferrera *et al.*, "Low power four wave mixing in an integrated, micro-ring resonator with Q = 1.2 million," *Opt. Express*, vol. 17, no. 16, pp. 14 098–14 103, Aug. 2009. DOI: 10.1364/OE.17.014098. [Online]. Available: http://www.osapublishing.org/oe/abstract.cfm?URI=oe-17-16-14098.

[91] A. C. Turner, M. A. Foster, A. L. Gaeta, and M. Lipson, "Ultra-low power parametric frequency conversion in a silicon microring resonator," *Opt. Express*, vol. 16, no. 7, pp. 4881–4887, Mar. 2008. DOI: 10.1364/OE.16.004881. [Online]. Available: http://www.opticsexpress.org/abstract.cfm?URI=oe-16-7-4881.

[92] J. Wu *et al.*, "2D layered graphene oxide films integrated with micro-ring resonators for enhanced nonlinear optics," *Small*, vol. 16, p. 1 906 563, 16 Apr. 2020, ISSN: 1613-6829. DOI: 10.1002/SMLL.201906563. [Online]. Available: https://onlinelibrary.wiley.com/doi/10.1002/smll.201906563.

[93] Y. Qu *et al.*, "Enhanced four-wave mixing in silicon nitride waveguides integrated with 2d layered graphene oxide films," *Advanced Optical Materials*, vol. 8, p. 2 001 048, 23 Dec. 2020, ISSN: 2195-1071. DOI: 10.1002/ADOM.202001048. [Online]. Available: https://onlinelibrary.wiley.com/doi/10.1002/adom.202001048.

[94] Y. Zhang, J. Wu, Y. Qu, L. Jia, B. Jia, and D. J. Moss, "Design and optimization of four-wave mixing in microring resonators integrated with 2d graphene oxide films," *Journal of Lightwave Technology*, vol. 39, pp. 6553–6562, 20 Oct. 2021, ISSN: 15582213. DOI: 10.1109/JLT.2021.3101292.

[95] G. P. Agrawal, "Chapter 10 - four-wave mixing," in *Nonlinear Fiber Optics (Sixth Edition)*, G. P. Agrawal, Ed., Sixth, Academic Press, 2019, pp. 401–462, ISBN: 978-0-12-817042-7. DOI: https://doi.org/10.1016/B978-0-12-817042-7.00017-8. [Online]. Available: https://www.sciencedirect.com/science/article/pii/B9780128170427000178.

[96] IDS Imaging Development Systems Inc., *UI-1460SE-C-HQ (AB.0010.1.09510.24)*.

[97] E. Dulkeith, F. Xia, L. Schares, W. M. J. Green, and Y. A. Vlasov, "Group index and group velocity dispersion in silicon-on-insulator photonic wires," *Opt. Express*, vol. 14, no. 9, pp. 3853–3863, May 2006. DOI: 10.1364/OE.14.003853. [Online]. Available: http://www.osapublishing.org/oe/abstract.cfm?URI=oe-14-9-3853.

[98] A. C. Turner *et al.*, "Tailored anomalous group-velocity dispersion in silicon channel waveguides," *Opt. Express*, vol. 14, no. 10, pp. 4357–4362, May 2006. DOI: 10.1364/OE.14.004357. [Online]. Available: http://www.osapublishing.org/oe/abstract.cfm?URI=oe-14-10-4357.

[99] *TUNABLE LD LIGHT SOURCE TSL-210 Operation Manual*, 2022. [Online]. Available: https://www.manualslib.com/manual/1726682/Santec-Tsl-Series.html.

[100] D. Bajoni *et al.*, "Micrometer-scale integrated silicon source of time-energy entangled photons," *Optica*, vol. 2, pp. 88–94, 2 Feb. 2015, ISSN: 2334-2536. DOI: 10.1364/OPTICA.2.000088. [Online]. Available: https://opg.optica.org/optica/abstract.cfm?uri=optica-2-2-88.

[101] T. J. Zimmerling, S. Afzal, and V. Van, “Fwm frequency generation in topological floquet defect mode resonance,” in *Frontiers in Optics + Laser Science 2021*, Optica Publishing Group, 2021, FM2E.2. DOI: 10.1364/FIO.2021.FM2E.2. [Online]. Available: https://opg.optica.org/abstract.cfm?URI=FiO-2021-FM2E.2.

[102] A. Peruzzo *et al.*, “Quantum walks of correlated photons,” *Science*, vol. 329, no. 5998, pp. 1500–1503, 2010. DOI: 10.1126/science.1193515. eprint: https://www.science.org/doi/pdf/10.1126/science.1193515. [Online]. Available: https://www.science.org/doi/abs/10.1126/science.1193515.

[103] Z.-Q. Jiao *et al.*, “Two-dimensional quantum walks of correlated photons,” *Optica*, vol. 8, no. 9, pp. 1129–1135, Sep. 2021. DOI: 10.1364/OPTICA.425879. [Online]. Available: http://opg.optica.org/optica/abstract.cfm?URI=optica-8-9-1129.

[104] C. Esposito *et al.*, “Quantum walks of two correlated photons in a 2D synthetic lattice,” *Quantum Information*, vol. 8, pp. 1–7, 1 Mar. 2022, ISSN: 2056-6387. DOI: 10.1038/s41534-022-00544-0. [Online]. Available: https://www.nature.com/articles/s41534-022-00544-0.

[105] G. Benenti, G. Casati, and G. Strini, *Principles of quantum computation and information. [electronic resource]*. World Scientific, 2004. [Online]. Available: https://login.ezproxy.library.ualberta.ca/login?url=https://search.ebscohost.com/login.aspx?direct=true&db=cat03710a&AN=alb.7753604&site=eds-live&scope=site.

[106] C. Schimpf *et al.*, “Quantum cryptography with highly entangled photons from semiconductor quantum dots,” *Science Advances*, vol. 7, no. 16, eabe8905, 2021. DOI: 10.1126/sciadv.abe8905. eprint: https://www.science.org/doi/pdf/10.1126/sciadv.abe8905. [Online]. Available: https://www.science.org/doi/abs/10.1126/sciadv.abe8905.

[107] E. Knill, R. Laflamme, and G. J. Milburn, “A scheme for efficient quantum computation with linear optics,” *Nature 2001*, vol. 409, pp. 46–52, 6816 Jan. 2001, ISSN: 1476-4687. DOI: 10.1038/35051009. [Online]. Available: https://www.nature.com/articles/35051009.

[108] C. H. Bennett and G. Brassard, “Quantum cryptography: Public key distribution and coin tossing,” *Theoretical Computer Science*, vol. 560, pp. 7–11, 2014, Theoretical Aspects of Quantum Cryptography – celebrating 30 years of BB84, ISSN: 0304-3975. DOI: https://doi.org/10.1016/j.tcs.2014.05.025. [Online]. Available: https://www.sciencedirect.com/science/article/pii/S0304397514004241.

[109] T. Kupko *et al.*, “Tools for the performance optimization of single-photon quantum key distribution,” *Quantum Information*, vol. 6, pp. 1–8, 1 Mar. 2020, ISSN: 2056-6387. DOI: 10.1038/s41534-020-0262-8. [Online]. Available: https://www.nature.com/articles/s41534-020-0262-8.

[110] J. E. Sharping *et al.*, “Generation of correlated photons in nanoscale silicon waveguides,” *Optics Express*, vol. 14, pp. 12 388–12 393, 25 Dec. 2006, ISSN: 1094-4087. DOI: 10.1364/OE.14.012388. [Online]. Available: https://opg.optica.org/oe/abstract.cfm?uri=oe-14-25-12388.

[111] H. Takesue *et al.*, "Generation of high-purity entangled photon pairs using silicon wire waveguide," *Optics Express*, vol. 16, pp. 20 368–20 373, 25 Dec. 2008, ISSN: 1094-4087. DOI: 10.1364/OE.16.020368. [Online]. Available: https://opg.optica.org/oe/abstract.cfm?uri=oe-16-25-20368.

[112] S Clemmen *et al.*, "Continuous wave photon pair generation in silicon-on-insulator waveguides and ring resonators," *Optics Express*, vol. 17, pp. 16 558–16 570, 19 Sep. 2009, ISSN: 1094-4087. DOI: 10.1364/OE.17.016558. [Online]. Available: https://opg.optica.org/oe/abstract.cfm?uri=oe-17-19-16558.

[113] A. S. Clark *et al.*, "Slow-light enhanced correlated photon pair generation in a silicon photonic crystal waveguide," *Optics Letters*, vol. 36, pp. 3413–3415, 17 Sep. 2011, ISSN: 1539-4794. DOI: 10.1364/OL.36.003413. [Online]. Available: https://opg.optica.org/ol/abstract.cfm?uri=ol-36-17-3413.

[114] M. Davanço *et al.*, "Telecommunications-band heralded single photons from a silicon nanophotonic chip," *Applied Physics Letters*, vol. 100, p. 261 104, 26 Jun. 2012, ISSN: 0003-6951. DOI: 10.1063/1.4711253. [Online]. Available: https://aip.scitation.org/doi/abs/10.1063/1.4711253.

[115] J. D. Franson, "Bell inequality for position and time," *Physical Review Letters*, vol. 62, p. 2205, 19 May 1989, ISSN: 00319007. DOI: 10.1103/PhysRevLett.62.2205. [Online]. Available: https://journals.aps.org/prl/abstract/10.1103/PhysRevLett.62.2205.

[116] P. G. Kwiat, A. M. Steinberg, and R. Y. Chiao, "High-visibility interference in a bell-inequality experiment for energy and time," *Physical Review A*, vol. 47, R2472, 4 Apr. 1993, ISSN: 10502947. DOI: 10.1103/PhysRevA.47.R2472. [Online]. Available: https://journals.aps.org/pra/abstract/10.1103/PhysRevA.47.R2472.

[117] R. Wakabayashi *et al.*, "Time-bin entangled photon pair generation from si micro-ring resonator," *Optics Express*, vol. 23, pp. 1103–1113, 2 Jan. 2015, ISSN: 1094-4087. DOI: 10.1364/OE.23.001103. [Online]. Available: https://opg.optica.org/oe/abstract.cfm?uri=oe-23-2-1103.

[118] J. Suo, S. Dong, W. Zhang, Y. Huang, and J. Peng, "Generation of hyper-entanglement on polarization and energy-time based on a silicon micro-ring cavity," *Opt. Express*, vol. 23, no. 4, pp. 3985–3995, Feb. 2015. DOI: 10.1364/OE.23.003985. [Online]. Available: http://opg.optica.org/oe/abstract.cfm?URI=oe-23-4-3985.

[119] J. R. Ong, M. Savanier, R. Kumar, and S. Mookherjea, "Entanglement measurement of a coupled silicon microring photon pair source," *Optics Express*, vol. 23, pp. 19 318–19 327, 15 Jul. 2015, ISSN: 1094-4087. DOI: 10.1364/OE.23.019318. [Online]. Available: https://opg.optica.org/oe/abstract.cfm?uri=oe-23-15-19318.

[120] H. Takesue, N. Matsuda, E. Kuramochi, and M. Notomi, "Entangled photons from on-chip slow light," *Scientific Reports*, vol. 4, pp. 1–4, 1 Jan. 2014, ISSN: 2045-2322. DOI: 10.1038/srep03913. [Online]. Available: https://www.nature.com/articles/srep03913.

[121] A. S. Clark, M. J. Collins, A. C. Judge, E. C. Mägi, C. Xiong, and B. J. Eggleton, "Raman scattering effects on correlated photon-pair generation in chalcogenide," *Opt. Express*, vol. 20, no. 15, pp. 16 807–16 814, Jul. 2012. DOI: 10.1364/OE.20.016807. [Online]. Available: http://opg.optica.org/oe/abstract.cfm?URI=oe-20-15-16807.

[122] M. Savanier *et al.*, "Photon pair generation from compact silicon microring resonators using microwatt-level pump powers," *Optics Express*, vol. 24, pp. 3313–3328, 4 Feb. 2016, ISSN: 1094-4087. DOI: 10.1364/OE.24.003313. [Online]. Available: https://opg.optica.org/oe/abstract.cfm?uri=oe-24-4-3313.

[123] C. M. Gentry *et al.*, "Quantum-correlated photon pairs generated in a commercial 45 nm complementary metal-oxide semiconductor microelectronic chip," *Optica*, vol. 2, no. 12, pp. 1065–1071, Dec. 2015. DOI: 10.1364/OPTICA.2.001065. [Online]. Available: http://opg.optica.org/optica/abstract.cfm?URI=optica-2-12-1065.

[124] E. Engin *et al.*, "Photon pair generation in a silicon micro-ring resonator with reverse bias enhancement," *Opt. Express*, vol. 21, no. 23, pp. 27 826–27 834, Oct. 2013. DOI: 10.1364/OE.21.027826. [Online]. Available: http://opg.optica.org/oe/abstract.cfm?URI=oe-21-23-27826.

[125] C. Xiong *et al.*, "Generation of correlated photon pairs in a chalcogenide as2s3 waveguide," *Applied Physics Letters*, vol. 98, no. 5, p. 051 101, 2011. DOI: 10.1063/1.3549744. eprint: https://doi.org/10.1063/1.3549744. [Online]. Available: https://doi.org/10.1063/1.3549744.

[126] T. Santiago-Cruz *et al.*, "Resonant metasurfaces for generating complex quantum states," *Science (New York, N.Y.)*, vol. 377, no. 6609, 991—995, Aug. 2022, ISSN: 0036-8075. DOI: 10.1126/science.abq8684. [Online]. Available: https://doi.org/10.1126/science.abq8684.

[127] M. Fox, "Chapter 6: Photon antibunching," in *Quantum Optics: An introduction*. Oxford University Press, 2006, pp. 105–125.

[128] M. Dinu, F. Quochi, and H. Garcia, "Third-order nonlinearities in silicon at telecom wavelengths," *Applied Physics Letters*, vol. 82, p. 2954, 18 Apr. 2003, ISSN: 0003-6951. DOI: 10.1063/1.1571665. [Online]. Available: https://aip.scitation.org/doi/abs/10.1063/1.1571665.

[129] IDQuantique, *Id281 superconducting nanowire series*. [Online]. Available: https://www.idquantique.com/quantum-sensing/products/id281-snspd-series/.

[130] S. Afzal, T. J. Zimmerling, V. Van, and S. Barzanjeh, "Resonance-enhanced entangled photon pair generation using topological floquet defect mode resonance," in *CLEO 2023*, Optica Publishing Group, 2023, FF1L.3. DOI: 10.1364/CLEO_FS.2023.FF1L.3. [Online]. Available: https://opg.optica.org/abstract.cfm?URI=CLEO_FS-2023-FF1L.3.

[131] S. Afzal *et al.*, *Bright quantum photon sources from a topological floquet resonance*, 2023. arXiv: 2308.11451 [quant-ph]. [Online]. Available: https://doi.org/10.48550/arXiv.2308.11451.

[132] F. Y. Gardes *et al.*, "High-speed modulation of a compact silicon ring resonator based on a reverse-biased pn diode," *Optics Express*, vol. 17, pp. 21 986–21 991, 24 Nov. 2009, ISSN: 1094-4087. DOI: 10.1364/OE.17.021986. [Online]. Available: https://opg.optica.org/oe/abstract.cfm?uri=oe-17-24-21986.

[133] C. Qiu, J. T. Robinson, Q. Xu, R. Soref, and W. Gao, "Reconfigurable electro-optical directed-logic circuit using carrier-depletion micro-ring resonators," *Optics Letters*, vol. 39, pp. 6767–6770, 24 Dec. 2014, ISSN: 1539-4794. DOI: 10.1364/OL.39.006767. [Online]. Available: https://opg.optica.org/ol/abstract.cfm?uri=ol-39-24-6767.

[134] Y. Tian *et al.*, "Experimental demonstration of a reconfigurable electro-optic directed logic circuit using cascaded carrier-injection micro-ring resonators," *Scientific Reports*, vol. 7, pp. 1–10, 1 Jul. 2017, ISSN: 2045-2322. DOI: 10.1038/s41598-017-06736-5. [Online]. Available: https://www.nature.com/articles/s41598-017-06736-5.

[135] I. Electro-Optics Technology, *Amplified high speed fiber photodetectors user guide*. [Online]. Available: https://www.photonicsolutions.co.uk/upfiles/AmplifiedHighSpeedFiberPhotodetectorsUsersGuide.pdf.

[136] New Imaging Technologies, *WiDy SenS 640 HIGH SENSITIVITY & HDR CAMERA*. [Online]. Available: https://new-imaging-technologies.com/product/widy-sens-640/.

[137] E. Lustig *et al.*, "Photonic topological insulator in synthetic dimensions," *Nature*, vol. 567, p. 356, 7748 2019. [Online]. Available: https://doi.org/10.1038/s41586-019-0943-7.

[138] A. Dutt, M. Minkov, I. A. D. Williamson, and S. Fan, "Higher-order topological insulators in synthetic dimensions," *Light: Science & Applications*, vol. 9, p. 131, 1 2020. [Online]. Available: https://doi.org/10.1038/s41377-020-0334-8.

[139] D. Cheng, K. Wang, and S. Fan, "Artificial non-abelian lattice gauge fields for photons in the synthetic frequency dimension," *Phys. Rev. Lett.*, vol. 130, p. 083 601, 8 Feb. 2023. DOI: 10.1103/PhysRevLett.130.083601. [Online]. Available: https://link.aps.org/doi/10.1103/PhysRevLett.130.083601.

[140] M. Y. Azbel, "Energy spectrum of a conduction electron in a magnetic field," *Journal of Experimental and Theoretical Physics*, vol. 46, pp. 929–946, Mar. 1964. [Online]. Available: http://www.jetp.ac.ru/cgi-bin/dn/e_019_03_0634.pdf.

[141] D. R. Hofstadter, "Energy levels and wave functions of bloch electrons in rational and irrational magnetic fields," *Physical Review B*, vol. 14, 6 1976, ISSN: 01631829. DOI: 10.1103/PhysRevB.14.2239.

[142] Z. A. Kudyshev, A. V. Kildishev, A. Boltasseva, and V. M. Shalaev, "Photonic topological phase transition on demand," *Nanophotonics*, vol. 8, pp. 1349 –1356, 2019.

[143] H. A. Haus, *Waves and Fields in Optoelectronics*. Prentice-Hall Inc., Englewood Cliffs, New Jersey, 1984, ch. 7, ISBN: 0-13-946053-5.

[144] P. G. Harper, "Single band motion of conduction electrons in a uniform magnetic field," *Proceedings of the Physical Society. Section A*, vol. 68, 10 1955, ISSN: 03701298. DOI: 10.1088/0370-1298/68/10/304.

[145] T. J. Zimmerling and V. Van, "Generation of hofstadter's butterfly spectrum using circular arrays of microring resonators," *Opt. Lett.*, vol. 45, no. 3, pp. 714–717, Feb. 2020. DOI: 10.1364/OL.384552. [Online]. Available: https://opg.optica.org/ol/abstract.cfm?URI=ol-45-3-714.

[146] F. Gan *et al.*, "Maximizing the thermo-optic tuning range of silicon photonic structures," in *2007 Photonics in Switching, PS*, 2007. DOI: 10.1109/PS.2007.4300747.

[147] D. Smirnova, D. Leykam, Y. Chong, and Y. Kivshar, "Nonlinear topological photonics," *Applied Physics Reviews*, vol. 7, no. 2, p. 021 306, 2020. DOI: 10.1063/1.5142397. eprint: https://doi.org/10.1063/1.5142397. [Online]. Available: https://doi.org/10.1063/1.5142397.

[148] V. Peano, M. Houde, F. Marquardt, and A. A. Clerk, "Topological quantum fluctuations and traveling wave amplifiers," *Phys. Rev. X*, vol. 6, p. 041 026, 4 Nov. 2016. DOI: 10.1103/PhysRevX.6.041026. [Online]. Available: https://link.aps.org/doi/10.1103/PhysRevX.6.041026.

[149] H. Jayatilleka, H. Shoman, L. Chrostowski, and S. Shekhar, "Photoconductive heaters enable control of large-scale silicon photonic ring resonator circuits," *Optica*, vol. 6, no. 1, pp. 84–91, Jan. 2019. DOI: 10.1364/OPTICA.6.000084. [Online]. Available: https://opg.optica.org/optica/abstract.cfm?URI=optica-6-1-84.

Appendix A: Psuedo-Infinite 1D Lattice

This project aims to experimentally demonstrate topological photonic insulator behaviours in circular arrays of microring resonators. We propose a new topological photonic lattice based on a circular array of microring resonators, called a ring-of-rings (ROR). By periodically varying the resonant frequencies of the microring resonators, we have shown theoretically that the structure can exhibit topological behaviours. The devices and structures submitted to the 2001PH AMF Silicon Photonics fabrication process can be used to experimentally verify the predicted topological properties.

A.1 Design

As described in Chapter 7, a realistic $N = 20$ device can be designed using a ring of microring resonators. The designed device rings have radii of approximately 11.27 μm and an effective index $n_{eff} \sim 2.57$, providing a roundtrip time $T_{rt} \sim 0.61$ ns. The roundtrip field attenuation factor $a_{rt} = \exp{-\alpha\pi R}$. For 3 dB/cm, $\alpha = 0.69cm^{-1}$ and a microring radius $\sim 11.27\mu$m, $a_{rt} \sim 0.9976$. The inter-resonator power-coupling coefficients κ^2 are between 6% and 16%, depending on the wavelength and which device is being tested. The overall layout of the device follows the ROR design that is presented in Fig. 7.1b.

A.2 Fabrication

The photonic chip consists of 3 arrays of microring resonators, where each microring has a diameter of approximately 23 micrometers. 2 arrays consist of 20 microring resonators in an ROR forming a 1D pseudo-infinite structure, while 1 array consists of 20 microring resonators in a 1D array to act as a baseline. The 2 ROR arrays differ in their coupling strength between microresonators to account for some variation in fabrication. The microring resonators implement doped silicon junctions for resonant frequency tuning. The photoconductive heater layout follows that described in [149], with an $N_{pp}/N/N_{pp}$ doping profile, a general sketch of which is provided in Fig. A.1a. The heating junctions are located away from the coupling regions to maximize impact on resonance frequency while minimizing impact on coupling coefficients. The waveguides are designed as rib waveguides with 500 nm widths and 130 nm heights, with 90 nm slabs to support the doped sections of silicon. The coupling gaps of one ROR device are 300 nm and the other are 250 nm. The coupling lengths for both are approximately 3.4 μm.

A.3 Testing

The devices can be wirebonded to a PCB and interfaced with Arduino controllers. As shown in Fig. A.1b, the electric circuits required to control these devices are quite complex. Electrical currents can be applied to the in-line $N_{pp}/N/N_{pp}$ doped junction heaters to tune and control the resonant frequencies of individual microring resonators in the array. These devices have the added benefit of producing a photo-current can be measured to provide additional information on the optical power present in each microring. Figure. A.1c provides a look at an entire ROR device. Each device shares 2 ground pads between all of the heating elements, the inside of the ROR is grounded and the perimeter of the ROR is grounded. Additionally, each heating circuit requires its own metal pad to apply heating current independently, which is applied to the center of each microring. Figure A.1d provides more detail of a single resonator, showing the details of the in-line photoconductive heater element distribution around the microring resonator. For each setting of the resonant frequency distribution, we can measure the transmission spectrum of the device using tunable lasers and photodetectors around the 1500-1600 nm wavelength range. In addition to investigating the transmission spectra of the ROR, we can also image the scattered light

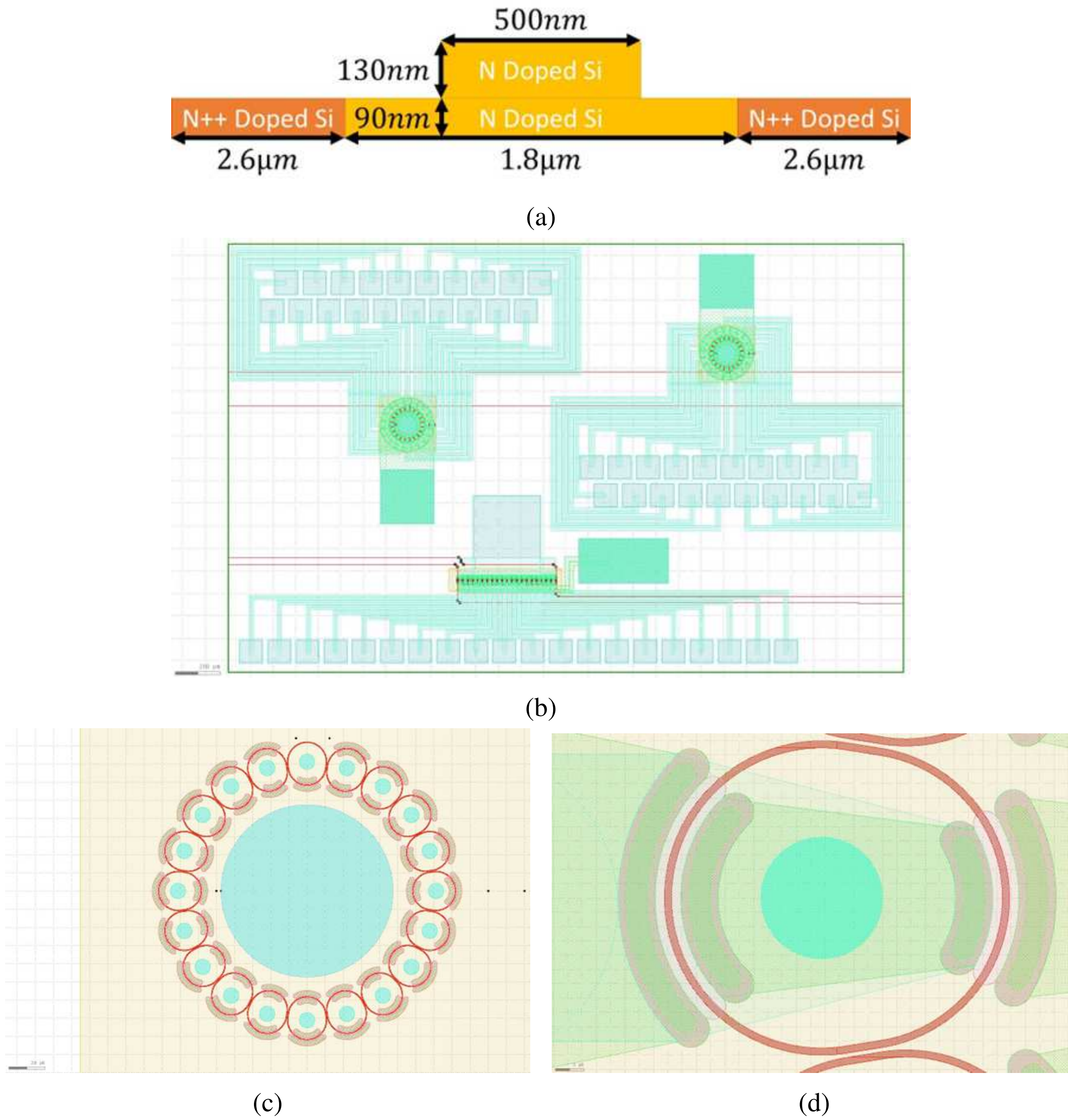

Figure A.1: (a) A general sketch of the $N_{pp}/N/N_{pp}$ photoconductive heater layout. (b) KLayout GDS file of the entire chip. The scale bar is in the bottom left. (c) KLayout GDS file of one ring-of-rings structure with detail of the layout of the microresonators. Some of the metal layers are hidden to show the important structures. The scale bar is in the bottom left. (d) KLayout GDS file of a single microring resonator, showing the detail of the $N_{pp}/N/N_{pp}$ doping locations around the resonator.

intensity distribution in the microring array using an NIR camera and a microscope setup, which can provide visual confirmation of expected light distribution in the structure.

Appendix B: Nonlinear thermo-optic effect in the FDMR at high optical powers

As mentioned in Chapter 4, at on-chip input laser powers $\gtrsim 0.5$ mW, a red shift and skewing of the linear FDMR spectrum could be observed. This is due to the nonlinear thermo-optic effect in the silicon waveguide, which is caused by an intensity-dependent change in the refractive index of silicon. Figure B.1 demonstrates the difference in the measured spectra for input laser powers of 0.03 mW and 25 mW, which corresponded to 3 μW and 2.55 mW in the waveguide, respectively. Figures B.1 (a), (b) and (c) show the resonance spectra at the signal, pump and idler wavelengths, respectively for 3 μW input power, while Figures B.1 (d), (e) and (f) show the corresponding spectra at 2.55 mW input power. Due to the red shift and skewing of the spectra at high optical powers, it was necessary to fine tune the signal, pump and idler wavelengths in order to achieve maximum resonance enhancement for maximum wavelength conversion efficiency at each level of input pump power.

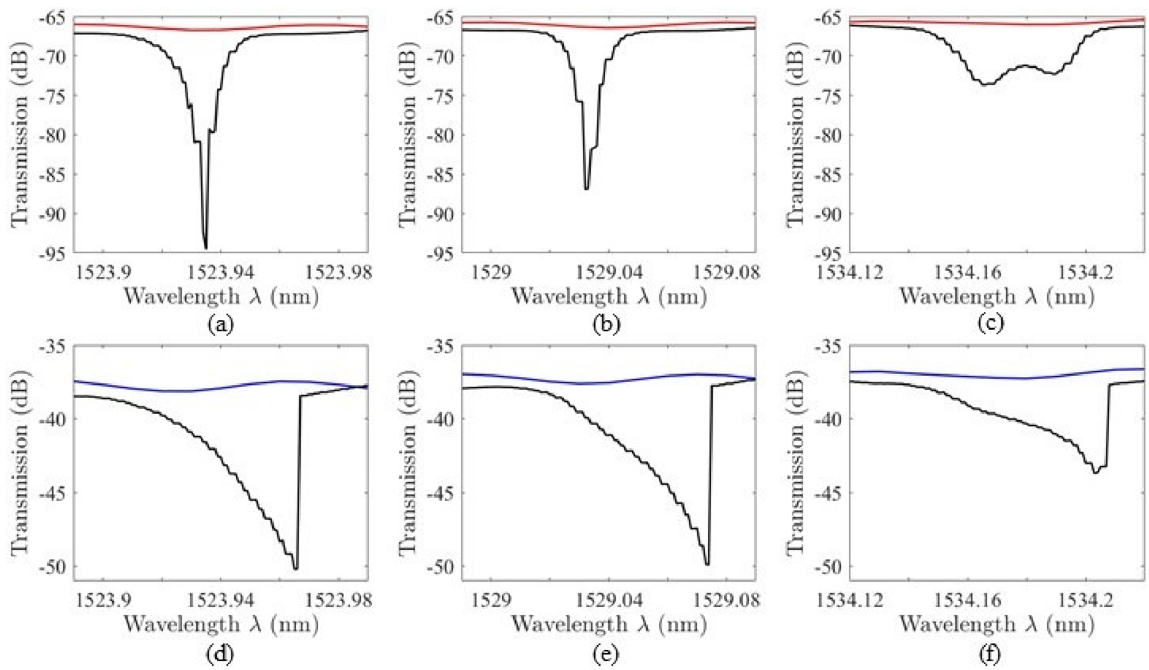

Figure B.1: Spectral scans of the background TPI lattice without heating power applied are given in blue and red. The FDMR spectra with 3 μW input optical power are given in (a-c) and with 2.55 mW input optical power in (d-f).